VNIVERSITAT
DE VALÈNCIA

Departamento de Física Teórica

Impact of a (sub)dominant non-cold dark matter component on the large scale structure of the universe

Ph.D. Thesis

Francisco Antonio Villaescusa Navarro

Supervisor

Dr. Carlos Peña Garay

Valencia, March 2012.

CARLOS PEÑA GARAY, Científico titular del Instituto de Física Corpuscular, Universitat de València-CSIC

> CERTIFICA:
>
> Que la presente memoria “IMPACT OF A (SUB)DOMINANT NON-COLD DARK MATTER COMPONENT ON THE LARGE SCALE STRUCTURE OF THE UNIVERSE” ha sido realizada bajo su dirección por FRANCISCO ANTONIO VILLAESCUSA NAVARRO y constituye su Tesis para optar al grado de Doctor en Física.

Y para que así conste, en cumplimiento de la legislación vigente, presenta en el Departamento de Física Teórica de la Universitat de València la referida Tesis Doctoral, y firma el presente certificado.

Valencia, a 15 de Marzo de 2012.

Carlos Peña Garay

A mis padres y a Luz

Agradecimientos - Acknowledgments

Tras 4 años en el mundo de la investigación, puedo afirmar rotundamente que jamás pense que sería tan difícil llegar a este punto. Cuando inicié mi camino en el mundo de la investigación, pensaba que aquellos duros años en donde compaginaba el estudio de 2 carreras, física y matemáticas, se habrían acabado y que con mucho menos esfuerzo podría conseguir muchas más cosas. Por contra, he descubierto que el mundo es muy grande, y esta repleto de personas realmente brillantes y que muchas de ellas tienen una capacidad de sacrificio que es realmente difícil emular.

Mi camino en el mundo científico no solo me ha conducido a Valencia, sino que me dado la magnífica oportunidad de pasar 4 meses en CITA (Toronto, Canada) y 1 año en Harvard (Cambridge, USA). De especial importancia y transcendencia ha sido mi estancia en Harvard. Allí, muchos de mis fantasmas y miedos se esfumaron definitívamente. Rodeado por auténticos gigantes, me he dado cuenta que ser el más inteligente de Rusia, Estados Unidos ó China no implica automáticamente el éxito, sino que este se consigue mediante trabajo, trabajo y más trabajo.

Me gustaría agradecer en primer lugar la ayuda y el apoyo que me han proporcionado mis padres desde siempre, y en particular desde que decidí estudiar física en Valencia. Sin sus numerosos esfuerzos y sacrificios hoy no estaría donde me encuentro. Tampoco mi formación sería la que es, y en los difíciles tiempos que estamos empezando a vivir, esta representa mi mejor carta de presentación en un mundo técnico y globalizado.

Mención especial también se merece mi compañera en la vida, Luz. En apenas 3 años, hemos tenido que vivir en 7 pisos diferentes entre Valencia, Toronto, Boston y Trieste. Hemos compartido muchas experiencias, algunas de ellas, como dormir en el frío suelo de un piso vacío en Cambridge, no especialmente agradables. Sin su compañia, apoyo y sacrifico todo hubiera sido mucho más duro, quizás demasiado.

Quisiera agradecer a mi supervisor, Carlos Peña, la ayuda que me ha brindado durante todo este tiempo. Gracias a él he podido visitar y desarrollarme profesionalmente en algunas de las ”catedrales del saber” como CITA ó Harvard y ha sido gracias a él que he conocido a casi todos mis colaboradores. Su forma de ver la ciencia y el mundo me ha enriquecido enormemente, tanto como investigador como persona. Siempre le estaré agradecido de entender perfectamente el ”two-body problem” y de hacer todo lo que estaba en su mano para soliviantarlo.

A Olga Mena le quiero expresar mi más profunda gratitud. Ella siempre ha estado presente tanto en los buenos momentos, que los han habido, como en los malos y difíciles, que desgraciadamente no han sido pocos. Durante los momentos realmente críticos, Olga siempre me ha ayudado a rebajar la tensión y a ser objetivo y pragmático. Sin esa ayuda quizás esta tesis no estaría escrita. En el plano profesional, siempre ha sido un auténtico placer trabajar, colaborar y en la mayor parte de las ocasiones, pedirle ayuda y consejos.

I would like to thank Neal Dalal for all his help, comprehension and the time he spent teaching me many things in cosmology and astrophysics. From the first moment I arrived at Toronto, Neal not only helped me with the housing stuff, but he encouraged me to socialize and to work really hard. I am specially grateful to him for his patient with me and with my english. My first paper was the result of the wonderful experience I lived at CITA.

A Jordi Miralda li dec molt més que el caràcter critic amb l'anàlisi, els mètodes i els resultats que gràcies a ell he anat millorant, li dec tot el temps que m'ha dedicat contestant-me a les nombroses preguntes i dubtes que li he plantejat al llarg de més d'un any. Encara sent un camí més dur, el màxim rigor en un treball científic marcarà, més prompte o més tard, la diferència entre un article i un bon article. Ha sigut un autèntic privilegi col·laborar amb algú de tanta profunditat i tan respectat en la matèria.

I would also like to express my gratitude to Avi Loeb. Avi allowed me to stay at ITC-Harvard for 1 year and despite its extremely busy agenda, he always found time for our weekly meeting. I am still surprised of the speed at which Avi works and how a single person can produce such large number of amazing ideas in any field, from planets to black holes. I will always remember one sentence I read in an object that Avi had at his office: *It's nice to be important, but more important it's to be nice.*

During the time I was at Harvard I worked very close with Mark Vogelsberger. Mark not only helped me a lot with all the N-body stuff, but he played a key role in the development of our paper with Matteo Viel and Avi Loeb. It was Mark who showed me that very hard work produces wonderful results, and that humility is one of most valuable virtues.

Sono in particolar modo grato a Matteo Viel. Matteo mi ha permesso di accedere ai dati delle sue simulazioni a N-corpi con i neutrini, che è stato il primo passo nella preparazione del nostro articolo. Matteo mi ha insegnato tutto ciò che so sulle Lyman-α forest e senza il suo interessamento, la sua pazienza e la sua competenza, il nostro articolo non avrebbe visto la luce. Quando l'ho incontrato a Barcellona, ho capito che tutte le bellissime cose che le persone dicono sul suo conto non sono semplice cortesia.

También quisiera dar las gracias a mis compañeros, tanto de la carrera como del master y del doctorado. A estas alturas, donde forzosamente nuestras carreras y vidas se irán separando cada vez más, me veo en la necesidad de recolectar y guardar todos los buenos momentos vividos durante estos 4 años. De entre todos ellos, quiero agradecer especialmente a Manu, Urbano, Zahara, Alberto Filipuzzi y Gustavo los bueno ratos que hemos compartido juntos.

Introduction and motivations

Many observations point toward the existence of a non-baryonic matter component in the universe, that we know as dark matter. Several decades ago, people started thinking on the possibility that the relic neutrinos were its constituents. The hypothesis stating that the dark matter is hot, expression used when the dark matter is made up of particles with large velocities (such as relic neutrinos), was soon excluded because it would implied that the first structures formed in the universe should have huge sizes. Objects of smaller size, such as galaxies, stars or planets, could only be formed through fragmentation of the initial giant structures. The fact that we do not observe such huge structures, in addition to the large number of small size objects that we see, provide evidence strong enough to rule out the possibility that neutrinos are either the unique or the main component of the dark matter.

Recently, the discover of the flavour change in different sources of neutrinos, known as the neutrino oscillations, has demonstrated that the neutrinos have mass, and therefore, they constitute a fraction of the dark matter. Although their contribution to the whole dark matter would be small, their large thermal velocities make them to behave in a very different way than the rest of the dark matter. Those large thermal velocities impact, among others, on the process of structure formation, delaying the formation time and evolution of cosmic structures. The effect of the relic neutrinos on the large scale structure of the universe has been studied and it is well understood in the lineal regime. In contrast, their impact on the non-lineal regime has not been systematically studied and it is nowadays poorly understood. In the era of precision cosmology in which we are entering, it is mandatory to understand correctly the effects that each energetic component produce on the large scale structure of the universe, thus, the impact of the neutrinos should be addressed in order to estimate both, Ω_ν and the rest of the cosmological parameters. In this thesis, all calculations were performed in the non-lineal regime, comparing the results with the ones in the lineal regime when it was necessary.

Nowadays, one of the most important questions in physics is: What are the masses of the neutrinos? In this thesis I have searched for cosmological observables, beyond the lineal regime, that would be sensitive to the masses of the neutrinos. On one hand, I have studied the possible detection, using gravitational lenses, of neutrino halos which are formed in the largest bound gravitational structures of the universe, the galaxy clusters. On the other hand I have studied how relic neutrinos modified the shape, size and evolution of the cosmological voids. For the observational detection of this effect, we have studied the signals that neutrinos produce on the high transmission regions of the Lyman-α forest.

Ruled out the hypothesis stating that the dark matter could be hot, the standard cosmological model assumes that the dark matter is cold. This model has passed successfully numerous tests over the last years and it is nowadays the most accepted model for cosmology by the community. However, it has several big problems that the model should solve to preserve its validity.

The cosmological N-body simulations are used as a laboratory where different universes are created to study their properties and evolution. By running those simulations, using the standard cosmological model, it is observed that the density profiles of the dark matter halos are well described by the *Navarro-Frenk-White* (NFW) profile. In the NFW profile, the dark matter density grows towards the center of the halo as $1/r$, forming a cusp. However, there are some types of galaxies where the dark matter density profile does not follow that trend, but the dark matter density profile remains constant, forming a core. Also in conflict with the standard cosmological model N-body simulations is the number of dark matter halos surrounding galaxies such as the Milky Way: simulations indicate that this number is much larger than the one measured by detecting dwarf galaxies around the Milky Way.

A strong effort from both, the theoretical and the observational side, is being carried out in order to conciliate simulations with observations. One of the possible solutions to both problems, comes from the so-called warm dark matter, i.e. dark matter made up of particles with thermal velocities between those of the relic neutrinos and those of the cold dark matter (these ones are considered negligibles). This type of dark matter would alleviate the problem with the number of dark matter halos surrounding Milky Way galaxies and also, because of the Tremaine-Gunn limit, the density profiles of the dark matter halos would present a core.

The N-body simulations performed till now, december 2011, do not have enough resolution to answer the question whether warm dark matter can produce cores, in the dark matter density profile, large enough to reproduce those observed in some types of galaxies such as the low surface brightness (LSB) galaxies. In this thesis, in collaboration with professor Neal Dalal, we have given an answer to the previous question.

The thesis is organized in five blocks: theoretical introduction, scientific research, summary and conclusions, appendixes and bibliography.

In the first block, theoretical introduction, we introduce the basic elements in cosmology and we present both, the dark matter and the neutrinos. We describe the properties of the cosmological neutrinos and their impact on the large scale structure of the universe at the lineal regime.

In the chapter number one, cosmological model ΛCDM, we present the standard cosmological model, its theoretical pillars and the observables that support its validity.

In the chapter number two, dark matter, we show the experimental evidence in favor of the existence of the dark matter, the plausible candidates and we describe briefly the cosmological N-body simulations.

In the chapter number three, cosmological neutrinos, we present the main properties of those particles and introduce the cosmic relic neutrino background, as predicted by the standard cosmological model. We also show the main effects that relic neutrinos produce on the large scale structure of the universe, at the lineal regime.

In the second block, scientific research, we present the scientific work carried out in this thesis. This block has 3 chapters, each one representing a scientific publication.

In the chapter number four, cores and cusps in warm dark matter halos, we answer to the question whether warm dark matter can produce cores, in the density profile of dark matter halos, large enough to reproduce those observed in some galaxies such as the LSB galaxies.

In the chapter number five, neutrinos halos and their weak lensing signature, we present a detailed study about the formation of neutrino halos in the gravitational potentials of galaxy clusters, and how these halos could be detected using weak lensing.

In the chapter number six, neutrino signatures on the high transmission regions of the Lyman-α forest, we introduce a new cosmological observable, which seems to be very sensitive to the masses of the neutrinos. We show how the regions with low baryon density, i.e. the regions with low dark matter density, are zones very sensitive to the masses of the relic neutrinos. We also describe a method which can be used to constrain Ω_ν using a set of high resolution QSO spectra.

In the third block, summary and conclusions, we summarize the motivation, objectives and achievements of the work done in this thesis. In the forth block we show the list of publications carried out during the time of this thesis, a summary of the thesis in spanish and additional information complementing the chapter 6. Finally, in the fifth block, we exhibit the bibliography.

Contents

Agradecimientos - Acknowledgments **vii**

Introduction and motivations **ix**

I Cosmology Overview 1

1 Cosmological model ΛCDM **3**

1.1 Theoretical model 3
  1.1.1 Pillars 3
  1.1.2 FRW metric 4
  1.1.3 Ideal fluid 5
  1.1.4 Einstein's equations 6
  1.1.5 Friedmann's equations 7
  1.1.6 Redshift 9
1.2 Cosmological parameters 11
  1.2.1 Supernovae 11
  1.2.2 CMB 14
  1.2.3 LSS 17

2 Dark matter **23**

2.1 Observational evidence 23
  2.1.1 Gravitationally bound systems 23
  2.1.2 Spiral galaxies rotation curves 24
  2.1.3 X-rays 25
  2.1.4 Gravitational lensing 26

2.1.5 Cosmic microwave background 26
2.1.6 Baryonic Acoustic Oscillations 27
2.1.7 Bullet cluster 27
2.2 Candidates 30
2.2.1 MACHO's 30
2.2.2 WIMP 30
2.2.3 Axions 32
2.3 Dark matter cosmological simulations 32

3 Cosmological Neutrinos **37**
3.1 Introduction 37
3.2 Masses 38
3.3 Relic neutrinos 42
3.4 Impact on cosmology 44

II Scientific Research **53**

4 Cores and cusps in warm dark matter halos **55**
4.1 Introduction 55
4.2 Numerical Method 58
4.3 Results 62
4.3.1 Anatomy of a WDM halo 63
4.3.2 Dependence on physical parameters 67
4.4 Discussion and summary 71

5 Neutrino halos in clusters of galaxies and their weak lensing signature **73**
5.1 Introduction 73
5.2 Numerical method 74
5.2.1 Mass density profile 74
5.2.2 Dark matter halo evolution 76
5.2.3 Neutrino orbits 78
5.3 Neutrino density profiles 79
5.4 Neutrino detection with weak lensing 81

5.5 Conclusion 86

6 Neutrino Signatures on the High Transmission Regions of the Lyman-α Forest 89

6.1 Introduction 89

6.2 Numerical Method 91

6.3 Analysis of the simulations 93

6.4 Numerical convergence 93

6.5 Discussion and Conclusions 95

III Summary and Conclusions 97

7 Summary and Conclusions 99

IV Appendices 103

A Publications 105

B Introducción, resumen y conclusiones en castellano 107

B.1 Introducción y motivaciones 107

B.2 El modelo cosmológico estándar 109

B.2.1 Modelo teórico 110

B.2.2 Parámetros Cosmológicos 114

B.3 Materia oscura 118

B.3.1 Evidencia observacional 118

B.3.2 Candidatos 121

B.4 Neutrinos 123

B.4.1 Introducción 123

B.4.2 Masas 124

B.4.3 Neutrinos cósmicos 126

B.4.4 Impacto en cosmología 127

B.5 Resumen y conclusiones 130

C Ω_ν sensitivity **135**

C.1 Introduction 135

C.2 Systematic errors 135

C.3 Uncertainty in the parameters 137

C.4 Conclusion 137

V Bibliography **139**

Part I

Cosmology Overview

Chapter 1

Cosmological model ΛCDM

In this chapter we illustrate the standard cosmological model. The chapter contains two major sections: the theoretical model itself, where we introduce the model, the basic concepts, the most important equations that we will use in the rest of the thesis and a brief description of the main methods used to measure the cosmological parameters.

1.1 Theoretical model

In this section we review the principles of both, the theory of general relativity and cosmology and we show the Einstein's and Friedmann's equations. We also present the description, in terms of general relativity, of an ideal fluid in cosmology. We finally introduce some of the parameters of the standard cosmological model and describe some basic concepts such as the redshift.

1.1.1 Pillars

One of the pillars of cosmology is the so-called *cosmological principle*. It proclaims that the universe is homogeneous and isotropic on large scales. This principle has been tested by observations [88][20], which point out that on scales above ~ 100 Mpc, the universe looks the same in all directions. On smaller scales, the universe is highly inhomogeneous. A proof of this is the fact that we observe planets, stars, galaxies, cluster of galaxies and cosmological voids.

Other pillar of modern cosmology is the theory of general relativity, which is nowadays the most successful theory of gravity. Formulated by Albert Einstein in 1916 [25], it is the standard theory used to describe gravity. Einstein constructed his theory under the following assumptions:

- The speed of light in vacuum as an invariant in any system of reference.

- The equivalence principle[1].

In general relativity the geometry and causal structure of the universe can be described by a 4-dimensional manifold

$$ds^2 = g_{\mu\nu} dx^\mu dx^\nu \ , \tag{1.1}$$

where $g_{\mu\nu}$ is a 4×4 symmetric tensor called *metric* and dx^μ is a 4-component vector. ds is the proper distance between two events x^μ and $x^\mu + dx^\mu$. For instance, the *Minkowski* metric describes the particular case of a static flat space-time

$$ds^2 = \eta_{\alpha\beta} dx^\alpha dx^\beta = -c^2 dt^2 + dx^2 + dy^2 + dz^2 \ . \tag{1.2}$$

In general relativity, objects move along geodesics of the 4-dimensional space-time geometry described by the metric 1.1. The equations of motion for a test particle[2] are given by

$$\frac{d^2 x^\mu}{d\lambda^2} + \Gamma^\mu_{\nu\gamma} \frac{dx^\nu}{d\lambda} \frac{dx^\gamma}{d\lambda} = 0 \ , \tag{1.3}$$

where λ is a variable used to parametrize the trajectory $x^\mu = x^\mu(\lambda)$. $\Gamma^\mu_{\nu\gamma}$ is the affine connection (also known as the *Christoffel symbols*)

$$\Gamma^\mu_{\nu\gamma} = \frac{1}{2} g^{\mu\sigma} \left[\frac{\partial g_{\sigma\nu}}{\partial x^\gamma} + \frac{\partial g_{\sigma\gamma}}{\partial x^\nu} - \frac{\partial g_{\nu\gamma}}{\partial x^\sigma} \right] \ , \tag{1.4}$$

with the tensor $g^{\mu\sigma}$ satisfying the relation $g^{\alpha\beta} g_{\beta\gamma} = \delta^\alpha_\gamma$, with δ^α_γ being:

$$\delta^\alpha_\gamma = \left\{ \begin{array}{ll} 1, & if\ (\alpha = \gamma) \\ 0, & if\ (\alpha \neq \gamma) \end{array} \right. \ . \tag{1.5}$$

1.1.2 FRW metric

It can be shown that the most general metric for a universe in which the cosmological principle holds (i.e. a homogeneous and isotropic universe) is given by the FRW (*Friedmann-Roberson-Walker*) metric (for a detailed derivation of this metric see for example [103])

$$ds^2 = c^2 dt^2 - a^2(t) \left[\frac{dr^2}{1 - Kr^2} + r^2 \left(d\theta^2 + sin^2\theta d\phi^2 \right) \right] \ , \tag{1.6}$$

---

[1] The equivalence principle states that in any gravitational field, there is always a system of reference in which the effects of gravity are absent.

[2] By test particle we refer to a particle with a mass very small or null so that the geometry of the universe is not distorted by the presence of the particle itself.

where t is the proper time, $a(t)$, which contains the time evolution of the universe, is the so-called *scale factor* and r, θ and ϕ are the spatial spherical comoving coordinates. K is a parameter that takes a value equal to $+1, 0$ or -1 depending on whether the universe is closed, flat or open respectively (i.e. depending on the total mass of the universe).

For the rest of the thesis we will use the metric 1.6 for a flat universe (i.e. with $K = 0$). Even thought this metric does not describe properly the space-time geometry in the neighborhood of planets, starts, galaxies...etc, it describes very well the universe background (i.e. the universe on scales larger than ~ 100 Mpc).

1.1.3 Ideal fluid

All the information about the density and the flux of energy and momentum in the space-time is embedded into the *stress-energy tensor* $T^{\mu\nu}$. In general relativity, the conservation law for this object is

$$T^{\mu\nu}_{;\nu} = \frac{\partial T^{\mu\nu}}{\partial x^{\nu}} + \Gamma^{\mu}_{\gamma\nu} T^{\gamma\nu} + \Gamma^{\nu}_{\gamma\nu} T^{\mu\gamma} = 0 \ . \tag{1.7}$$

This equation represents the relativistic version of the classical momentum and energy conservation laws.

The universe is often modeled as a *perfect fluid*. A perfect fluid is defined as a medium in which at every point there is a locally inertial Cartesian frame of reference, moving with the fluid, in which the fluid appears isotropic. If we are situated in this inertial Cartesian coordinate system, the stress-momentum tensor adquires the form:

$$T^{\mu\nu} = \begin{pmatrix} \rho & 0 & 0 & 0 \\ 0 & p & 0 & 0 \\ 0 & 0 & p & 0 \\ 0 & 0 & 0 & p \end{pmatrix}$$

where ρ and p are the density and pressure respectively. The above stress-tensor can be also written as

$$T^{\mu\nu} = p\eta^{\mu\nu} + (p + \rho) u^{\mu} u^{\nu} \ , \tag{1.8}$$

where $\eta_{\alpha\beta}$ is the Minkowski metric 1.2 and u^{γ} is an object that behaves as a four-vector under Lorentz transformations and which components are $u^0 = 1$, $u^i = 0$ in the local Cartesian coordinate system. This vector is normalized such as $\eta_{\alpha\beta} u^{\alpha} u^{\beta} = -1$.

General relativity implies that any equation describing a physical process must be written in a covariant form. In doing so, it is guaranteed that any observer, independently of his system of reference, can use the same equations and can compute the way in which that physical process happens in any other system of reference. The necessity of covariance comes from the fact that there is not a preference system of reference in general relativity.

The covariant expression of the stress-tensor for a perfect fluid, which reproduces equation 1.8 in a local Cartesian coordinate system, is

$$T^{\mu\nu} = pg^{\mu\nu} + (p+\rho)u^\mu u^\nu \ . \tag{1.9}$$

In this tensor ρ and p are scalars which satisfy the condition that in a local inertial comoving coordinate system, their values equal those of the density and pressure from the tensor 1.8. u^μ behaves as a a four-vector under a general coordinate transformation taking the form $u^0 = 1,\ u^i = 0$ in a local inertial comoving coordinate system and it is normalized such as $g_{\alpha\beta}u^\alpha u^\beta = -1$.

1.1.4 Einstein's equations

Trying to formulate the equations governing gravity, Einstein knew that those equations must be written in a covariant form and that for slowly changing and weak gravitational fields, they must reproduce the Poisson equation

$$\bigtriangledown^2 \phi = 4\pi G T^{00}. \tag{1.10}$$

Einstein also imposed that the order of the derivatives present in the equations should not be greater than 2 (remember that Newton's equations have derivates of second order at most). The only equation satisfying the above three conditions is

$$R_{\mu\nu} - \frac{1}{2}g_{\mu\nu}R = -8\pi G T_{\mu\nu}, \tag{1.11}$$

where $T_{\mu\nu} = g_{\mu\alpha}g_{\nu\beta}T^{\alpha\beta}$, $R_{\mu\nu}$ is the *Ricci tensor*

$$R_{\mu\nu} = \frac{\partial\Gamma^\gamma_{\mu\gamma}}{\partial x^\nu} - \frac{\partial\Gamma^\gamma_{\mu\nu}}{\partial x^\gamma} + \Gamma^\sigma_{\mu\gamma}\Gamma^\gamma_{\nu\sigma} - \Gamma^\sigma_{\mu\nu}\Gamma^\gamma_{\gamma\sigma} \ , \tag{1.12}$$

and R is the *Ricci scalar*

$$R = g_{\alpha\beta}R^{\alpha\beta} \ , \tag{1.13}$$

with $R^{\alpha\beta} = g^{\alpha\mu}g^{\beta\nu}R_{\mu\nu}$. Equations 1.11 are the famous Einstein's equations for the gravitational field. That system is the original set of equations that Einstein wrote. Soon after, he realized that those equations implied a dynamic universe, in contrary with the belief at that time which considered the universe as static and eternal in time. He then modified his equations adding a new term (the presence of this new term is not forbidden for any of the three previous assumptions) in order to allow a static universe.

$$R_{\mu\nu} - \frac{1}{2} g_{\mu\nu} R + g_{\mu\nu}\Lambda = -8\pi G T_{\mu\nu}, \tag{1.14}$$

This term represents a vacuum energy which impregnate the whole universe. Not long after he modified his equations by adding that new term, Edwin Hubble discovered that the universe is in fact in expansion. Einstein referred to this as the greatest mistake of his whole life. Nowadays, we tend to believe that the universe has indeed a cosmological constant Λ currently dominating the energy density of the universe. For the rest of the thesis we will make use of equations derived from the system 1.14.

1.1.5 Friedmann's equations

The geometry and evolution of the universe background is completely described by the metric 1.6, which has two variables: the curvature of the universe, K, and the scale factor, $a(t)$. As we have already discussed, the value of K depends on the total mass of the universe while the temporal dependence of the scale factor depends on the proportion of the different energetic components of the universe.

If we assume that on large scales the universe can be described as a perfect fluid (see equation 1.9) and we use the metric 1.6 and the Einstein equations 1.14, we end up with the *Friedmann equations* [30][31]:

$$\begin{aligned} H^2 = \left(\frac{\dot{a}}{a}\right)^2 &= \frac{8\pi G}{3}\rho - \frac{Kc^2}{a^2} + \frac{\Lambda c^2}{3} \\ \dot{H} + H^2 = \frac{\ddot{a}}{a} &= -\frac{4\pi G}{3}\left(\rho + \frac{3p}{c^2}\right) + \frac{\Lambda c^2}{3}\ . \end{aligned} \tag{1.15}$$

$H(t) = \dot{a}/a$ is the so-called *Hubble function.* $H_0 \equiv H(t_0)$, with t_0 being the current time, is usually parametrized as

$$H_0 = 100\ h \frac{\text{km}}{\text{s Mpc}}\ , \tag{1.16}$$

with $h \sim 0.7$. For the rest of the thesis we will consider the cosmological constant as a fluid with density $\rho_\Lambda = \Lambda c^2/8\pi G$ and pressure $p_\Lambda = -\rho_\Lambda c^2$. By using these expressions, the Friedmann equations can be rewritten in the form:

$$\begin{aligned}\left(\frac{\dot{a}}{a}\right)^2 &= \frac{8\pi G}{3}\rho - \frac{Kc^2}{a^2} \\ \frac{\ddot{a}}{a} &= -\frac{4\pi G}{3}\left(\rho + \frac{3p}{c^2}\right) \ ,\end{aligned} \tag{1.17}$$

where ρ is now $\rho = \rho_{\rm CDM} + \rho_{\rm r} + \rho_\Lambda + ...$ and $p = p_{\rm r} + p_\Lambda + ...$. Note that by combining equations 1.17 we get the expression

$$\dot{\rho} = -3H\left(\rho + \frac{p}{c^2}\right) \ , \tag{1.18}$$

which can also be derived from the conservation law of the stress-momentum tensor $T^{\mu\nu}_{;\nu} = 0$. The above relation represents the energy conservation equation in a dynamical (expanding or contracting) universe.

The relation between the density and the pressure is often parametrized by the so-called *equation of state*

$$p/c^2 = w\rho \ . \tag{1.19}$$

Lets assume that the universe is dominated by dust[3]. In this case the pressure is 0. By using the equation 1.18 with $p = 0$ we conclude that dust density evolves as $\rho_{dust} \propto a^{-3}$. In contrast, if the universe were dominated by radiation $p/c^2 = \rho/3$, the density would evolve as $\rho_{radiation} \propto a^{-4}$. For a general fluid with a equation of state $p/c^2 = w\rho$, with w constant, the solution of the equation 1.18 is given by

$$\rho \propto a^{-3(1+w)} \ . \tag{1.20}$$

A very useful, and commonly used, concept in cosmology is the *critical density*. As we have seen above, depending on the total mass of the universe, this can be open ($K = +1$), close ($K = -1$) or flat ($K = 0$). The critical density is defined as the required density of the universe to be flat. From the first equation of the system 1.17 we can write the critical density as

$$\rho_c^0 = \frac{3H^2(a_0)}{8\pi G} \qquad \rho_c(a) = \frac{3H^2(a)}{8\pi G} \ , \tag{1.21}$$

where a_0 is the today's scale factor and the superscript 0 means that the quantity is compute at the actual time. It is a common practice in cosmology to normalize the scale factor such as $a_0 = 1$. We will use this normalization for the rest of the thesis.

---

[3] By dust we mean matter at a low temperature, so that its pressure is negligible compared to its density

Typically, the content of the universe is specified by the density of each component in units of the critical density of the universe

$$\Omega_i^0 = \frac{\rho_i^0}{\rho_c^0} \qquad \Omega_i = \frac{\rho_i(a)}{\rho_c(a)} \ . \tag{1.22}$$

In a universe having three energetic components, matter (dust), radiation and a cosmological constant, the total density will evolve, according to 1.18, as

$$\rho(a) = \rho_c^0 \left[\Omega_m^0 a^{-3} + \Omega_R^0 a^{-4} + \Omega_\Lambda^0\right] . \tag{1.23}$$

Note that the following relation is always satisfied

$$\Omega_m + \Omega_R + \Omega_\Lambda + \Omega_K = 1 \ , \tag{1.24}$$

where we have defined

$$\Omega_K = -\frac{Kc^2}{a^2 H^2} \ . \tag{1.25}$$

Finally, using 1.20, 1.21, 1.22, 1.24 and 1.25 we can derive the time dependence of the Hubble function

$$H(a) = H_0 \sqrt{\Omega_\Lambda^0 + \Omega_K^0 a^{-2} + \Omega_m^0 a^{-3} + \Omega_R^0 a^{-4}} \ . \tag{1.26}$$

1.1.6 Redshift

Another standard concept in cosmology is the *redshift*, z. Following [104], suppose that there is a star emitting radiation at some comoving distance r_1 from the earth. At some time t_1 in the past this star emitted a photon which was traveling radially to the earth. Because light satisfies the condition $ds^2 = 0$ (light follows null geodesics), we can write the following equality by using the metric 1.6

$$cdt = -a(t)\frac{dr}{\sqrt{1 - Kr^2}}. \tag{1.27}$$

We have taken the negative sign after making the square root because as time increase, the comoving distance decrease (because light is coming to earth). If that photon, emitted at t_1 reaches the earth at the actual time t_0 we can write

$$c\int_{t_1}^{t_0} \frac{dt}{a(t)} = -\int_{r_1}^{0} \frac{dr}{\sqrt{1 - Kr^2}} \ . \tag{1.28}$$

After the first photon was emitted, a second photon left the star in direction to the earth at some posterior time $t_1 + dt_1$. This photon will be reaching the earth at a time $t_0 + dt_0$, satisfying

$$c\int_{t_1+dt_1}^{t_0+dt_0} \frac{dt}{a(t)} = -\int_{r_1}^{0} \frac{dr}{\sqrt{1-Kr^2}} \ . \tag{1.29}$$

By writing the previous equation we have assumed that the star does not have any peculiar velocity, therefore r_1 does not depend on time (the comoving distance r_1 is fixed, while the proper distance $R_1 = a(t)r_1$ increases as time passes due to the expansion of the universe). We can therefore combine the previous equations, 1.29 and 1.30, to obtain

$$\int_{t_1+dt_1}^{t_0+dt_0} \frac{dt}{a(t)} = \int_{t_1}^{t_0} \frac{dt}{a(t)} \ , \tag{1.30}$$

from which we can extract

$$\frac{dt_1}{a(t_1)} = \frac{dt_0}{a(t_0)} \ . \tag{1.31}$$

dt_1 is the time interval between the emission of two successive photons by the star, which is emitting photons with a frequency $\nu_1 = 1/dt_1$. In contrast, $\nu_0 = 1/dt_0$ is the arrival frequency of photons emitted by a star at t_1 with a frequency ν_1. From the previous equation we can compute the frequency observed in the earth, ν_0, of an object that emitted light at t_1 with a frequency ν_1:

$$\nu_0 = \nu_1 \frac{a(t_1)}{a(t_0)} = \nu_1 a(t_1) \ . \tag{1.32}$$

Note that the above expression is also correct if we interpret dt_1 as the interval between two consecutive maximums in a electromagnetic wave, with a frequency $\nu_1 = 1/dt_1$. Under this interpretation a photon emitted at a time t_1 with energy $E_1 = h\nu_1$, will reach the earth at t_0 with an energy $E_0 = h\nu_0 = E_1 a(t_1)/a(t_0) = E_1 a(t_1)$. Therefore, the expansion of the universe not only modifies the frequency of an object emitting radiation but also the energy of the photons themselves reaching the earth.

The redshift is defined as the shift between the observed and the emitted wavelength of an object:

$$z = \frac{\lambda_{\rm obs} - \lambda_{\rm emi}}{\lambda_{\rm emi}} \tag{1.33}$$

where λ_{obs} is the wavelength observed on earth and λ_{emi} is the emitted wavelength. The relation between redshift and the expansion factor is then given by (we have used the relation $\lambda = c/\nu$)

$$1+z=\frac{a(t_0)}{a}=\frac{1}{a}\ . \tag{1.34}$$

The redshift is commonly used in cosmology and astrophysics and it can be measured directly by looking at the shift in the spectra of stars, galaxies...etc. The redshift is a quantity which naively gives an estimate of distance to objects, the higher the redshift the larger the distance to it.

1.2 Cosmological parameters

In this section we briefly describe how the proportions of the different energetic components are measured. The cosmological parameters of the standard cosmological model (i.e. $\Omega_{\rm CDM}$, $\Omega_{\rm b}$, Ω_Λ, Ω_K, H_0...etc) can be constrained by numerous observations, being Supernovae, CMB and LSS the main methods used to perform this task. Here we discuss the physics behind them and show the reader how the parameters are extracted from them.

1.2.1 Supernovae

The study of the supernova luminosity distances is considered as the first probe that pointed at the existence of a cosmological constant. In this subsection we review the methodology and the way in which this conclusion was reached.

One of the standard methods to estimate distances in astronomy is by making use of luminosity measurements. The *absolute luminosity* of an object, L, is the energy per unit of time emitted by such object while the *apparent luminosity*[4], l, is the energy received in the earth per time unit and per area unit. Due to historical reasons these quantities are expressed via magnitudes. The relation between the apparent luminosity and the *apparent magnitude* of an object is defined by (the numerical factors depend on the particular band, in this case we consider the band B)

$$l=2.52\cdot 10^{-5}\times 10^{-2m/5}\ \text{erg cm}^{-2}\ \text{s}^{-1}\ , \tag{1.35}$$

while the relation between the absolute luminosity and the *absolute magnitude* is written as

$$L=3.02\cdot 10^{35}\times 10^{-2M/5}\ \text{erg s}^{-1}\ . \tag{1.36}$$

Note that under this definition, the absolute magnitude of an object corresponds to the apparent magnitude of that object as seen from a distance of 10 pc[5] from it.

---

[4] Note that this terminology is not used at present. The modern name for this quantity is *flux*

[5] 1 parsec (pc) ~ 3.26 light years $\sim 3.09\times 10^{16}\ m$

Since L and l are related by $l = L/(4\pi d^2)$, where d is the distance to the object, the relation between absolute and apparent magnitudes and distance is

$$m = M + 5\ log_{10}\left(\frac{d}{10\ \mathrm{pc}}\right)\ . \tag{1.37}$$

The apparent magnitude can be measured directly on the earth while the absolute magnitude is usually known or inferred by others methods. The above equation, 1.37, works pretty well for objects near the earth, while it is not adequate for objects situated at large distances since some corrections must be taken into account.

For cosmological distances, the expression $l = L/(4\pi d^2)$ needs to be rewritten in the following way:

$$l = \frac{L}{4\pi r^2 a^2(t_0)(1+z)^2}. \tag{1.38}$$

In this expression we have replaced the distance d by the proper distance $R = a(t)r$, with r being the comoving distance to the object and $a(t_0) = 1$ is the expansion factor today. A factor $(1+z)$ is introduced to account for the fact that the rate at which source emits photons and the rate at which are received on earth is reduced by a factor of $1+z$ (see discussion in the redshift section). The other $(1+z)$ factor comes because photons emitted with a energy $h\nu_0$, will reach earth with energy $h\nu_0/(1+z)$.

Since the apparent magnitude, l, can be measured and the absolute magnitude, L, is either known or inferred by others methods, the dependence of the comoving distance, r, with the cosmological parameters can be used to constraint these by using expression 1.38. The dependence of the comoving coordinate r with the redshift z and the cosmological parameters is given by (see eq. 1.5.44 in [104]):

$$r(z) = S\left[\frac{1}{H_0}\int_{1/(1+z)}^{1} \frac{dx}{x^2\sqrt{\Omega_\Lambda + \Omega_K x^{-2} + \Omega_{\mathrm{m}} x^{-3} + \Omega_{\mathrm{R}} x^{-4}}}\right]\ , \tag{1.39}$$

where the functional $S[y]$ is

$$S[y] = \begin{cases} sin\ y & K\ = +1 \\ y & K\ =\ \ 0 \\ sinh\ y & K\ = -1 \end{cases}\ . \tag{1.40}$$

Ω_{m} receives contributions from any non-relativistic particle, i.e. $\Omega_{\mathrm{m}} = \Omega_{\mathrm{b}} + \Omega_{\mathrm{CDM}} + \Omega_\nu$ with neutrinos being non-relativistics today.

Supernovae type Ia are considered *standard candles* because there are strong reasons to believe that their absolute luminosity is fixed. This type of supernova is generated by a process in which a white dwarf star accretes matter from its red dwarf star companion in a binary system. The white dwarf gains matter and eventually reaches its Chandrasekhar

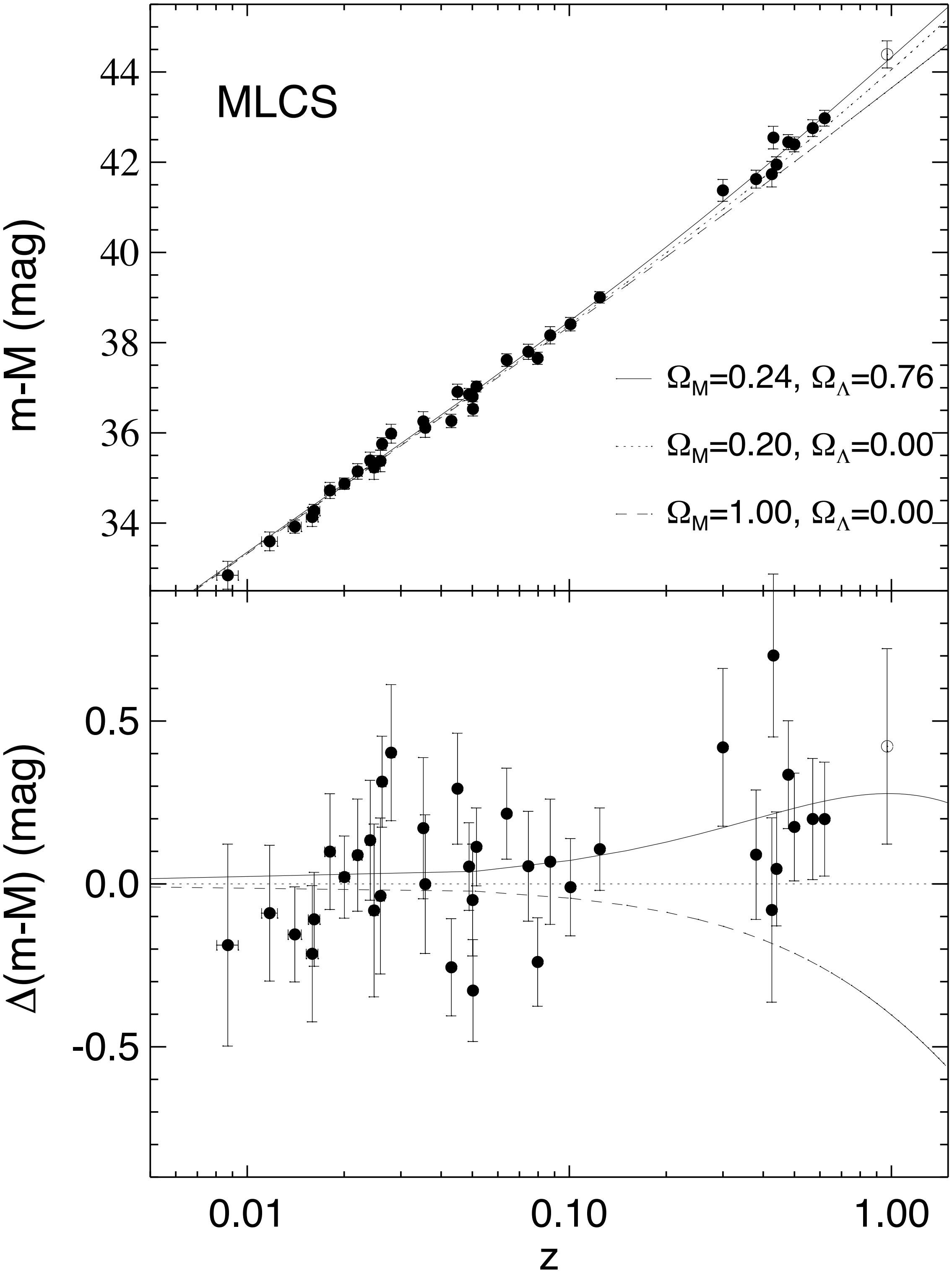

Figure 1.1: m-M (distance) versus redshift. Each point represents a supernova. The solid line the shows the m-M=m-M(z) (the details of the band used can be found on [74]) function for a flat cosmological universe with $\Omega_m = 0.24$ and $\Omega_\Lambda = 0.76$ (see eqs. 1.38 and 1.39). Dashed and dotted lines show the prediction for the cosmological values labelled in the figure. (Image taken from [74])

limit ($\sim 1.4 M_\odot$[6]). Once reached, the star becomes unstable and undergoes a runaway nuclear fusion reaction. Since this supernova type explode at almost the same mass (when Chandrasekhar limit is reached), their absolute luminosity is about the same for all of them. This is particularly important because by measuring both the apparent magnitude and the redshift of this type of supernovae we can extract the function $r(z)$, which dependents on the cosmological parameters Ω_Λ, Ω_K, Ω_m, Ω_R and H_0.

For a set of apparent magnitudes of type Ia supernova at different redshifts, and taking into account that L is a constant, formulas 1.38 and 1.39 can be used to constrain the cosmological parameters Ω_m, Ω_b, Ω_Λ, Ω_K and H_0. In the Figure 1.1 is plotted the m-M magnitude versus the redshift for different type Ia supernovae. From those data it was possible to rule out the hypothesis that the universe only contains matter ($\Omega_m = 1$). The model that best fit the data is the one corresponding to a flat universe ($K = 0$) with $\Omega_m \sim 0.3$ and $\Omega_\Lambda \sim 0.7$, indicating therefore the presence of the dark energy.

1.2.2 CMB

Studies of the distribution of the anisotropies in the cosmic microwave background (CMB) have allowed the determination of the cosmological parameters with an unprecedented precision. Here we present the basis of this method.

In the primordial universe, both photons and baryons were coupled via Thompson scattering forming a plasma. When the temperature of the universe dropped enough to allow electrons to combine with protons to form hydrogen atoms, photons decoupled from the baryons and they were free to travel all along the universe. Some of those photons reach the earth coming from all directions of the sky with an amazing isotropy, presenting a black body spectrum

$$I(\nu, T) = \frac{2h\nu^3}{c^2} \frac{1}{e^{h\nu/K_B T} - 1} \ , \tag{1.41}$$

where $I(\nu, T)$ is the energy per unit of time, per unit of area of the emitting surface, per unit of solid angle and per unit of frequency, with an average temperature T equals to 2.725 K.

The temperature of this background of microwaves is not perfectly isotropic, but it presents deviations of about one part in one hundred thousand. Different sets of values of the cosmological parameters lead to different statistical distributions of the anisotropies in the CMB. For this reason, the analysis of the statistical properties of those anisotropies can be used to constrain the value of the cosmological parameters.

A standard way of studying those temperature perturbations is by expanding them in terms of the spherical harmonics Y_l^m

---

[6] $M_\odot$ denotes the mass of the sun. $M_\odot \sim 2 \times 10^{30}$ kg.

$$\triangle T(\widehat{n}) = T(\widehat{n}) - T_0 = \sum_{lm} a_{lm} Y_l^m(\widehat{n}) \ , \tag{1.42}$$

where $\widehat{n}$ is a normalized vector in a given direction and T_0, the mean CMB temperature, is computed by averaging the temperature over all the directions

$$T_0 = \frac{1}{4\pi} \int d^2\widehat{n} T(\widehat{n}) \ . \tag{1.43}$$

The simplest quantity characterizing the distribution of the anisotropies in the CMB is given by the mean value of the product of two $\triangle T(\widehat{n})$ (a simpler quantity, $< \triangle T(\widehat{n}) >$, is explicitly null given that we assume that the universe is rotationally invariant):

$$< \triangle T(\widehat{n}) \triangle T(\widehat{n}') >= \sum_{lm} C_l Y_l^m(\widehat{n}) Y_l^{-m}(\widehat{n}') = \sum_l C_l \left(\frac{2l+1}{4\pi}\right) P_l(\widehat{n} \cdot \widehat{n}') \ , \tag{1.44}$$

with P_l being the Legendre polynomials. In the previous expression we have made use of the following property which is a consequence of the condition that the universe is rotationally invariant

$$< a_{lm} a_{l'm'} >= \delta_{ll'} \delta_{m-m'} C_l \ . \tag{1.45}$$

In the Figure 1.2 we show the value of C_l as a function of the multipole moment l as measured from 5 different instruments, WMAP, Acbar, Boomerang, CBI and VSA from the CMB. That plot represents the correlations between temperature anisotropies separated by an angle equals to θ, where $\theta \approx \pi/l$. As can be seen from the Figure, there are several peaks in the graphic, indicating the presence of correlations at different angular separations in the CMB.

Physically, what we observe in that Figure are the acoustics waves in the photon-baryon plasma of the primordial universe. Those waves were originated from the primordial inhomogeneities in the distribution of dark matter as the result of the competition between two forces: on one hand radiation pressure acts as a repulsive force, on the other hand gravity tries to compress matter (see the following section for a detailed description of the baryonic acoustic waves). The first peak corresponds to an acoustic wave which was compressed only once before decoupling. Depending on the content of baryons, dark matter...etc in the universe, the shape, position and height of those peaks varies. Therefore, the study of them reveals information about the cosmological parameters.

The position of the first peak is very important since it gives the size of the horizon at the time of decoupling (the horizon is the maximum distance between two regions causally connected) , providing therefore, information about the geometry of the universe. The results indicate that the universe is either flat or it has a very small curvature. The second

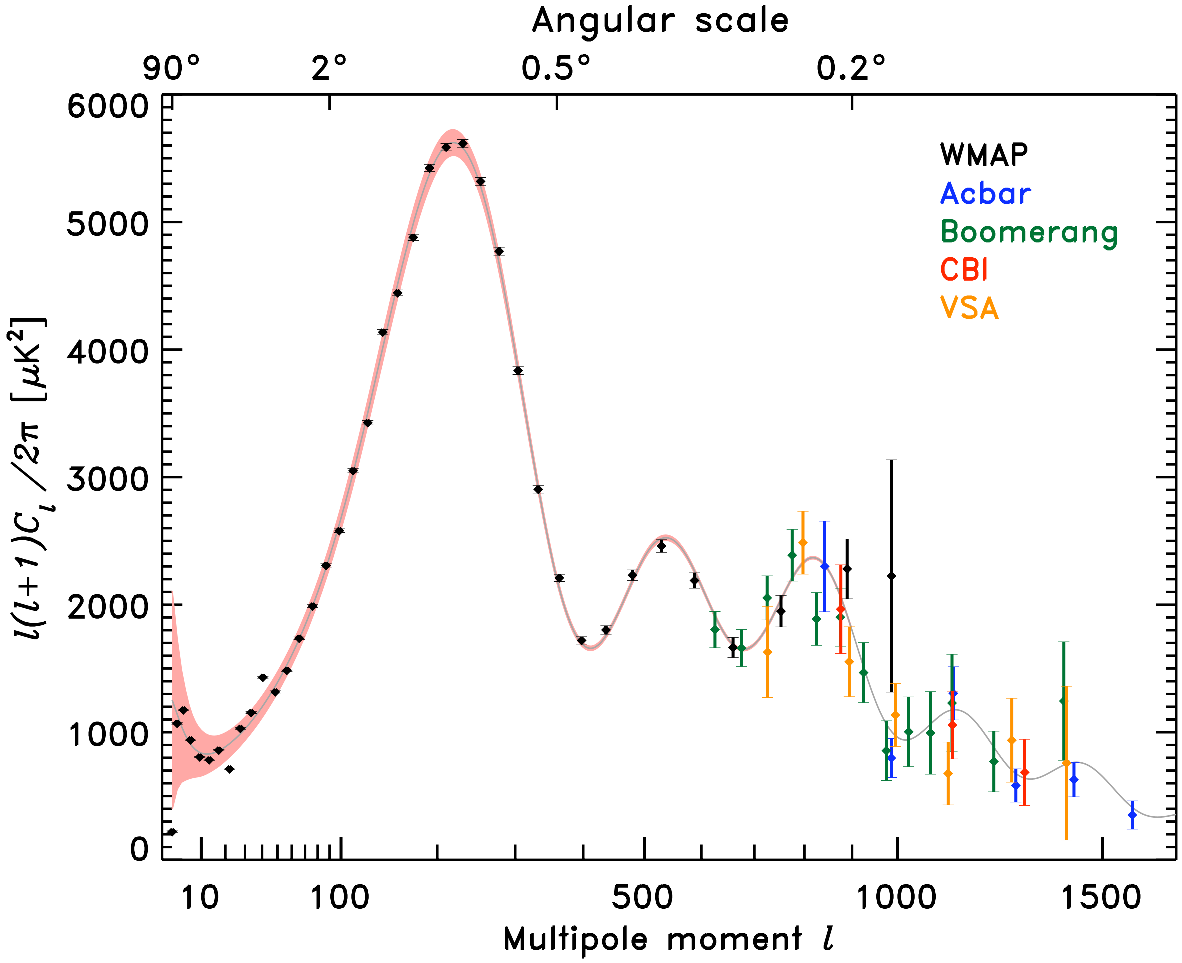

Figure 1.2: C_l versus the multipole moment l for data taken with 5 different instrument, WMAP, Acbar, Boomerang, CBI and VSA from the cosmic microwave background. (Image taken from `http://en.wikipedia.org/wiki/File:PowerSpectrumExt.svg`)

peak contains information about the fraction of baryons in the universe and the fraction of dark matter in the universe is enclosed in the third peak.

1.2.3 LSS

The distribution of matter on large scales can be used to constrain the cosmological parameters. In this subsection we show the standard methods utilized to study the distribution of matter in the universe and how the cosmological parameters can be inferred from them.

In the universe, the stars cluster in groups or galaxies, the galaxies are associated in groups or clusters of galaxies. Surrounding huge cosmological voids, walls and filaments with thousands or millions of galaxies within them form what it is called the cosmic web.

The distribution of matter on those very large scales of the universe contains important information about the cosmological parameters. The so-called *correlation function* is a statistical quantity that contains information about the distribution of matter in the universe. For a continuos field it is defined as

$$\xi(|\mathbf{r}-\mathbf{r}'|) =< \delta(\mathbf{r})\delta(\mathbf{r}') > \tag{1.46}$$

while for a discrete field (a galaxy catalog) it is defined via

$$dP = \bar{n}^2(1+\xi(r_{12}))dV_1 dV_2 \ . \tag{1.47}$$

In the previous equation dP is the differential probability of finding a pair of galaxies separated by a distance r_{12}. $\bar{n}$ is the mean number of galaxies and dV_1 and dV_2 are the differential volumes of two balls whose centers are separated by a distance r_{12}. Note that in the above equations, the correlation function depends only on the modulus, not in the direction of the vector. This is because we consider that the universe is rotationally invariant.

Widely used in cosmology and enclosing the same information that the correlation function, the *power spectrum*, $P(k)$, it is defined as the fourier transform of the correlation function:

$$P(\mathbf{k}) = \int \xi(\mathbf{r}) e^{i\mathbf{k}\cdot\mathbf{r}} d^3\mathbf{r} \qquad\qquad \xi(\mathbf{r}) = \int P(\mathbf{k}) e^{-i\mathbf{k}\cdot\mathbf{r}} \frac{d^3\mathbf{k}}{(2\pi)^3} \tag{1.48}$$

The shape of the power spectrum depends on the cosmological parameters (see for example the dependence of the power spectrum shape with the masses of the neutrinos in the Figure 3.4). By using galaxy catalogs, the power spectrum can be reconstructed, at least in a range of k's (see for example [37][38][60]). The use of complementary methods such as the CMB, or the Lyman-α forest has the potential to reconstruct the power spectrum in a wide range of k, allowing therefore, a much better measure of the cosmological parameters.

As we have already explained in the subsection 1.2.2, in the primordial plasma, photons and baryons were coupled via Thompson scattering. Perturbations in that plasma, due to the presence of inhomogeneities in the matter density, led to acoustic waves which propagate through the plasma with a velocity approximately equals to $c/2$, creating density variations. Those waves are originated by counteracting forces: on one hand the excess of matter in a given place acts as an attractive force while the pressure of photons results in a repulsive force. Once photons decoupled from baryons, they were free to travel across the universe while the perturbation in the baryons kept frozen. The radius of the first wave, which travel over the plasma until photon decoupling, is known as the sound horizon. Those waves, known as BAO (Baryonic Acoustics Oscillations), left a pattern in the distribution of baryons, which can be measured by galaxy surveys. This pattern has already been found in the correlation function of galaxy catalogs as can be seen in the Figure 1.3.

The baryonic acoustic oscillations represent a cosmological standard ruler, whose size is fixed by simple physics. The detection of the baryonic acoustic oscillations at different redshifts allows to measure the *angular diameter distance* as a function of the redshift. The angular diameter distance is defined as the ratio between the size of an object, L, and the angular size of the object as seen from the earth, θ

$$d_A = \frac{L}{\theta} \ . \tag{1.49}$$

This distance depends on the Hubble function

$$d_A(z) \propto \int_0^z \frac{dz'}{H(z')} \ , \tag{1.50}$$

thus, by measuring the dependence of d_A with the redshift, we obtain information of the dependence of $H(z)$ with z and therefore we can constrain the value of the cosmological parameters.

Other important technique used to determine the cosmological parameters is the study of the *Lyman-α forest*. The spectrum of quasi-stellar objects (QSO's) that reach the earth contain lots of information about the distribution of the intergalactic medium. To understand the physics of the forest lets imaging a QSO emitting radiation with a given spectrum

$$I_{QSO} = I_{QSO}(\lambda) \ , \tag{1.51}$$

and suppose that there is a cloud of gas, containing neutral hydrogen between the earth and the quasar at a redshift z_{cloud}. When the light of the QSO penetrates the cloud, this will absorb a part of the radiation at a wavelength $\lambda_{absortion} = 1215(1+z)$ Å. When reaching the earth, the spectrum of the quasars presents structure like this presented in the Figure 1.4.

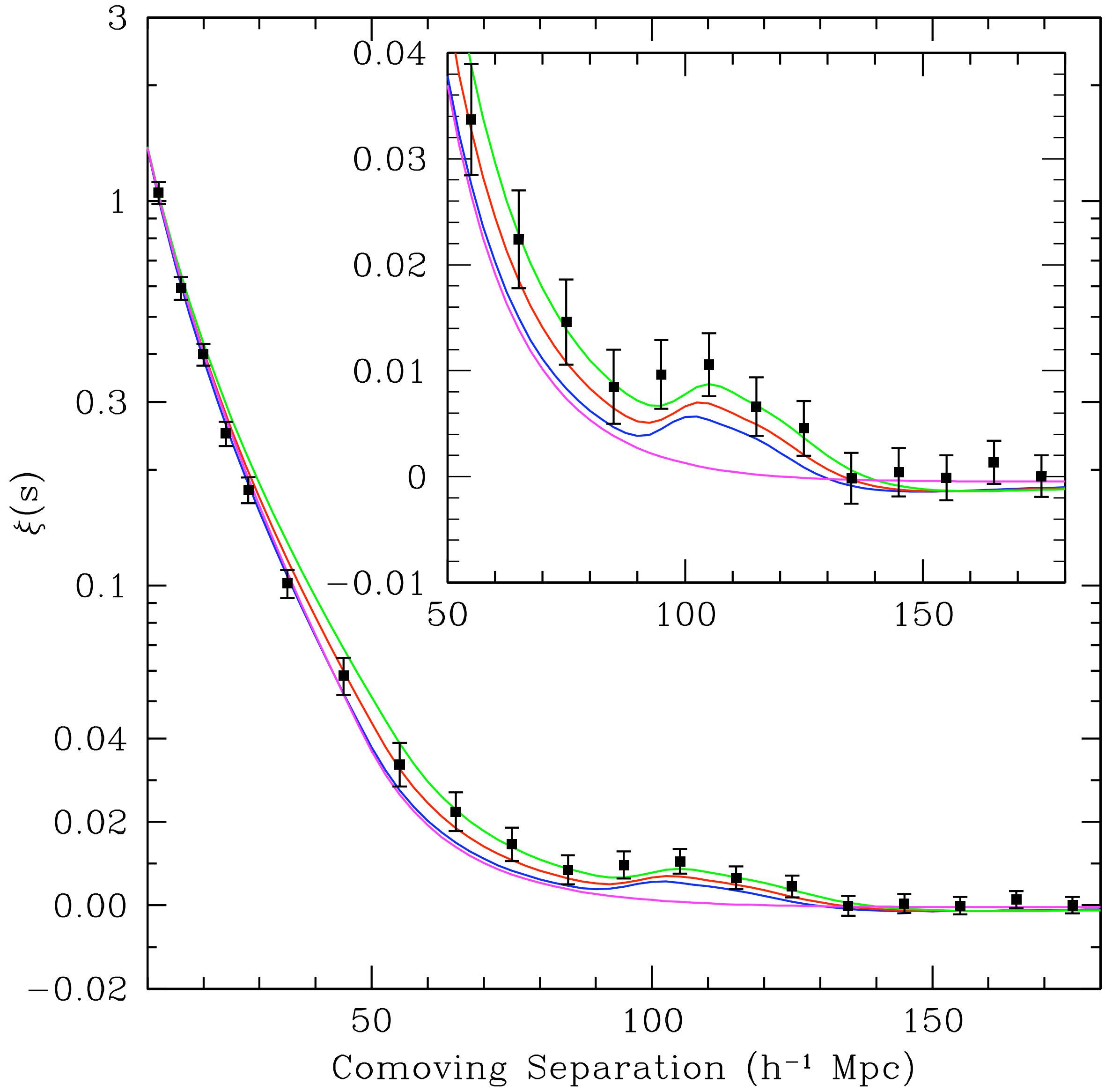

Figure 1.3: Correlation function extracted from the SDSS galaxy catalog. In the Figure, it is visible an excess of correlation at about 100 h^{-1}Mpc, showing the presence of the first acoustic peak. The colored solid lines represent the theoretical prediction of the correlation function for the following cases: green, red and blue, all of them have $\Omega_b h^2 = 0.024$ and $\Omega_m h^2 = 0.12,\ 0.13,\ 0.14$ respectively while the purple line represents a pure CDM universe, without baryons, and $\Omega_m h^2 = 0.105$. (Image taken from the reference [26])

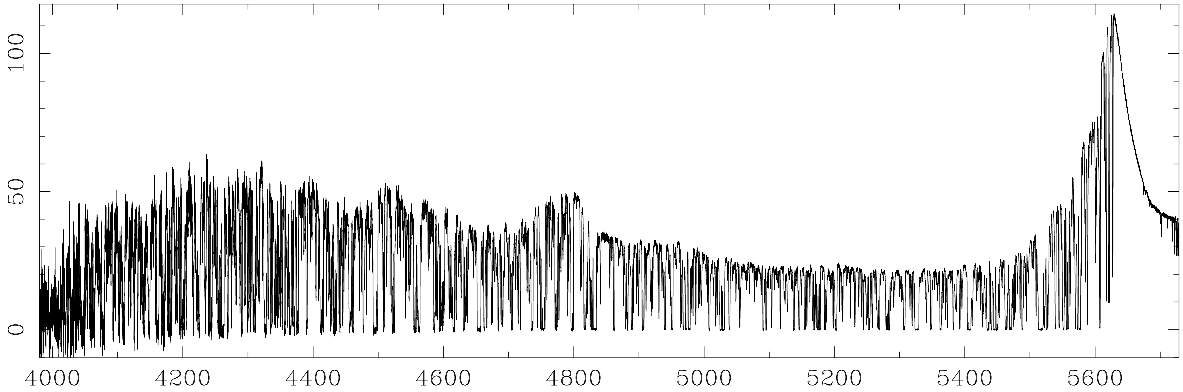

Figure 1.4: Example of the Lyman-α forest in the spectra of the QSO 1422+23.

The use of the Lyman-α forest allow the study of the distribution of the intergalactic medium at redshifts $z \sim 2 - 4$, and can be used to constrain the cosmological parameters. In the Chapter 6 we present a novel method, using the Lyman-α forest, to determine Ω_ν.

We end this chapter by showing in 1.5 the latest cosmological parameters derived from studies of CMB, BAO and supernovae.

WMAP Cosmological Parameters
Model: lcdm+sz+lens
Data: wmap7+bao+h0

$10^2\Omega_b h^2$	2.260 ± 0.053	$1 - n_s$	0.037 ± 0.012
$1 - n_s$	$0.013 < 1 - n_s < 0.061$ (95% CL)	$A_{\mathrm{BAO}}(z = 0.35)$	0.468 ± 0.011
C_{220}	5762^{+38}_{-37}	$d_A(z_{\mathrm{eq}})$	14238^{+128}_{-129} Mpc
$d_A(z_*)$	14073^{+129}_{-130} Mpc	$\Delta^2_{\mathcal{R}}$	$(2.441^{+0.088}_{-0.092}) \times 10^{-9}$
h	$0.704^{+0.013}_{-0.014}$	H_0	$70.4^{+1.3}_{-1.4}$ km/s/Mpc
k_{eq}	0.00985 ± 0.00026	ℓ_{eq}	$138.6^{+2.6}_{-2.5}$
ℓ_*	302.40 ± 0.73	n_s	0.963 ± 0.012
Ω_b	0.0456 ± 0.0016	$\Omega_b h^2$	0.02260 ± 0.00053
Ω_c	0.227 ± 0.014	$\Omega_c h^2$	0.1123 ± 0.0035
Ω_Λ	$0.728^{+0.015}_{-0.016}$	Ω_m	$0.272^{+0.016}_{-0.015}$
$\Omega_m h^2$	0.1349 ± 0.0036	$r_{\mathrm{hor}}(z_{\mathrm{dec}})$	284.6 ± 1.9 Mpc
$r_s(z_d)$	152.7 ± 1.3 Mpc	$r_s(z_d)/D_v(z = 0.2)$	$0.1904^{+0.0037}_{-0.0038}$
$r_s(z_d)/D_v(z = 0.35)$	0.1143 ± 0.0020	$r_s(z_*)$	146.2 ± 1.1 Mpc
R	$1.7239^{+0.0100}_{-0.0099}$	σ_8	0.809 ± 0.024
A_{SZ}	$0.96^{+0.69}_{-0.96}$	t_0	13.75 ± 0.11 Gyr
τ	0.087 ± 0.014	θ_*	0.010389 ± 0.000025
θ_*	0.5953 ± 0.0014 °	t_*	377730^{+3205}_{-3200} yr
z_{dec}	1088.2 ± 1.1	z_d	1020.5 ± 1.3
z_{eq}	3232 ± 87	z_{reion}	10.4 ± 1.2
z_*	$1090.89^{+0.68}_{-0.69}$		

Figure 1.5: Cosmological parameters derived from data from CMB anisotropies (WMAP), together with BAO and supernovae (H_0). (File taken from `http://map.gsfc.nasa.gov/`)

Chapter 2

Dark matter

In this chapter we present the huge evidence in favour of the existence of the dark matter, the most popular candidates to furnish it and we end the chapter by describing a very popular tool in cosmology, the N-body simulations. We also introduce the problems related with those cosmological simulations which represent a challenge for the standard cosmological model.

2.1 Observational evidence

The evidence of the presence of dark matter is overwhelming. From the first clues discovered by Zwicky in 1933 to the recent discover of the bullet cluster, the existence of dark matter in the universe is supported by many observations. In this section we review the most important ones. For a review on this topic we refer to [76][7].

2.1.1 Gravitationally bound systems

The first clue about the existence of the dark matter was found by Fritz Zwicky in 1933 [108] after studying the properties of the Coma cluster. Using the virial theorem, he concluded that the mass of the Coma cluster exceed by many times the mass estimated from the visible matter. In this subsection we introduce the virial theorem and we show how Zwicky reached the conclusion of the presence of dark matter in the Coma cluster.

Lets assume that a cluster of galaxies contains N galaxies, each of them having an average mass M_g and moving within the cluster at a mean velocity V_g. The total kinetic energy of that system is given by

$$T = \frac{1}{2} N M_g V_g^2 \ . \tag{2.1}$$

For a cluster with N galaxies the number of pairs of those is $N(N-1)/2$, thus, the total potential energy is

$$U = -\frac{1}{2}N(N-1)\frac{GM_g^2}{R} \ , \tag{2.2}$$

where R is the average distance between galaxies. The virial theorem states that for a stable, self-gravitating system made of objects with the same mass and spherically symmetric, the total kinetic energy is equal to minus one half the total potential energy of the system

$$T = -\frac{1}{2}U \ . \tag{2.3}$$

The total mass of the cluster can be therefore estimated by making use of this theorem and by measuring both R and V_g

$$M_{cluster} = NM_g \cong \frac{2RV_g^2}{G} \ . \tag{2.4}$$

Zwicky measured the size of the Coma cluster and the radial velocities of the galaxies within it and applied the virial theorem to compute the total mass of the cluster. He found that the Coma cluster mass should be larger that its visible mass by several hundreds of times. Zwicky concluded that the Coma cluster was filled with some sort of non-visible matter which was responsible of holding the cluster together.

2.1.2 Spiral galaxies rotation curves

Another clue of the existence of the dark matter comes from the rotation curves of spiral galaxies, which point out to the existence of a halo of dark matter in them.

Spiral galaxies are a type of galaxy that consist of a flat, rotating disk containing stars and gas, and a central concentration of stars known as the bulge. Both, stars and gas in the thin disk, rotate around the center of the galaxy in almost circular orbits. The velocity profile of the galaxy can be easily computed by equaling the centrifugal force mv^2/r and the gravitational strength $GM(r)m/r^2$, where m is either the mass of the gas particle or the mass of star and $M(r)$ is the mass inside a sphere of radius r.

$$v = \sqrt{\frac{GM(r)}{r}} \tag{2.5}$$

We would naively expect that far from the center of the galaxy, the function $M(r)$ would not grow much, and thus, the velocity profile would decrease as $\sim 1/\sqrt{r}$. Surprisingly, this

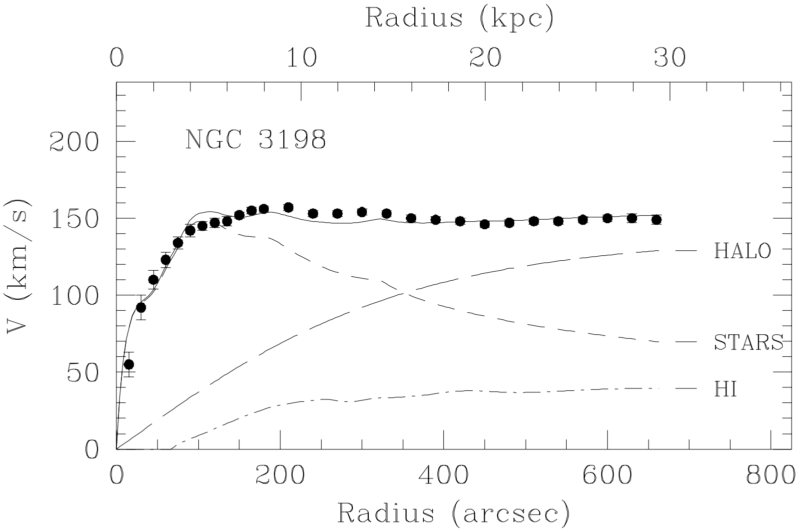

Figure 2.1: Rotation curve of the galaxy NGC 3198. At large radii the velocity profile flattens out, a behavior which can not be explained by the mass of the galaxy disk alone. A dark matter halo is needed to reproduce the observed profile. Image taken from [10]

behavior is not observed when measuring the galaxy rotation curves. In contrast, a nearly constant velocity is obtained for radii larger than $\sim 5\ kpc$.

In Figure 2.3, the measured velocity profile of the galaxy NGC2198 is plotted. The contribution from the mass of the disk is not enough to account for the observed rotation curve. A dark matter halo is needed to reproduce it.

2.1.3 X-rays

The intracluster medium (ICM) is filled with hot gas as X-ray observations point out. Assuming that this gas is in hydrostatic equilibrium and is spherically symmetric, the following equality can be written

$$\frac{GM(r)}{r^2} = \frac{1}{\rho(r)}\frac{dP(r)}{dr}\ , \tag{2.6}$$

where $M(r)$ is the total mass inside a sphere of radius r, $\rho(r)$ is the gas density profile and $P = nk_BT$ is the gas pressure. Using the gas temperature $T(r)$ and the gas density $\rho = \mu m_p n$, with $\mu = 0.61$ being the average gas particle mass in terms of the proton mass m_p, it is possible to derive the mass profile $M(r)$ of the galaxy cluster.

Studies of this type yield to $M_{total}/M_b \geqslant 3$, indicating that the baryonic mass of the cluster represents, at most, one third of its total mass. Therefore, a non-baryonic mass

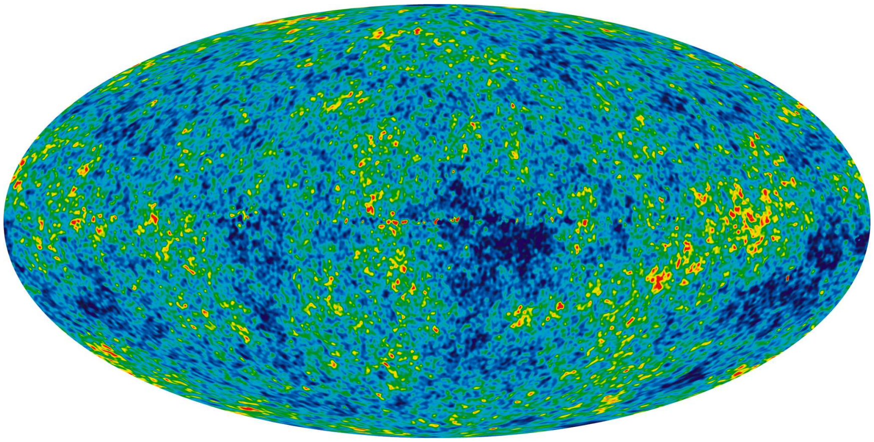

Figure 2.2: CMB temperature map of WMAP 7yr release. Colors indicate deviations from the average in the range -200 μK (black) to $+200$ μK (red). Image taken from `http://lambda.gsfc.nasa.gov`.

component is needed to reproduce the observed density and temperature profile of the cluster.

2.1.4 Gravitational lensing

Given that light follows space-time geodesics, it is expected that the trajectory of photons from an astrophysical source (e.g. a star or quasar) would be deviated when approaching into the gravitational potential created by a galaxy, cluster of galaxies...etc.

In 1919 Sir Arthur Eddington verified the deflection of light rays coming from stars near the direction of the sun during an eclipse. This is considered as the first proof in favour of general relativity.

Gravitational lensing allows to measure the matter distribution in the lens (the astrophysical object whose gravitational field deflects the light) by studying the spatial distribution of the lensed object (see [77] for a review). The results show clearly that the mass inside lens systems such as galaxies or clusters is much larger that the one observed by comparing the mass to light ratio $\Upsilon = M/L$ measured with the one expected. Therefore, a significant amount of matter in those systems is contributing to the total mass but not to the brightness. The most simple explanation for this phenomena is the presence of the dark matter within those objects.

2.1.5 Cosmic microwave background

The discovery of the cosmic microwave background (CMB) in 1964 [71] started an era of precision in cosmology. As we have seen in the section 1.2.2, the CMB has been widely used to constrain the cosmological parameters. The study of the anisotropies in the temperature background of the CMB and in particular the study of correlations of those at different angular sizes of the sky has allowed a measurement of the content of dark matter in the universe. The third peak in the $C_l = C_l(l)$ function (see Figure 1.2) contains information on Ω_m. Therefore, by measuring its position, height and shape it is possible to infer that there must be a dark matter component in the universe.

The current measurements indicate that the energetic content of the universe is made up of baryons ($\sim 4.5\%$), dark matter ($\sim 23\%$) and dark energy ($\sim 72\%$).

2.1.6 Baryonic Acoustic Oscillations

As we have explained in the section 1.2.3, in the primordial plasma, photons and electrons were coupled via Thompson scattering. The anisotropies in the matter density field led to acoustic waves which propagated throughout the plasma until the time of decoupling. Those waves left an imprint in the baryon distribution which can be observed in galaxy surveys.

Those waves, whose radii can be easily computed, represent a standard ruler since its size remain fixed after decoupling. The scale of BAO depends on the dark matter content of the universe and on the Hubble constant, h. The ratio Ω_b/Ω_m can be measured and results in a value of 0.18 ± 0.04, in very good agreement with the CMB measurements.

2.1.7 Bullet cluster

The merging galaxy cluster 1E0657-56 [59], also known as the bullet cluster, is the result of the collision between two galaxy clusters. It represents one of the most direct evidences of dark matter and a challenge for theories such as MOND (MOdified Newtonian Dynamics).

Gravitational lensing has found that most of the mass of the system is in two different regions of the cluster, while the strongest emission from X-rays does not take place in those regions. In the Figure 2.4 we show in green lines the mass contours from weak lensing reconstruction while the X-rays emission is drawn on top of it. The most plausible explanation for this configuration is that two galaxy clusters collided and while both, stars and dark matter, were not strongly affected by the collision and the majority of them passed right through, gravitationally slowed by the mass of the other cluster, the gas present in both clusters interacted electromagnetically with each other during the collision, slowing down their velocities. This description explains very well the morphology of the bullet cluster while theories such as MOND needs of pretty exotic scenarios to reproduce that configuration.

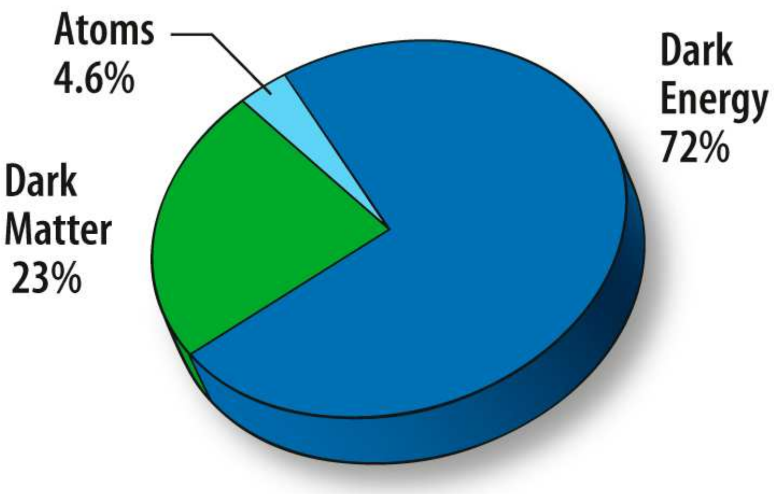

TODAY

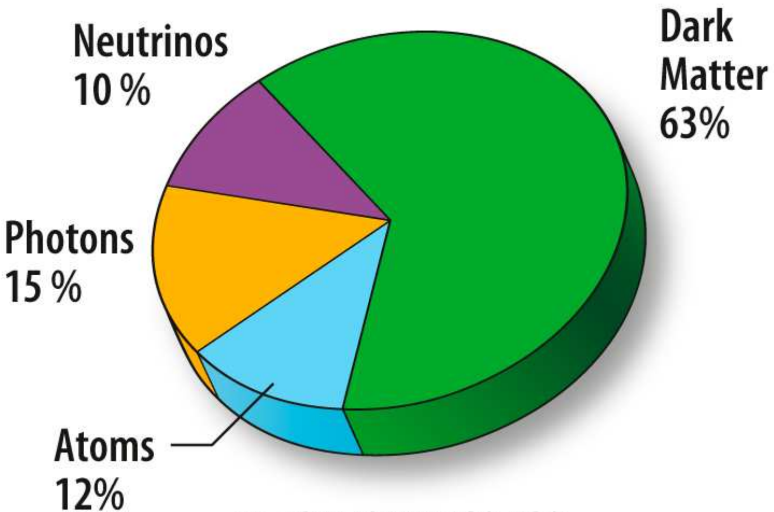

13.7 BILLION YEARS AGO
(Universe 380,000 years old)

Figure 2.3: Universe energetic content. Image taken from `http://lambda.gsfc.nasa.gov`.

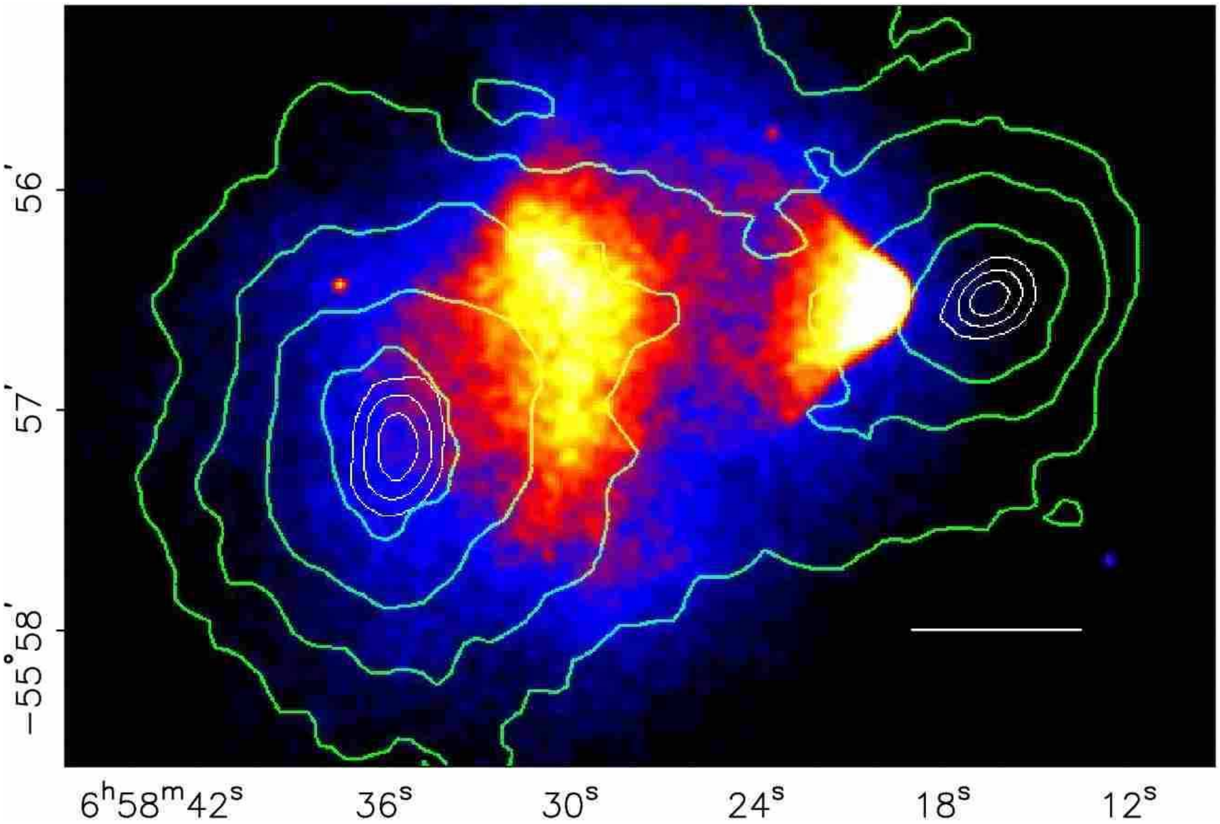

Figure 2.4: The bullet cluster. The green lines represent the mass contours as measured by weak lensing and the colored regions show the temperature of the gas. The simpler explanation for this morphology is the following: two galaxy clusters collided and while both, stars and dark matter, were not strongly affected by the collision and the majority of them passed right through, gravitationally slowed by the mass of the other cluster, the gas present in both clusters interacted electromagnetically with each other during the collision, slowing down their velocities. Image taken from [18].

2.2 Candidates

As we have described in the previous section, the presence of dark matter is supported by many independent observations. In this section we briefly review the possible candidates to constitute the dark matter[1]. We emphasize that dark matter has only been detected so far by gravitational methods that do a collective detection which does not allow to distinguish among many candidates, and not through other interactions.

2.2.1 MACHO's

One of the possible candidates to dark matter may be objects which have very low or null luminosity such as planets, brown dwarfs, neutron stars or black holes. Those objects are embedded into the category of Massive Astrophysical Compact Halo Objects (MACHO's) and the advantage of considering them is that they are made of baryonic matter, so there is no necessity of introducing any other particle beyond the standard model.

The hypothesis that the dark matter is made of objects with a low or null luminosity can be tested by searching for microlensing events that would take place when one of those astrophysical objects pass in front of or nearly in front of a star. The MACHO project reported $13 - 17$ microlensing event after 5.7 years of photometric observation on 11.9 millions of stars [3]. This number rules out the possibility that all dark matter is made up of MACHO's. We emphasize that dark matter being all baryonic is also ruled out by the fact that Ω_m is measured to be around 0.25 and primordial nucleosynthesis shows that baryons have Ω_b about 0.05.

2.2.2 WIMP

The particle standard model presents some problems such as the neutrino masses, which this model predicts to be zero while neutrino oscillation experiments have shown that the neutrinos have a mass of at least $\Sigma m_\nu \sim 0.05$ eV. Extensions of the standard model represent a natural way to solve those problems. One of those extensions is the so called supersymmetry. In supersymmetry, each particle of the standard model has a superpartner which differs from it by 1/2 in spin. In other words, each boson in the standard model is associated with a supersymmetric fermion and each standard model fermion is associated with a supersymmetric boson. If this symmetry would be perfect, the masses of the superpartners would be the same of their associated standard model particles. Given that these particles have not been found, this symmetry must be broken, allowing superpartners to be heavier than the standard model particles. In many models, supersymmetry assigns a new multiplicative quantum number, R, which is $+1$ for standard model particles and -1 for supersymmetry particles. This number is conserved in any reaction, which means that the

---

[1] We note that the list of candidates to furnish the dark matter is very long, however, in this thesis we only present the most popular among them.

lightest supersymmetry particle must be stable and that it could only decay to standard model particles by annihilation with itself. The name WIMP arises from *Weakly Interacting Massive Particles* and supersymmetry introduces a candidate in a very natural way.

Lets suppose that the number density of those WIMP particles is n, then, the annihilation rate per particle-antiparticle is given by $n < \sigma v >$, where $< \sigma v >$ is the average value of the product of the annihilation cross section and the relative velocity. The total number of particles in a box of co-moving volume a^3 is na^3, and the rate of decrease in the number of particles due to particle-antiparticle annihilations is given by $na^3 \times n < \sigma v >$. Apart from this rate of decrease in the number of particles, there is a production rate in the number of those particles by pair creations from the background equals to $n_{eq}a^3 \times n_{eq} < \sigma v >$, where n_{eq} is the number density of particles and antiparticles in equilibrium at a given temperature. The equation governing the evolution of the number density of these particles is then given by

$$\frac{d(na^3)}{dt} = -\left(n^2 - n_{eq}^2\right)a^3 < \sigma v > \quad . \tag{2.7}$$

At high temperature, $k_B T \gg m$, the solution of previous equation is just $n = n_{eq}$, showing that particles and antiparticles are in thermal equilibrium in the plasma. As the temperature drops by the expansion of the universe, the annihilation rate decreases and eventually, when the universe expansion rate H excess the rate of annihilation, the density of the particles can not decrease further. The particle relic abundance is then set up.

Assuming that the annihilation of particles and antiparticles took place in the radiation domination era, it can be shown that the current density of those particles in units of the critical density of the universe Ω_{WIMP}, is (for a detailed derivation see section 3.4 of [104])

$$\Omega_{WIMP} = 11.5h^{-2}\big(m(GeV)\big)^{-1.85}\big(\mathcal{F}/\sqrt{\mathcal{N}}\big)^{-0.95} \quad , \tag{2.8}$$

where $\mathcal{F}$ is a fudge factor that contains information about the number of annihilation channels and the details of the interaction responsible for the annihilation and $\mathcal{N}$ is the number of particle types. In the regime where $k_B T \ll m$, $< \sigma v >$ is proportional to m^2, and therefore, it is not surprising the dependence on m in the previous equation, indicating that heavy particles annihilate more effectively than light ones. The importance of these types of particles is that they can naturally reproduce a the cosmological value for Ω_m equals to $\Omega_m \sim 0.3$ by simply assuming that those particles have a mass in the range 10 GeV-1 TeV.

Due to the fact that the superpartners of the Z boson (zino), the photon (photino) and the neutral higgs (higgsino) have the same quantum numbers, they can mix and the mass operator has 4 eigenstates. Those eigenstates are called neutralinos, and the lightest one is stable under the assumption of R symmetry. This particle is a Majorana fermion (i.e. neutralino is its own antiparticle) and electrically neutral, and in many supersymmetric models is the LSP (*lightest supersymmetric particle*), making it the best candidate to dark matter.

Because those particles only feel the weak and the gravitational interaction, its detection is challenging. One of the standard ways to search for those particles is by looking at the recoils they produce in atomic nuclei when they collide with them. So far, no conclusive evidence of its existence has been found.

2.2.3 Axions

Axions are other possible candidate to dark matter. These particles appear as a natural solution to the strong CP problem in QCD (*quantum chromodynamics*). This problem arises as a consequence that there is no theoretical motivation that implies that CP symmetry must be conserved in QCD theory. Therefore, when we write all possible terms in the QCD lagrangian, one of them, which violates CP, appears naturally. This term implies that the neutron must have an electric dipole moment. In order to satisfy the experimental bounds on this quantity, the coefficient of this CP violating term must be extremely small. The reason why this term is so small or null represents a problem for QCD.

As a possible solution to this problem, Peccei and Quinn [69] postulated a new symmetry, the Peccei-Quinn symmetry, that becomes spontaneously broken. When this symmetry is broken a new particle, the axion, appears. The role of the term that breaks CP symmetry in the QCD lagrangian is now played by the axion.

Axions would be electrically neutral, have a very small mass, and very low cross-section for weak and strong forces. Due to this weak interactions, they were not in thermal equilibrium with other particles. Despite their very small mass, they can be cold (i.e. have very small velocities). These properties make them to be a very plausible dark matter candidate. Axions can couple to photons in the presence of strong magnetic fields, this feature has been used to search for cosmological axions or set bounds on their mass and cross-section (e.g. [81][82][63]). No signal has been detected so far.

In some supersymmetric theories, axino (the superpartner of the axion) would be the lightest supersymmetric particle with $R = -1$, and hence stable. These axinos may or may not be produced thermally, and they are another candidate for the dark matter constituent.

2.3 Dark matter cosmological simulations

One way to study the impact of the dark matter in the universe is by running cosmological simulations in a supercomputer. By studying the results of those simulations and comparing them with observations, it is possible to obtain a large amount of information about the physics involved in the process of structure formation.

Structures observed in the universe such as planets, stars, galaxies, clusters of galaxies and voids are the result of the non-linear process of structure formation. At the CMB epoch, the universe was highly homogeneous. Inhomogeneities in the density field were below one part over ten thousand:

$$\left(\frac{\delta\rho}{\overline{\rho}}\right)_{CMB} \leqslant \ 10^{-5} \ . \tag{2.9}$$

Nowadays, the mass of bounded objects range from $\sim {M_J}^2$ for planets to $\sim 10^{15}\ M_\odot$ for large clusters of galaxies while radii remain between $\sim {r_J}^3$ (planets) to $\sim$ Mpc (clusters). This translates into densities ranging from $\sim 10^{43}\ M_\odot/\mathrm{Mpc}^3$ for planets to $\sim 10^2\ M_\odot/\mathrm{Mpc}^3$ for clusters of galaxies. By comparing this range with the mean density of the universe $\sim 1\ M_\odot/\mathrm{Mpc}^3$ it is obvious that the universe is highly inhomogeneous at the current time on scales smaller than $\sim 100\ h^{-1}$Mpc.

The process of transforming very small inhomogeneities (CMB) to large density contrast (planets, galaxies...etc) is driven mainly by gravity. The Friedmann equations 1.17 govern the evolution of the universe background. It can be shown that the evolution of a isolated small density perturbation δ is described in a expanding universe by the following equation (see for example the chapter 6 in [65]):

$$\ddot{\delta} + 2H\dot{\delta} - \frac{c_s^2}{a^2}\triangle\delta - 4\pi G\overline{\rho}\delta = 0 \ , \tag{2.10}$$

where $\delta = \delta\rho/\overline{\delta}$ is the density contrast and c_s is the sound speed $c_s^2 = (\partial p/\partial\rho)_S$,

$$\delta p = c_s^2\delta\rho + \sigma\delta S \ , \tag{2.11}$$

being S the entropy. To study the evolution of the whole dark matter distribution, a more general description is needed. Dark matter is commonly described as a collisionless fluid. As that, it satisfies the collisionless Boltzmann equation (also known as Vlasov equation)

$$\frac{\partial f}{\partial t} + \mathbf{v}\frac{\partial f}{\partial \mathbf{x}} - \frac{\partial \Phi}{\partial \mathbf{x}}\frac{\partial f}{\partial \mathbf{v}} = 0 \ , \tag{2.12}$$

where $f = f(\mathbf{x}, \mathbf{v}, t)$ is the phase-space distribution function which fully describe the fluid, $\mathbf{x}$ and $\mathbf{v}$ are the position and velocity vectors and Φ is the gravitational potential which satisfy the Poisson equation

$$\nabla^2\Phi(\mathbf{x}, t) = 4\pi G\rho(\mathbf{x}, t) \ . \tag{2.13}$$

$\rho(\mathbf{x}, t)$ is the density field which is connected with the distribution function by

---

[2] M_J means the mass of Jupiter. $M_J = 1.9 \times 10^{27}$ kg

[3] r_J means the radius of Jupiter. $r_J =\sim 70.000$ km

$$\rho(\mathbf{x}, t) = \int d\mathbf{v} f(\mathbf{x}, \mathbf{v}, t) \tag{2.14}$$

The Boltzmann equation 2.12 is a set of 6 coupled partial differential equations. Solving this equation by using finite difference techniques is nowadays impracticable. One way to approach to the solution of this equation is by a Monte-Carlo realization which is called *N-body simulation.* N-body simulations consist of a set of particles simulating the phase-space density $f(\mathbf{x}, \mathbf{v}, t)$, the higher the number of particles the better the function f is sampled. The evolution of f is obtained by following the evolution of the particle system under their self-gravity.

The initial conditions for those simulations are set up using the power spectrum generated by inflation and evolved linearly until the initial redshift of the simulation (typically computed via CAMB[4]). The simulation is typically performed in a periodic boundary cubic box in comoving coordinates. All the particles in the simulation have the same mass and this mass is constrained by the requirement that their total mass reproduces the mean matter density $\rho_m = \Omega_m \rho_c$ in the simulation box. Therefore, if the simulation contains N particles in a periodic box of comoving length L, the resolution of the simulation (the mass of a single particle, m_p) is given by:

$$m_p = \rho_m^0 L^3 / N \tag{2.15}$$

Some N-body codes allow to perform simulations which include baryons, star formation, neutrinos...etc. In the Figure 2.5 we show the result of one of these N-body simulations carried out with the code GADGET[5]. The biggest constrain of these simulations comes from the computational time required to perform them. If a high resolution is wanted, then the box should be small and the number of particles large. In contrast, sometimes it is not needed a high resolution but a large number of for example dark matter halos. In this case we should choose a big box and the maximum number of particles that our resources allow us.

N-body simulations with the ΛCDM model are in good agreement with a wide range of observations such as the abundance of clusters at $z < 1$ or the galaxy-galaxy correlation function [87]. However, there some important discrepancies, among them we emphasize:

- *Satellite halos problem.* N-body simulations produce a number of satellite halos around Milky Way-sized halos that exceeds the observed number of dwarf galaxies. This problem has been alleviated recently from the discovery of low luminosity dwarf galaxies in the SDSS catalog [83].
- *Cusp-Core problem.* N-body simulations produce cusp dark matter density profiles, while observations of LSB (*Low Surface Brightness*) galaxies indicate that density profiles have a prominent core.

---

[4] `http://camb.info/`

[5] `http://www.mpa-garching.mpg.de/gadget/`

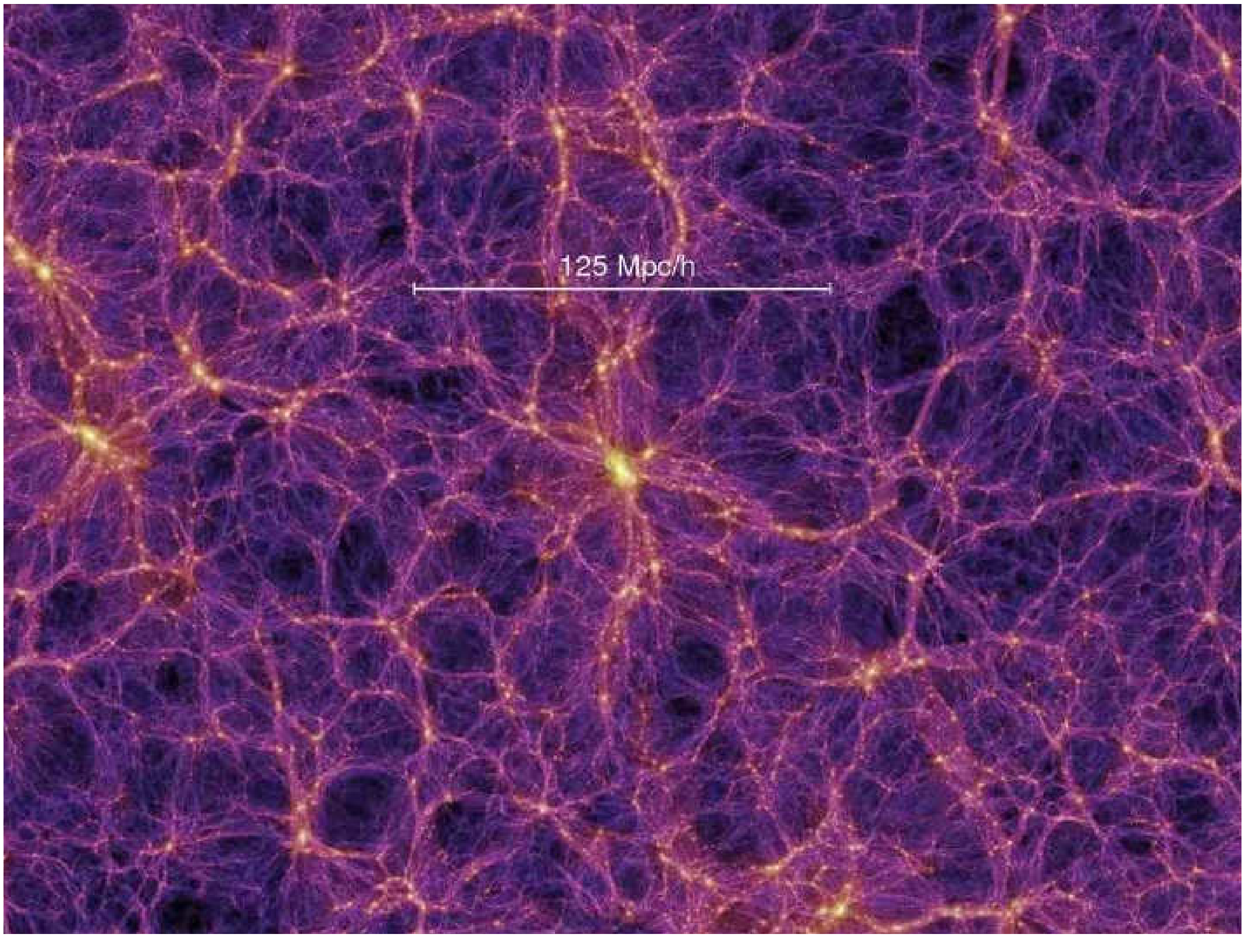

Figure 2.5: N-body snapshot of the millennium simulation. (Image taken from `http://www.mpa-garching.mpg.de/gadget/`)

In this thesis we investigate the hypothesis proposed by several authors that these problems can be solved by considering that the dark matter is warm rather than cold. The difference between cold and warm is due to the velocity dispersion of cold dark matter particles. Cold dark matter particles are supposed to have a negligible velocity dispersion at all epochs, while warm dark matter would have a velocity dispersion high enough so those particles free stream over a length of $\sim 100\ h^{-1}$kpc. By making this, the number of small halos would be reduced considerably because halos would have a natural minimum size given by the velocity dispersion of dark matter particles. It could also alleviate the problem with cusp dark matter halos since phase-space density arguments implies the presence of a core for halos formed of particles with a non-null velocity dispersion. In the chapter 4 we answer the question whether warm dark matter is able to create cores in the dark matter density profile as large as the observed in the LSB galaxies.

Chapter 3

Cosmological Neutrinos

In this chapter we introduce the neutrinos and its main properties. We discuss in detail the neutrino oscillations and the current bounds in the mass of them. We present the cosmological neutrinos, as predicted by the standard cosmological model and we end the chapter describing the main effects that those neutrinos induce in cosmology in the linear regime.

3.1 Introduction

Neutrinos were theoretically postulated in 1930 by Wolfgang Pauli in order to avoid the problems of violation of energy, momentum and spin in the beta decay process

$$n \longrightarrow p^+ + e^- + \overline{\nu}_e \, . \tag{3.1}$$

The implications of that hypothesis were:

- Neutrino mass has to be small.
- Neutrinos have to be electrically neutral.
- Neutrinos should not be affected by the strong interaction.

Neutrinos were detected experimentally on 1956 in an experiment carried out by Clyde Cowan and Frederick Reines [22]. They used a source of $\sim 5 \times 10^{13}$ ν/s, coming from a nuclear reactor, and they searched for signals of the reaction

$$\overline{\nu}_e + p^+ \longrightarrow n + e^+ \, . \tag{3.2}$$

The positron generated in that reaction disintegrates quickly with an electron e^-, producing a pair of gamma rays. The detection of those gamma rays plus the delayed neutron capture produce a clear signature of the existence of neutrinos. That signal was found by Cowan and Reines in its famous experiment, demonstrating experimentally the existence of the neutrinos.

Neutrinos are a component of the particle standard model. They are fermions with spin 1/2 and within this model they are massless particles. The decay of the Z boson indicates that the number of neutrinos that are sensitive to weak interactions is $N_\nu = 2.994 \pm 0.012$ [68]. Due to their very small cross section, the detection of neutrinos is particularly challenging. As we explain in detail below, we know from neutrino oscillation experiments that the mass, of at least two of them, is non-zero. This suggests that the standard model of particle physics should be extended to explain the neutrino masses and to accommodate a particle (or several) that furnish the dark matter.

3.2 Masses

For almost 40 years, a major discrepancy took place between the measured number of neutrinos that reached the earth coming from the sun and the expected number of those computed from theoretical models of the interior of the sun. This discrepancy is known as the *solar neutrino problem*:

Neutrinos are produced in the core of the sun by nuclear processes such as

$$ {}^1_1H \; + \; {}^1_1H \; \longrightarrow \; {}^2_1H \; + \; e^+ \; + \nu_e \; . \tag{3.3} $$

Those neutrinos, due to their weak cross section, travel to the earth with almost no interactions with other particles. However, the number of neutrinos that reach the earth, as measured by experiments, is about a factor 3 smaller than the prediction from theoretical models.

The solution to this puzzle comes from the so-called *neutrino oscillations*, driven the neutrino mass: in the sun, neutrinos are produced as electron neutrinos, ν_e, by reactions such as 3.3, but there is a non-zero probability that those neutrinos change their flavour in their way to earth. About 2/3 of the most energetic electron neutrinos produced in the core of the sun oscillate, changing their flavour to μ-neutrinos, ν_μ, in their way to earth. As a consequence, the number of energetic neutrinos (in the range of several MeV) sensitive to detection is reduced to 1/3, explaining the discrepancy between the expected number from theoretical models and the observed number as measured by experiments. This solution was also confirmed by the observation of the $\overline{\nu}_e$ reactor neutrinos disappearance in the Kamland detector.

Other illustrative example involving neutrino oscillations comes from the so-called *atmospheric neutrinos*: cosmic rays collide with particles in the atmosphere of the earth producing, among others particles, pions π^+. The decay of these pions into other lighter particles produce neutrinos:

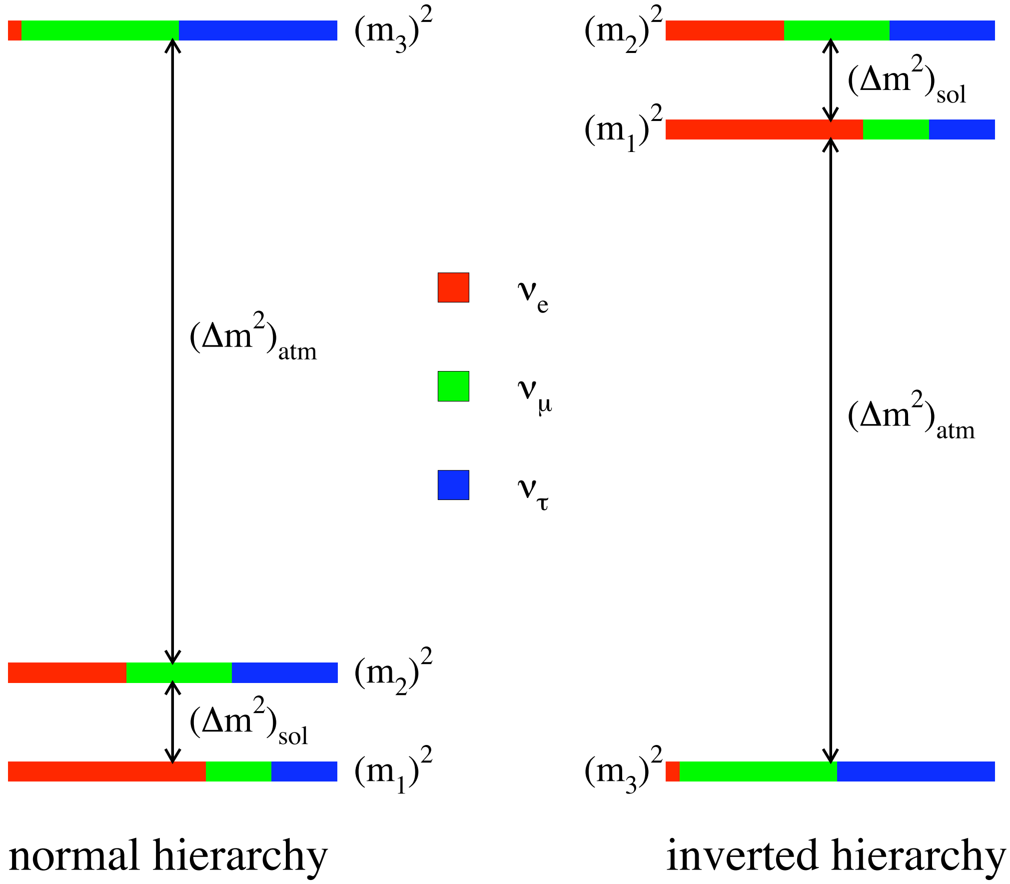

Figure 3.1: Neutrino hierarchy. Depending on the sign of $\triangle m^2_{31}$, the neutrino masses can follow the normal (positive sign) or inverted (negative sign) scheme. Image taken from [24]

$$\pi^+ \longrightarrow \mu^+ + \nu_\mu \ , \tag{3.4}$$

and

$$\mu^+ \longrightarrow e^+ + \nu_e + \overline{\nu}_\mu . \tag{3.5}$$

From the above reactions we could predict that the proportion of μ-neutrinos to electron neutrinos would be 2:1. The neutrino detectors, which are sensitive to the angle in which neutrinos enter through them, demonstrate that the proportion of $\mu - neutrinos$ to electron neutrinos is 2:1 if the neutrinos come from the region of the atmosphere above the detector, whereas the proportion is just 1:1 if the neutrinos come from the region of the atmosphere above the antipodes of the detector, i.e. neutrinos that are produced in the diametral opposite part of the atmosphere above the detector and travel across the earth until they reach the detector. The reason why the proportion of μ-neutrinos to electron neutrinos depends on the direction in which neutrinos come is because, there is a probability that some μ-neutrinos oscillate and change their flavour to τ-neutrinos and this probability depends on the distance that neutrinos have travelled until the reach detector. Within the shorter distance to the detector, the one between the detector and neutrinos produced above it, this probability is so small that the ratio 2:1 in which they are produced is conserved until its detection. In contrast, when the neutrinos have to travel through the earth to reach the detector, this probability rises and can make that half of the μ-neutrinos oscillate to τ-neutrinos. This solution was also confirmed by the disappearance of ν_μ and $\overline{\nu}_\mu$ neutrinos produced in accelerators and detected at a distance of several hundred kilimeters (K2K, MINOS).

Neutrinos are produced as flavour eigenstates ν_e, ν_μ or ν_τ but they propagate as mass eigenstates ν_1, ν_2 or ν_3. The relation between mass and flavour eigenstates is given by:

$$\begin{pmatrix} \nu_e \\ \nu_\mu \\ \nu_\tau \end{pmatrix} = \begin{pmatrix} 1 & 0 & 0 \\ 0 & c_{23} & s_{23} \\ 0 & -s_{23} & c_{23} \end{pmatrix} \begin{pmatrix} c_{13} & 0 & s_{13}e^{-i\delta} \\ 0 & 1 & 0 \\ -s_{13}e^{i\delta} & 0 & c_{13} \end{pmatrix} \begin{pmatrix} c_{12} & s_{12} & 0 \\ -s_{12} & c_{12} & 0 \\ 0 & 0 & 1 \end{pmatrix} \begin{pmatrix} \nu_1 \\ \nu_2 \\ \nu_3 \end{pmatrix} ,$$

where c_{ij} =cos θ_{ij} and s_{ij} =sin θ_{ij} with $i, j = 1, 2, 3$ and δ being the CP-violating phase. Each mass eigenstate receive contributions from the three flavour eigenstates and those contributions change with time as neutrino propagates. The observation of these time dependent contributions (oscillations) implies that neutrinos can not be all massless. Those oscillations, as measured from solar, reactor, atmospheric and accelerated neutrinos, give us information on the square difference of the neutrino mass eigenstates and in the mixing angles $sin\ \theta_{ij}$ (see for example [33]):

$$\triangle m_{21}^2 = (7.6 \pm 0.2) \times 10^{-5}\ eV^2 \ , \tag{3.6}$$

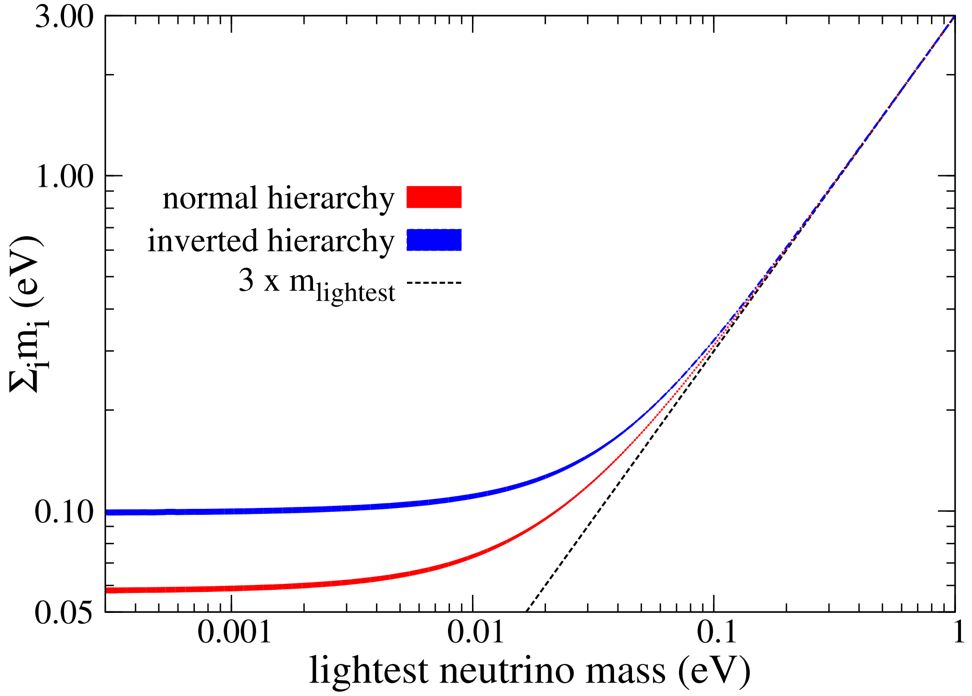

Figure 3.2: $\Sigma_i m_{\nu_i}$ as a function of the mass of the lightest neutrino for both hierarchies. For masses of neutrinos larger than $\sim$ 0.2 eV, the 3 neutrino masses are almost perfectly degenerates.

$$|\triangle m^2_{31}| = (2.4 \pm 0.1) \times 10^{-3}\ eV^2\ . \tag{3.7}$$

$$\theta_{12} = 34.4 \pm 1.0 \tag{3.8}$$

$$\theta_{23} = 42.8^{+4.7}_{-2.9} \tag{3.9}$$

$$\theta_{13} = 5.6^{+3.0}_{-2.7} \tag{3.10}$$

$$\delta_{\rm CP} \in [0, 360] \tag{3.11}$$

Running oscillation experiments pursue to measure those parameters (with special attention to θ_{13} and $\delta_{\rm CP}$). The first difference $\triangle m^2_{21}$ indicates that the mass eigenstate m_2 must have a mass larger than 8.7×10^{-3} eV. In contrast, the square difference $\triangle m^2_{31}$ can be positive or negative. This gives place to two different neutrino mass schemes called *normal hierarchy* and *inverted hierarchy* depending on the sign (positive or negative) of $\triangle m^2_{31}$. In the Fig. 3.1 we show the two different hierarchies and the distribution of masses associated with them. In the Fig. 3.2 we plot, for the two schemes, the sum of the three neutrinos masses, $\Sigma_i m_{\nu_i}$, as function of the mass of the lightest one. From that Figure we can see that for neutrino masses larger than $\sim$ 0.2 eV, the three neutrino masses are almost degenerated. In the normal hierarchy scheme, the minimum value for the sum of neutrinos masses is $\Sigma_i m_{\nu_i} \simeq 0.06$ eV while in the inverted hierarchy scheme, this value becomes $\Sigma_i m_{\nu_i} \simeq 0.1$ eV.

The current upper limits on the mass of the electron neutrino from particle experiments alone come from the tritium beta decay. At 95% CL the electron neutrino mass is below $m < 2.05 - 2.3$ eV [53][48]. Starting on 2012, the KATRIN experiment [45] is expected to measure neutrino masses in the range $0.3 - 0.35$ eV. Doble beta decay experiments will also put constrains on neutrino masses and is expected to answer the question whether neutrinos are Dirac or Majorana particles.

Cosmological bounds are much stronger, putting upper limits on the sum of the masses of neutrinos, $\Sigma_i m_{\nu_i}$, below ~ 1 eV. The anisotropies in the cosmic microwave background (CMB) are sensitive to neutrino masses. Constraints from WMAP7 alone yield to $\Sigma_i m_{\nu_i} <$ 1.3 eV [47], while combined with large scale structure (LSS) measurements, put a limit in the mass of $\Sigma_i m_{\nu_i} < 0.3$ eV [99, 89, 34, 73]. The tightest 2σ upper limit of $\Sigma_i m_{\nu_i} < 0.17$ eV, is obtained by combining CMB, LSS and Lyman-α forest [79] data sets (see [1] for a summary of current and future neutrino mass constrains). We note however that these constrains are very model-dependent and need to assume a particular model for the universe.

3.3 Relic neutrinos

In the first instants after the Big Bang, neutrinos were in thermal equilibrium with other particles in the primordial plasma by reactions such as

$$e^+ \ + e^- \longrightarrow \ \nu \ + \ \overline{\nu} \ . \tag{3.12}$$

While in thermal equilibrium, the number density of neutrinos with mass m_ν and momentum between p and $p + dp$ is given by the Fermi-Dirac distribution

$$n_\nu(p, T) = \frac{4\pi g p^2}{(2\pi\hbar)^3} \left(\frac{1}{e^{\sqrt{p^2+m_\nu^2}/k_B T} + 1} \right) \ , \tag{3.13}$$

with $g = 2$ being the number of spin states of the neutrinos. When the temperature dropped below $T \sim 10^{10}$K ($k_B T \sim 1$ MeV[1]) the expansion rate of the universe was larger than the collision rate that kept the neutrinos in thermal equilibrium with the other particles. At that time, neutrinos decoupled from the plasma and could travel as free particles. Here we demonstrate that the distribution of the relic neutrinos gets frozen once they decoupled.

Assuming that the neutrino masses are, at most, of the eV order, we conclude that at the time they decoupled they where very relativistic ($k_B T \gg m_\nu$), so we can made the approximation $E = \sqrt{p^2 + m^2} \cong p$. Once the neutrinos decoupled, their momentum is redshifted by the expansion of the universe

$$p_\nu \sim a^{-1} \ , \tag{3.14}$$

---

[1] $k_B = 8.617 \times 10^{-5}$ eV/K

so we can write the number density of relic neutrinos at any time posterior to neutrino decoupling as

$$n_\nu(p,z) = \frac{4\pi g p^2}{(2\pi\hbar)^3}\left(\frac{1}{e^{p/k_B T_\nu(z)}+1}\right) \ , \tag{3.15}$$

where $T_\nu(z) = T_\nu^0(1+z)$. T_ν^0 is the current temperature of the cosmic neutrino background (*CNB*). It can be shown that this temperature is related with the temperature of the photons in the CMB by [104]

$$T_\nu = \left(\frac{4}{11}\right)^{1/3} T_\gamma \ . \tag{3.16}$$

Given that CMB temperature is $T_\gamma^0 = 2.725$ K, we deduce that the current temperature of the relic neutrino distribution is $T_\nu^0 = 1.95$ K $(1.68 \times 10^{-4}$ eV). The number density of relic neutrinos per specie today is given by

$$n_\nu^0 = \frac{4\pi g}{(2\pi\hbar)^3}\int_0^\infty \frac{p^2 dp}{e^{p/k_B T_\nu^0}+1} \simeq 113\frac{\nu}{\text{cm}^3} \ . \tag{3.17}$$

The neutrino energy density and pressure can be computed by:

$$\rho_\nu(z) = \int_0^\infty n_\nu\left(p,z\right) dp\sqrt{p^2+m_\nu^2} \ , \tag{3.18}$$

$$P_\nu(z) = \int_0^\infty n_\nu\left(p,z\right) dp\frac{p^2}{3\sqrt{p^2+m_\nu^2}} \ . \tag{3.19}$$

In the regime where $m_\nu \gg T_\nu$ we can approximate the factor $\sqrt{p^2+m_\nu^2}$ by m_ν and by using the expressions above we get $\rho_\nu(z) = \rho_\nu^0(1+z)^3$ and $P_\nu(z) \sim 0$. This demonstrates that when neutrinos became non-relativistics (at low redshift), they behave as matter. In contrast, in the regime where $m_\nu \ll T_\nu$, the factor $\sqrt{p^2+m_\nu^2}$ can be approximated by p. This yields to a temporal dependence $\rho_\nu(z) = \rho_\nu^0(1+z)^4$ and $P_\nu(z) = \rho_\nu(z)/3$ which reproduces the behavior of radiation.

Neutrinos became non-relativistics approximately at a redshift[2]

$$z_{\text{non-relativistics}} \sim 2000\left(\frac{m_\nu}{1\text{ eV}}\right) \ . \tag{3.20}$$

In the regime in which neutrinos are highly non-relativistic, the ratio of neutrino energy density to the critical density can be easily computed using eq. 3.18 and taking into account

---

[2] a commonly used practice is that a particle is considered relativistic if $m/T < 3$.

that $m_\nu \gg T_\nu$. This gives $\rho_\nu^0 \cong 113$ eV/cm$^3 \times \Sigma_i m_{\nu_i}$ that together with $\rho_c^0 = 1.054 \times 10^4\ h^2$ eV/cm^3 produces:

$$\Omega_\nu h^2 \simeq \frac{\Sigma_i m_{\nu_i}}{93.3\ eV} \ . \tag{3.21}$$

The mean thermal velocity of relic neutrinos, when they are non-relativistic, can be easily computed from the distribution 3.15 and is roughly given by

$$\overline{v}_\nu = 150(1+z)\left(\frac{1\ \mathrm{eV}}{m_\nu}\right)\ \mathrm{km\ s^{-1}} \ . \tag{3.22}$$

3.4 Impact on cosmology

Neutrinos play an important role in cosmology. Their large velocity dispersion make them to behave in a very different way from that of the cold dark matter. In this section we explain how the large neutrino velocities impact on the grow of CDM perturbations and therefore in the large scale structure of the universe.

Here we point out two effects that neutrinos induce in the process of structure formation if a fraction of the dark matter is made up of neutrinos. This is equivalent to keep fixed the total dark matter content, Ω_{dm}, splitting it into cold dark matter and neutrinos $\Omega_{\mathrm{dm}} = \Omega_{\mathrm{CDM}} + \Omega_\nu$.

The first induced effect is that neutrinos modify the matter-radiation equality. This time represents the epoch when the contribution of radiation to the total energy content of the universe equals the contribution from matter and is given by

$$a_{\mathrm{eq}} = \frac{\Omega_{\mathrm{r}}}{\Omega_{\mathrm{b}} + \Omega_{\mathrm{CDM}}} \tag{3.23}$$

with Ω_{r} taking contributions from both, photons and neutrinos. Since both cosmological models, with massive or massless neutrinos, make the same contribution to Ω_{r} at this epoch (at the time of matter-radiation equality, neutrinos of masses $\Sigma_i m_{\nu_i} \lesssim 1$ eV are very relativistic, so they contribute to the energy density as radiation instead of matter), the decrement in Ω_{CDM}, which is due to massive neutrinos, modify this time by a factor $(1-f_\nu)^{-1}$

$$a_{\mathrm{eq}}^{f_\nu} = a_{\mathrm{eq}}^{f_\nu=0}(1-f_\nu)^{-1} \ , \tag{3.24}$$

with f_ν defined as:

$$f_\nu = \frac{\Omega_\nu}{\Omega_{\mathrm{m}}} = \frac{\Omega_\nu}{\Omega_{\mathrm{b}} + \Omega_{\mathrm{CDM}} + \Omega_\nu} \ . \tag{3.25}$$

Given that CDM perturbations do not grow as fast in the radiation dominated era ($\delta \propto \ln(a)$) as in the matter dominated era ($\delta \propto a$), the delay in the matter-radiation equality, as compared with the massless neutrino model, induced by massive neutrinos, will produce that structures would be less evolved in the massive neutrino model than in the massless case.

The second effect arises once the CDM perturbations enter into the matter dominated era. Neutrinos will slow down the rate at which CDM perturbations grow. In order to understand in detail this effect lets write down the mass and momentum conservation laws for an ideal fluid (since we are interested in CDM perturbations, we will assume that universe is made up of a cosmological constant, CDM and massive or massless neutrinos):

$$\left(\frac{\partial \rho}{\partial t}\right)_{\mathbf{r}} + \vec{\nabla}_{\mathbf{r}} \cdot (\rho \mathbf{u}) = 0 \tag{3.26}$$

$$\left(\frac{\partial \mathbf{u}}{\partial t}\right)_{\mathbf{r}} + (\mathbf{u} \cdot \vec{\nabla}_{\mathbf{r}})\mathbf{u} = -\vec{\nabla}_{\mathbf{r}}\Phi \tag{3.27}$$

with $\rho(\mathbf{r}, t)$, $\mathbf{u}(\mathbf{r}, t)$ and $\Phi(\mathbf{r}, t)$ being the density, velocity and gravitational potential of the ideal fluid respectively (note that since we are interested in CDM perturbations we can neglect pressure gradients in the momentum conservation equation). The above equations together with the Poisson equation,

$$\nabla^2_{\mathbf{r}}\Phi = 4\pi G\rho \ , \tag{3.28}$$

specify completely the evolution of the ideal fluid once the initial conditions are given. The linearized equation governing the evolution of a CDM density perturbation can be found by using the above equations (see for example [65]):

$$\ddot{\delta}_{\rm CDM} + 2\frac{\dot{a}}{a}\dot{\delta}_{\rm CDM} = 4\pi G\overline{\rho}_{\rm CDM}\delta_{\rm CDM} \ , \tag{3.29}$$

where $\overline{\rho}_{\rm CDM}$ is the background CDM density, $\delta_{\rm CDM}$ is the CDM density perturbation $\rho_{\rm CDM}(\mathbf{x}, t) = \overline{\rho}_{\rm CDM}(t)[1 + \delta_{\rm CDM}(\mathbf{x}, t)]$ and $\mathbf{x} = \mathbf{r}/a$ is the comoving coordinate. Equation 3.29 has as general solution:

$$\delta_{\rm CDM}(\mathbf{x}, t) = A(\mathbf{x})D_1(t) + B(\mathbf{x})D_2(t) \ , \tag{3.30}$$

with D_1 and D_2 being the growing and decaying modes respectively. For a flat cosmology, well inside the matter dominated era

$$\left(\frac{\dot{a}}{a}\right)^2 \cong \frac{8\pi G}{3}\overline{\rho}_{\rm CDM} \ , \tag{3.31}$$

$$\frac{\ddot{a}}{a} \cong -\frac{4\pi G}{3}\overline{\rho}_{\mathrm{CDM}} \tag{3.32}$$

the growing mode is given by $D_1(a) \propto a$. The general growing mode, for a flat universe with both CDM and a cosmological constant:

$$\left(\frac{\dot{a}}{a}\right)^2 \cong \frac{8\pi G}{3}(\overline{\rho}_{\mathrm{CDM}} + \overline{\rho}_{\Lambda}) \tag{3.33}$$

$$\frac{\ddot{a}}{a} \cong -\frac{4\pi G}{3}(\overline{\rho}_{\mathrm{CDM}} - 2\overline{\rho}_{\Lambda}) \ , \tag{3.34}$$

is given by the well known expression:

$$\delta \propto H(z)\int_z^{\infty} \frac{dz'(1+z')}{H^3(z')} \ . \tag{3.35}$$

Note that for $z \gg 1$ ($H(z) = H_0\sqrt{\Omega_{\mathrm{CDM}}(1+z)^3 + \Omega_\Lambda} \simeq H_0\sqrt{\Omega_{\mathrm{CDM}}}(1+z)^{3/2}$) we recover the growth factor of the Einstein-De Sitter universe ($\delta \propto (1+z)^{-1}$). Equation 3.29 is also valid to compute the linear growth of cold dark matter perturbations in a universe containing massive neutrinos. The difference with the equation governing the evolution of CDM perturbations in a neutrinoless universe is that neutrinos affect the Hubble parameter:

$$H^2 = \frac{8\pi G}{3}(\overline{\rho}_{\mathrm{CDM}} + \overline{\rho}_\nu + \overline{\rho}_{\Lambda}) \tag{3.36}$$

Lets assume that neutrinos are non-relativistic at some epoch of the matter dominated era. Therefore their density will scale as $\overline{\rho}_\nu(a) \propto a^{-3}$ and the ratio

$$f_\nu = \frac{\overline{\rho}_\nu}{\overline{\rho}_{\mathrm{CDM}} + \overline{\rho}_\nu} \tag{3.37}$$

remain constant and equals to $\Omega_\nu/(\Omega_\nu + \Omega_{\mathrm{CDM}})$. In this epoch of the matter dominated era when neutrinos are non-relativistic we can write:

$$\left(\frac{\dot{a}}{a}\right)^2 \cong \frac{8\pi G}{3}(\overline{\rho}_{CDM} + \overline{\rho}_\nu) = \frac{8\pi G}{3}\overline{\rho}_{CDM}\frac{1}{1-f_\nu} \tag{3.38}$$

$$\frac{\ddot{a}}{a} \cong -\frac{4\pi G}{3}(\overline{\rho}_{CDM} + \overline{\rho}_\nu) = -\frac{4\pi G}{3}\overline{\rho}_{CDM}\frac{1}{1-f_\nu} \ . \tag{3.39}$$

Using the above equations we find that the solution to eq. 3.29 can be written in the form $\delta(\mathbf{x}, a) = A(\mathbf{x})a^{\alpha_+} + B(\mathbf{x})a^{\alpha_-}$, with

$$\alpha_\pm = \frac{-1 \pm \sqrt{1 + 24(1 - f_\nu)}}{4} \ . \tag{3.40}$$

Therefore, in the matter dominated era, the growth of CDM perturbations is suppressed by neutrinos

$$D_1(a) \simeq a^{1-(3/5)f_\nu} \ . \tag{3.41}$$

The general solution to equation 3.29 in presence of a cosmological constant can be found in [41].

By solving eq. 3.29 for 4 different cosmological models we show in the Fig. 3.3 the different growth of a CDM perturbation. The amplitude of the CDM perturbation is fixed at $z = 100$ for all the models. The growth in the Einstein-De-Sitter cosmology ($\Omega_{\rm CDM} = 1$) is given by $\delta \propto a$, while this trend is recovered in the matter dominated era for the neutrinoless cosmology with a cosmological constant. The model with massive neutrinos and no cosmological constant reproduced the law $\delta \propto a^{1-(3/5)f_\nu}$ and this function is recovered in the matter dominated era of the model with both massive neutrinos and a cosmological constant. As can be seen in the figure, neutrinos delay the process of structure formation by slowing down the rate at which CDM grow.

One of the most useful concepts in cosmology is the so-called *matter power spectrum*. It is defined as the two point correlation function of non-relativistic matter fluctuations in Fourier space

$$P(k, z) =< |\delta_{\rm m}(k, z)|^2 > \ , \tag{3.42}$$

being $\delta_m = \delta\rho_m/\overline{\rho}_m$ the matter density contrast. It is possible to solve numerically the equations governing the growth of perturbations in the linear regime and therefore, compute the evolution of the *linear* power spectrum[3].

In Fig. 3.4 we plot the linear power spectrum, computed with CAMB, for a massless neutrinos universe with cosmological parameters: $\Omega_{\rm CDM} = 0.25$, $\Omega_b = 0.05$, $\Omega_\Lambda = 0.7$, $n_{\rm s} = 0.95$, $h = 0.7$ and $\sigma_8 = 0.8$. We also plot the linear power spectrum of different cosmological models with 3 degenerate neutrinos. Those models satisfy $\Omega_\nu + \Omega_{\rm CDM} = 0.25$.

As can be see from Fig. 3.4, neutrinos suppress the power on small scales. This suppression comes from the two effects discussed above. The first one is that neutrinos modify the matter radiation equality delaying this epoch by a factor $(1 - f_\nu)^{-1}$. Given that perturbations do not grow as fast in the radiation dominated era as in the matter dominated era, we expect that structures would be less evolved in the case with massive neutrinos, i.e. the power spectrum on small scales should be suppressed. The second one, and the most important, is because once CDM perturbations enter into the matter dominated era, neutrinos

---

[3] One of the most popular codes to do this is CAMB (`http://camb.info/`)

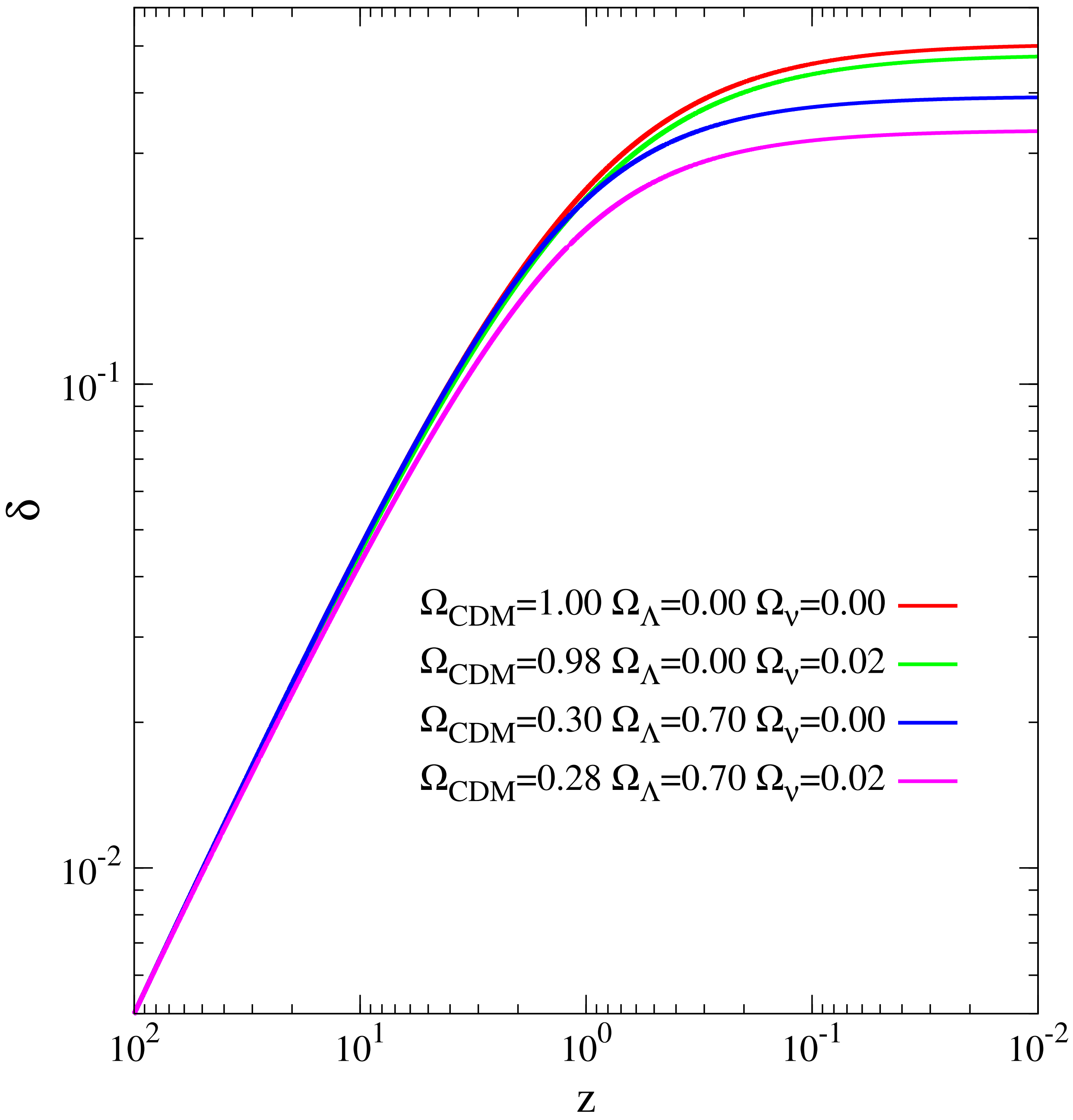

Figure 3.3: The linear growth of a CDM perturbation as a function of cosmology. We plot the time evolution of a CDM perturbation as a function of Ω_{CDM}, Ω_Λ and Ω_ν for perturbations which have the same amplitude at $z = 100$. In the matter dominated era ($z < 2$ for models with a cosmological constant) the behavior of the growth is perfectly described by $\delta \propto a$ for the neutrinoless models and $\delta \propto a^{1-(3/5)f_\nu}$ for the models with massive neutrinos.

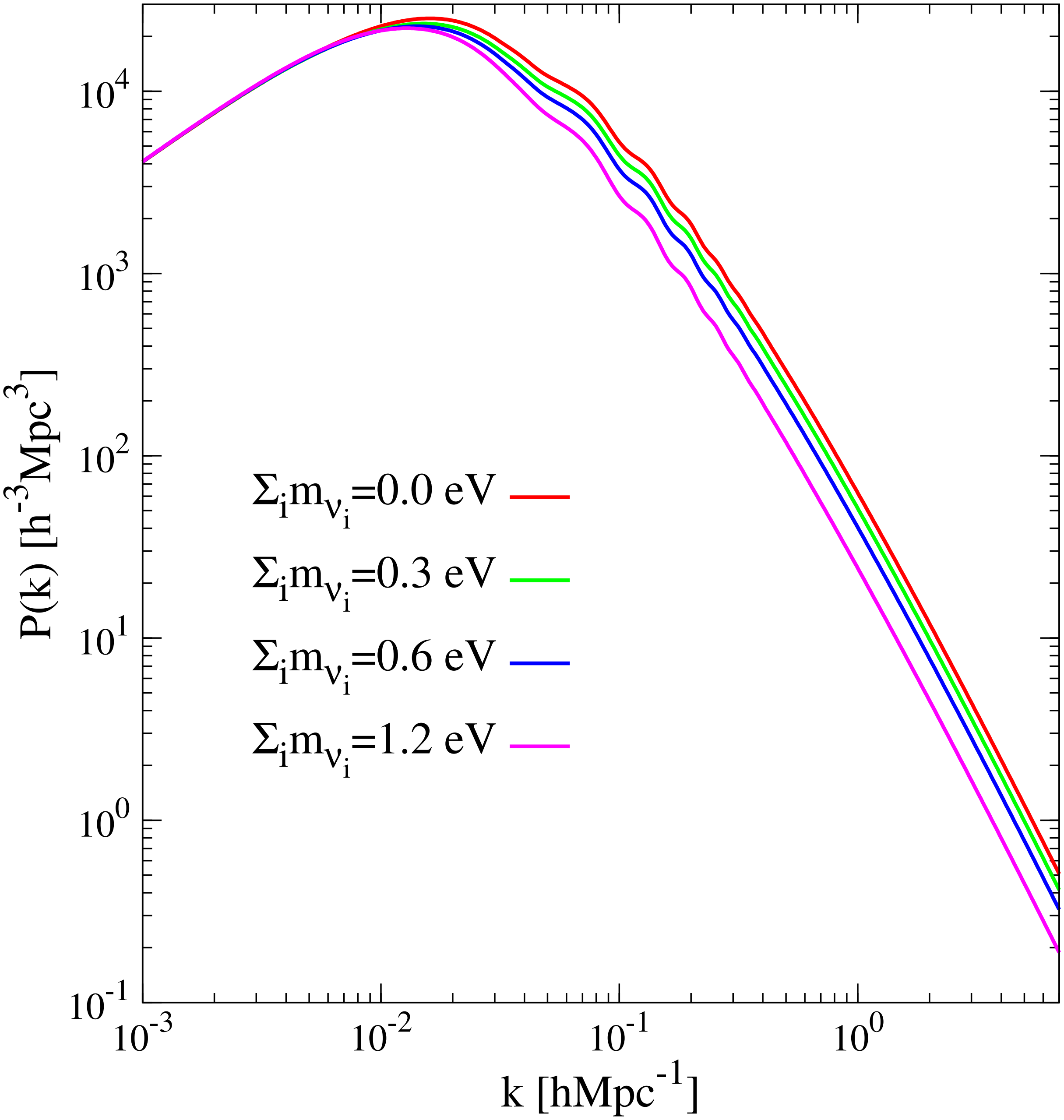

Figure 3.4: Linear power spectrum for 3 cosmological models with massive neutrinos and one with massless neutrinos. The massless model has cosmological parameters: $\Omega_{\rm CDM} = 0.25$, $\Omega_{\rm b} = 0.05$, $\Omega_\Lambda = 0.7$, $n_{\rm s} = 0.95$, $h = 0.7$ and $\sigma_8 = 0.8$. The models with neutrinos satisfy $\Omega_\nu + \Omega_{\rm CDM} = 0.25$. Neutrinos large free-streaming produce a decrease in the amplitude of the power spectrum on small scales as a result of the delay they induce in the process of structure formation.

slow down the rate at which perturbations grow. In the massless neutrino cosmology and in the matter dominated era, CDM perturbations grow as $\delta \propto a$ while massive neutrinos cause that perturbations on this regime grow at a slower rate $\delta \propto a^{1-(3/5)f_\nu}$.

These two effects produce a suppression in the matter power spectrum on small scales as can be seen from Fig. 3.4. On very small scales, the suppression caused by neutrinos can be estimated to be (see [51])

$$\frac{P(k)^{f_\nu}}{P(k)^{f_\nu=0}} = (1-f_\nu)^3[1.9\times 10^5 g(a_0)\Omega_m h^2 f_\nu/N_\nu]^{-(6/5)f_\nu} \ , \tag{3.43}$$

with $g(a_0)$ a function, evaluated today, that account for the change in the grow factor due to the presence of a cosmological constant. For values of $f_\nu < 0.07$ the above expression can be approximated by the well known formula:

$$\frac{P(k)^{f_\nu} - P(k)^{f_\nu=0}}{P(k)^{f_\nu=0}} = \frac{\triangle P}{P} \cong -8f_\nu \ . \tag{3.44}$$

In the Fig. 3.5 we plot the ratio $P(k)^{f_\nu}/P(k)^{f_\nu=0}$ for different neutrino masses. For values of f_ν smaller than 0.07, the suppression of the linear power spectrum on small scales is very well approximated by the expression $\triangle P/P \cong -8f_\nu$.

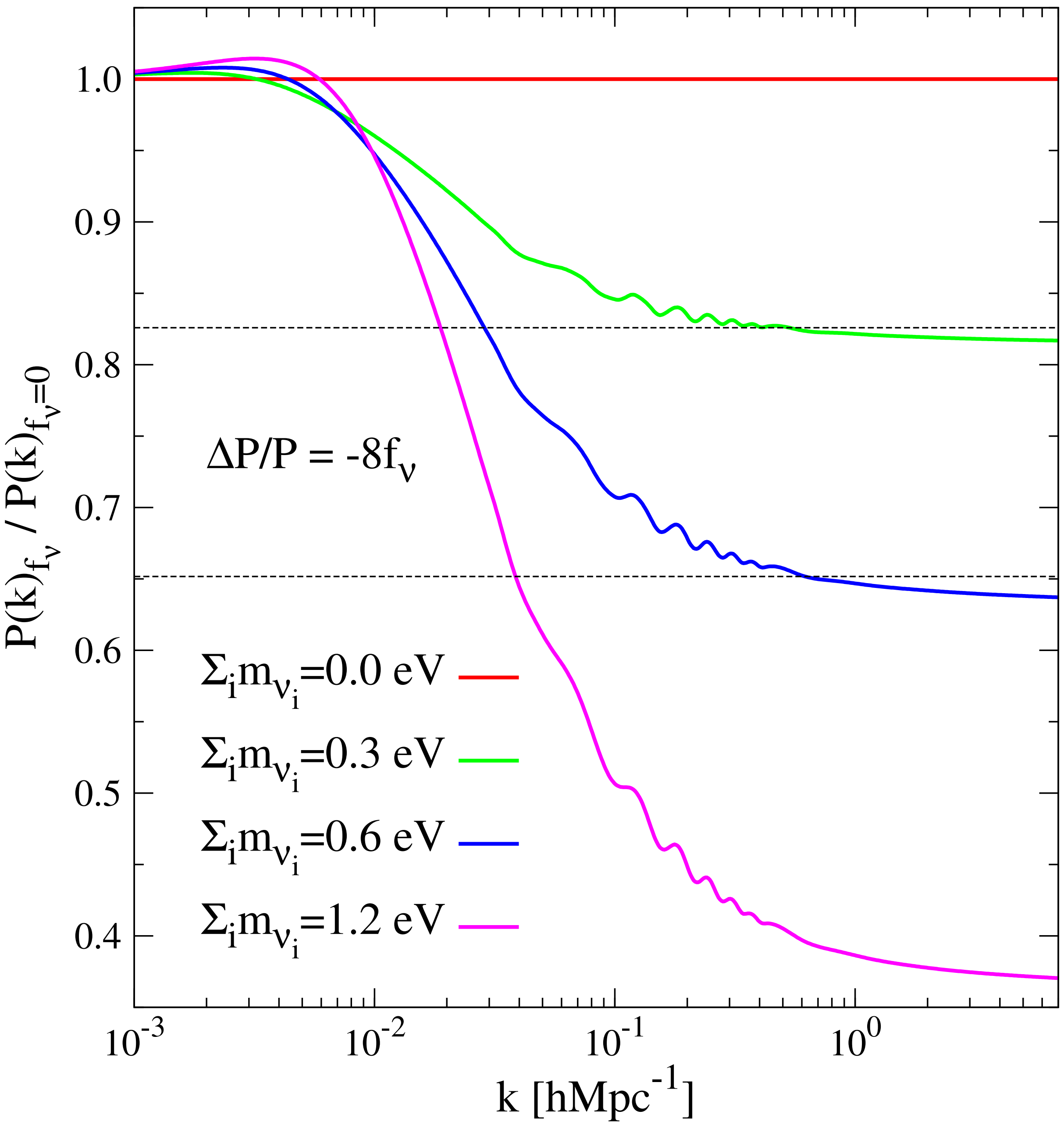

Figure 3.5: Ratio between the linear power spectrum with massive neutrinos to this with massless neutrinos. The massless neutrino model has cosmological parameters: $\Omega_{\rm CDM} = 0.25$, $\Omega_{\rm b} = 0.05$, $\Omega_\Lambda = 0.7$, $n_{\rm s} = 0.95$, $h = 0.7$ and $\sigma_8 = 0.8$. The models with massive neutrinos satisfy $\Omega_\nu + \Omega_{\rm CDM} = 0.25$. For values of $f_\nu = \Omega_\nu/\Omega_{\rm m}$ less than ~ 0.07, the maximum neutrino suppression is roughly given by $\triangle P/P \sim -8f_\nu$.

Part II

Scientific Research

Chapter 4

Cores and cusps in warm dark matter halos

In this chapter we answer the question whether warm dark matter can produce cores in the dark matter density profile large enough to reproduce the observed ones in the LSB galaxies. This chapter is a copy of the paper:

Cores and cusps in warm dark matter halos, Francisco Villaescusa-Navarro & Neal Dalal, 2011, JCAP, 03, 24

4.1 Introduction

The spectacularly successful cold dark matter (CDM) model idealizes the thermal motions of dark matter particles as negligible on all scales at high redshift. In this model, perturbation modes on all scales are gravitationally unstable, leading to hierarchical structure formation in which nonlinear structures such as halos assemble through numerous mergers. Numerical simulations of structure formation within CDM models indicate that halos are predicted to have steep central density profiles, with logarithmic slopes $d\log\rho/d\log r \sim -1$ on the smallest resolved scales (see [67] for a recent example).

In many DM models, however, the DM temperature is nonzero, which can affect the properties of DM halos in multiple ways. For example, a finite DM temperature suppresses the abundance of low-mass halos. This occurs because, following freezeout of dark matter interactions, DM particles freely stream over some distance determined by their thermal velocities, and density fluctuations on scales below this free-streaming scale $r_{\rm fs}$ are highly suppressed. Roughly speaking, the smallest halos that arise are expected to have masses of order $M_{\rm fs} = (4\pi/3)\bar{\rho}_m r_{\rm fs}^3$, although N-body simulations have not definitively ruled out the formation of at least some halos below $M_{\rm fs}$ through non-hierarchical processes like fragmentation [100].

Besides this suppression of the abundance of halos, a nonzero DM temperature also can affect the central density profiles of the halos that do form. One elegant way to see this is to note that the DM phase space density is finite if the DM temperature is finite, and since DM is taken to be collisionless, then Liouville's theorem guarantees that the phase space density cannot increase. Hence, the phase space density is bounded within DM halos [91], which implies that the central slope of the DM density profile must vanish (e.g. [92]). In other words, halos are expected to have central cores if the DM is not cold. Note that this effect is caused by the finite DM temperature at the time of formation of the halo, and is not due to the truncation of the small-scale linear power spectrum [101].

Therefore, increasing the DM temperature has the effect of suppressing the number of low-mass halos, and of producing central cores in DM halos. Observationally, there may be evidence for both of these effects. The observed number of Local Group satellite galaxies falls well below the thousands of DM subhalos found in CDM simulations of halos like our Galaxy's (see [49] for a recent review). In addition, the 21 cm rotation curves of certain galaxies, in particular low surface brightness (LSB) galaxies, appear better fit by cored DM profiles than cuspy DM profiles (see [50] for a recent discussion). For these reasons, there has been considerable interest in the literature in investigating structure formation in models where DM is not perfectly cold. In so-called Warm Dark Matter (WDM) models, the DM temperature is chosen to make the free-streaming scale correspond to subgalactic scales, $r_{\rm fs} \sim 0.1h^{-1}$Mpc [12].

WDM models have become increasingly disfavored in recent years, in large part because of constraints on the matter power spectrum derived from the Lyman-α forest flux power spectrum [78]. The observational support for WDM models from dwarfs and LSB galaxies has also eroded, as faint Local Group satellites have been discovered in increasing numbers (e.g. [6] [90] [49]) thanks to the Sloan Digital Sky Survey. Very recently, [50] have argued that the large cores apparently observed in certain LSB galaxies cannot all be due to WDM, since the implied central phase space densities in these systems are not universal, but instead show large variations from object to object. This suggests an astrophysical origin for claimed detections of central cores, and mechanisms to produce such cores have been proposed (e.g. [35]).

In this paper, we present yet another argument against WDM as the origin of large cores in halo density profiles. As discussed by [50], the inferred core radii in several LSB galaxies are large fractions of the halo virial radii, $r_{\rm core} \sim 5\%\, r_{200}$. As mentioned above, such large cores do not arise in CDM models, and so we might naturally consider producing large cores by raising the DM temperature. Making the DM warm, however, has the side effect of wiping out small halos, and so it is not obvious that raising the DM temperature can generate halos with large $r_{\rm core}/r_{200}$.

We can, however, use a simple argument to make an order-of-magnitude estimate of this ratio. Consider a WDM particle of mass m and typical momentum p. Following freezeout, its momentum redshifts as $p \propto a^{-1}$, so let us write $p = mv_0/a$, where v_0 is the velocity today at $z = 0$ (since WDM must be nonrelativistic today, $v_0 \ll 1$). The particle's velocity is then $v(a) = v_0/\sqrt{v_0^2 + a^2}$ (using units where $c = 1$). Neglecting accelerations caused by gravitational potential fluctuations, the particle freely streams a comoving distance

$$r_{\rm fs} = \int \frac{v\,dt}{a} \sim \frac{v_0}{\Omega_r^{1/2} H_0} \log\left(\frac{a_{\rm eq}}{v_0}\right), \tag{4.1}$$

where we assume $v_0 \ll a_{\rm eq} = \Omega_r/\Omega_m$. This distance encloses mass $M_{\rm fs} = (4\pi/3)\bar{\rho}_m r_{\rm fs}^3$, and as noted above, the smallest halos that form will have masses of order $M_{\rm fs}$. The virial velocities of these halos at their formation epoch a_c are

$$v_{200} = \left(\frac{GM_{\rm fs}}{r_{200}}\right)^{1/2} = \left(\frac{\Omega_m \Delta_{200}^{1/3}}{2a_c}\right)^{1/2} H_0\, r_{\rm fs}, \tag{4.2}$$

where $\Delta_{200} \approx 200$ is the virial overdensity. Now, because the thermal velocity $v_{\rm th} \approx v_0/a_c$ at expansion factor a_c is nonzero, infalling particles will not fall directly towards the halo center, but instead have a nonzero impact parameter, and the typical impact parameter determines the core size. Naively, we might expect that at formation ($a = a_c$),

$$\frac{r_{\rm core}}{r_{200}} \sim \frac{v_{\rm th}}{v_{200}} \sim \left(\frac{\Omega_r}{\Omega_m}\frac{2}{\Delta_{200}^{1/3} a_c}\right)^{1/2} / \log\left(\frac{a_{\rm eq}}{v_0}\right). \tag{4.3}$$

Following formation, any subsequent growth in halo mass can only decrease the core radius, while the virial radius can only increase. Indeed, even if the mass distribution around the halo is static, with no accretion following formation, the virial radius will still grow in time proportionally to the expansion factor a, because the expansion of the universe dilutes the background mean matter density. This is the reason why halo concentrations correlate with halo formation times in CDM cosmologies (e.g. [102] [106][107]). Therefore, following the formation epoch a_c, the ratio $r_{\rm core}/r_{\rm vir}$ must diminish in time at least as fast as a_c/a; any mass accretion will only decrease this ratio even faster. Assuming no growth, then at the present time ($a = 1$)

$$\frac{r_{\rm core}}{r_{200}} \sim \left(\frac{\Omega_r}{\Omega_m}\right)^{1/2} \left(\frac{2a_c}{\Delta_{200}^{1/3}}\right)^{1/2} / \log\left(\frac{a_{\rm eq}}{v_0}\right). \tag{4.4}$$

This ratio is maximized by delaying halo formation as late as possible. For typical parameters, and setting $a_c = 1$, this gives $r_{\rm core} \approx 10^{-3} r_{200}$ observed today.

From this simple order-of-magnitude estimate, it appears unlikely that WDM models can produce sufficiently large core radii to explain LSB galaxies. This argument is only approximate, however. To make further progress, we have performed calculations of halo formation in WDM models. Our results indicate that WDM halo cores are significantly smaller than the above estimate, which precludes WDM as an explanation for the large cores that are claimed to exist in certain LSB galaxies.

4.2 Numerical Method

In this section we describe our numerical method to solve for the self-consistent halo density profile following collapse. We eschew conventional N-body simulations, since for feasible simulation parameters the core radii will typically be unresolved or (at best) marginally resolved [21]. Since we are interested in studying the behavior on scales smaller than the typical resolution limits of conventional N-body simulations, we have instead employed an alternative approach similar to that used by [52].

We calculate the collapse of isolated peaks in an expanding universe. To isolate the effects of the nonzero WDM temperature during halo collapse, we focus on the case of spherical collapse. This problem has been investigated previously in the literature, and it is straightforward to show that cold, spherical collapse gives halos with central density profiles behaving as $\rho \propto r^{-2}$, or steeper [28] [9] [52]. Because cold spherical collapse is well-understood, any departures from r^{-2} profiles are clearly due to the effects of warm collapse. By Newton's theorem, our calculations neglect the effects of the local environment of peaks, which cause peaks to collapse nonspherically. We know from previous cosmological WDM simulations, however, that accounting for the effects of local environment does not lead to large cores in WDM halos [101] [21].

For a given potential $\Phi(r,t)$, assumed to be spherically symmetric, we integrate the equations of motion to solve for the orbit $R(t)$ for each particle. Given the orbit $R(t)$, we compute the mass profile deposited by each particle. We compute orbits for many particles, and sum over all their deposited mass profiles to obtain the total mass profile $M_{\rm total}(r,t)$, and the total density $\rho = (dM_{\rm total}/dr)/(4\pi r^2)$. Then, we repeat this procedure, using the newly obtained mass profile, and iterate to convergence.

We initialize this procedure using linear perturbation theory. We start with a linear density profile $\delta(r_{\rm L})$ describing the initial peak at the starting epoch $a_{\rm init} = (1+z_{\rm init})^{-1}$. Here, $r_{\rm L}$ is a comoving Lagrangian radius, to be distinguished from the proper Eulerian radius r at subsequent times. We choose the initial peak profile to be proportional to the (linear theory) matter correlation function, $\delta(r_{\rm L}) \propto \xi(r_{\rm L})$. This corresponds to the average profile of high peaks in the $\nu \to \infty$ limit [4], and so this profile should be typical of the first halos to form in WDM cosmologies. The matter correlation function depends on the WDM transfer function, which [12] found to be well described by the parametrization

$$T_{\rm WDM}(k) = [1 + (\alpha k)^{2\nu}]^{-5/\nu}, \tag{4.5}$$

where $\nu \approx 1.2$ and α is a characteristic length scale. We parametrize WDM models by their free-streaming scale $r_{\rm fs}$, or equivalently the enclosed mass $M_{\rm fs}$, so we require a translation between $r_{\rm fs}$ and α. We determine the equivalent free-streaming length for a given α by matching the [12] transfer function to top-hat smoothing, which is given by

$$W_{\rm TH}(k) = \frac{3}{(kR)^3}[\sin(kR) - kR\cos(kR)] \tag{4.6}$$

for smoothing scale R, which we take to be equal to r_{fs}. We have found that $\alpha \approx 5r_{\mathrm{fs}}$ provides a reasonable match to the two functions.

Given a desired free-streaming mass M_{fs} and halo formation redshift z_{form}, we set the initial peak profile shape $\delta(r = a_{\mathrm{init}}\, r_{\mathrm{L}})$ to be proportional to the correlation function (using the appropriate r_{fs}), and normalize the peak height at the starting redshift so that the average interior overdensity $\bar{\delta} \equiv 3r^{-3}\int_0^r r^2\delta\, dr$, linearly evolved to redshift z_{form} and evaluated at the free-streaming scale is $\bar{\delta}(r_{\mathrm{L}} = r_{\mathrm{fs}}, z = z_{\mathrm{form}}) = \delta_c = 1.686$, in accordance with the spherical collapse model [36]. We assume that this linear profile evolves at early times according to linear perturbation theory:

$$\delta(r = a\, r_{\mathrm{L}}, a) = D(a)\delta(r_{\mathrm{L}}) \tag{4.7}$$

where $D(a)$ is the linear growth factor, which for ΛCDM universes with no pressure perturbations may be expressed as

$$D(a) \propto H(a)\int_0^a \frac{da}{(aH)^3}, \tag{4.8}$$

normalized so that $D(a = 1) = 1$ [70]. Note that this procedure is not entirely self-consistent, since our use of CDM growth factors neglects the scale-dependence in WDM growth factors caused by residual free-streaming at late times. Our neglect of this residual free streaming when normalizing the initial peak height means that our peaks do not actually reach $\delta = \delta_c$ at redshift z_{form}, leading to slight errors in the formation epoch. This does not appear to affect our results significantly.

This procedure specifies the initial overdensity perturbation at the starting redshift of the simulation. We also require the initial velocities for all the particles. These velocities have three contributions: the Hubble velocity, the bulk peculiar velocity, and a random thermal velocity. The Hubble term is of course just given by $\boldsymbol{v}_H = H\,\boldsymbol{r}$. The bulk peculiar velocity may be computed from the density profile, using the linearized continuity equation

$$\dot{\delta} + \boldsymbol{\nabla}\cdot\boldsymbol{v} = 0, \tag{4.9}$$

along with the assumption of potential flow at early times (i.e. $\nabla \times \boldsymbol{v} = 0$). This gives

$$v_r(r, a) \simeq -\frac{1}{3} r\bar{\delta}(r, a)H(a), \tag{4.10}$$

where again $\bar{\delta} \equiv 3r^{-3}\int_0^r r^2\delta\, dr$. In addition to this bulk peculiar velocity, for each particle we add a thermal velocity, drawn from a Fermi-Dirac distribution function for WDM temperature T:

$$f(p, T)d^3p = \frac{1}{N_0(T)}\frac{p^2dp}{e^{p/k_BT} + 1} \tag{4.11}$$

where the normalization is given by

$$N_0(T) = \int_0^\infty \frac{p^2dp}{e^{p/T} + 1}. \tag{4.12}$$

We typically begin at redshift $z = 100$. We sample 6000 initial radii spaced uniformly in volume, up to a maximum radius chosen to enclose the virialized region at $z = 0$. For each radius, we sample the momentum distribution with 500 points and the angular distribution with 200 points, weighting the particles according to the fraction of initial volume, solid angle, and momentum distribution that they represent.

Given the initial conditions for each particle, we then integrate forward the equations of motion using a fourth order, variable timestep Runge-Kutta integrator. The equations of motion are given by the usual Newtonian dynamics:

$$\frac{d^2R}{dt^2} - \frac{L^2}{R^3} = -\nabla\Phi, \tag{4.13}$$

where the angular momentum $\boldsymbol{L} = \boldsymbol{R} \times \boldsymbol{v}$ is conserved because of the assumed spherical symmetry.

Given an orbit $R(t)$, the enclosed mass profile deposited by each particle is

$$M(r,t) = m_p\Theta[r - R(t)], \tag{4.14}$$

where m_p is the mass represented by the particle, and $\Theta(x)$ is the step function. Summing over all particles gives the total mass profile $M_{\rm total}(r,t)$, and the density $\rho(r,t)$ and potential $\Phi(r,t)$ follow easily. Having computed the mass profile $M(r,t)$ for a given iteration, we then use that mass profile in the equations of motion for the subsequent iteration. In practice, we bin the mass profile using a grid with 350 bins spaced uniformly in expansion factor a and 500 logarithmically spaced bins per decade in radius, and then linearly interpolate from this grid to estimate the mass M at arbitrary times and radii as needed for the orbit integrations.

To expedite this calculation, we have made use of a simplifying approximation. For particles deep within the halo, whose orbital times are small compared to the Hubble time, we stop the orbital integration after the fractional change in the product $R_{\rm apo} \times M(R_{\rm apo})$ over one orbit is less than 10^{-3}. Thereafter, we assume that the orbit evolves adiabatically. Specifically, we assume that the radial action $J_r = \oint v_r dR \propto [R_{\rm apo}M(R_{\rm apo})]^{1/2}$ is an adiabatic invariant. Given the time evolution of the mass profile $M(r,t)$, we then easily determine the time evolution of the orbital apoapse $R_{\rm apo}$. As Fig. 4.1 illustrates, adiabaticity is an excellent approximation for these orbits. Similarly, we assume that the ratio of periapse to apoapse, $R_{\rm peri}/R_{\rm apo}$, is also conserved because of conservation of angular momentum. Given $R_{\rm peri}$ and $R_{\rm apo}$, we then assume that the mass profile deposited by this particle is

$$M(r,t) = m_p \times \begin{cases} 1, & \text{if } r > R_{\rm apo} \\ \frac{r - R_{\rm peri}}{R_{\rm apo} - R_{\rm peri}}, & \text{if } R_{\rm peri} < r < R_{\rm apo} \\ 0, & \text{if } r < R_{\rm peri} \end{cases} \tag{4.15}$$

which is a good approximation to Eqn. (4.14), except for radii very near $R_{\rm peri}$ or $R_{\rm apo}$.

This iterative procedure rapidly converges to a self-consistent collapse solution; Figure 4.2 illustrates one typical example. As the figure shows, the interior density profile quickly

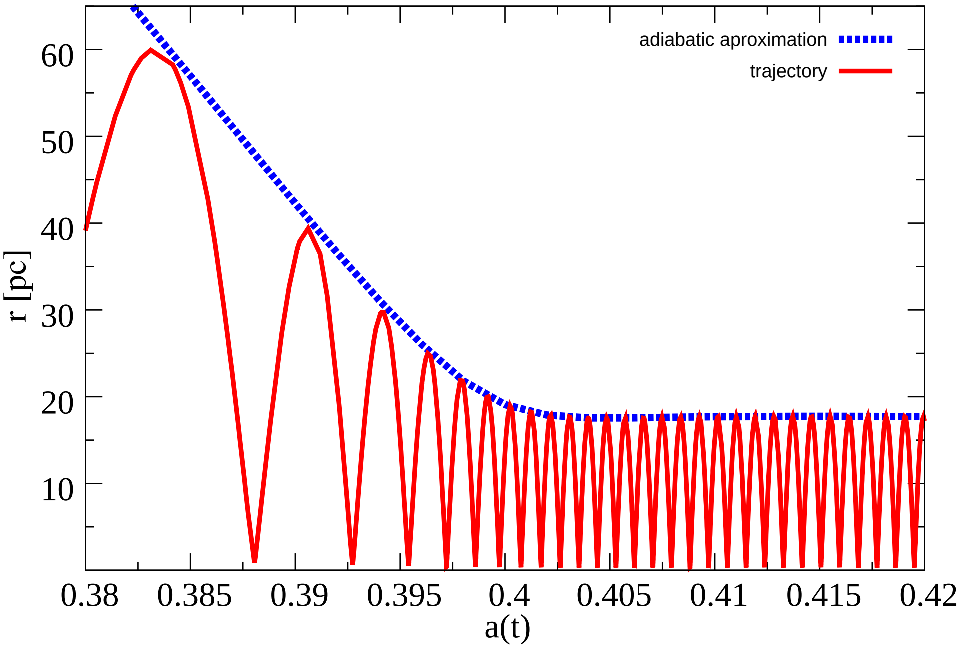

Figure 4.1: Adiabatic orbital evolution. The solid red curve shows an example orbit $r(t)$ for a particle from one of our collapse calculations. For comparison, the dashed blue curve shows the expected behavior for the apoapse under the assumption that the orbit responds adiabatically to the deepening gravitational potential.

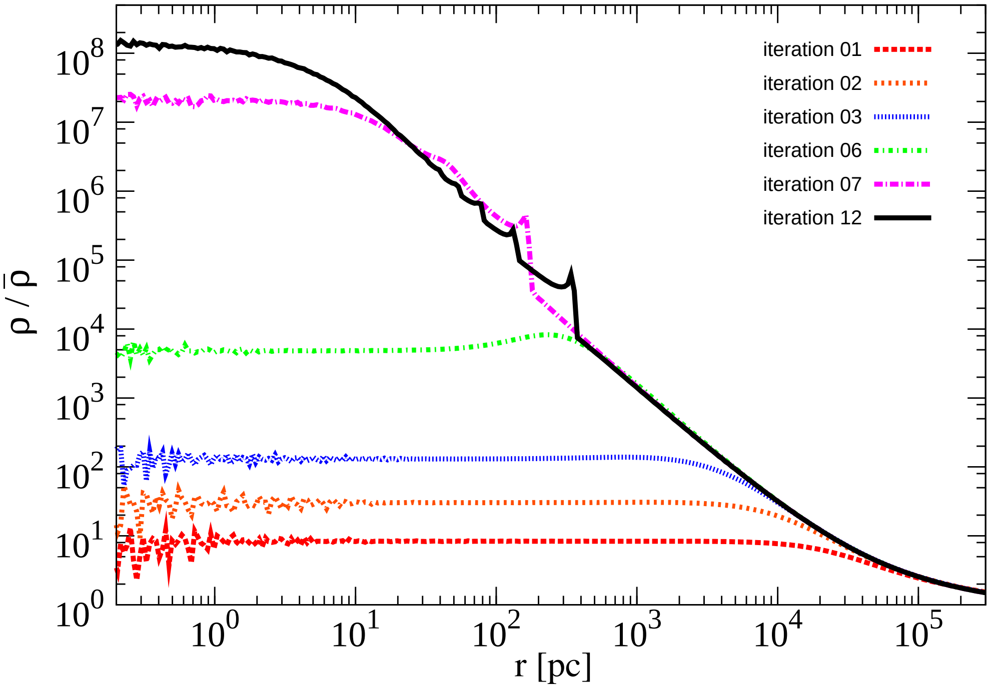

Figure 4.2: Convergence of the density profile. The halo density profile at $z = 2.7$ after iterations 1,2,3,6 and 7 are shown in the colored curves, while the black curve shows the converged profile (12 iterations).

settles into roughly r^{-2} behavior, as expected, although there are features at both large radii and small radii. The spikes at large radii are caustics, a well-known feature of cold spherical collapse [28][98]. At small radii, discreteness effects of the finite number of particles leads to noise in the determined profile. This noise in the mass profile enters the equations of motion for particles, which affects particle orbits and leads to rapidly developing instabilities in the phase-space structure [39][5][40]. These instabilities significantly distort the shape of the radial caustics at times following collapse. We have checked that if we suppress these instabilities by artificially smoothing the potential, the caustics match the expected form. Because these instabilities are physical, rather than numerical in origin, we have opted not to suppress them. Accordingly, our density profiles at late times, long after collapse, do not show the expected prominent caustics.

4.3 Results

In this section we present results of our calculations. In the first subsection, we illustrate the behavior found in one typical simulation, and in the following subsection we describe how the behavior changes as we vary several physical parameters.

4.3.1 Anatomy of a WDM halo

In this subsection, we describe the detailed results of one of our simulations. The behavior found for this halo is representative of our simulations. For concreteness, we use a WDM temperature $T_0/m = 1.3 \cdot 10^{-8}$ in units where $c = 1$, which gives a free-streaming scale $r_{\rm fs} \sim 100\, h^{-1}$ kpc, and normalize the initial peak amplitude so that halo formation occurs near redshift $z = 3$. Figures 4.3 and 4.4 show the results. Figure 4.3 plots the density profile $\rho(r)$, the 3-D velocity dispersion $\sigma(r)$, and the pseudo-phase-space density ρ/σ^3, as a function of time, while Fig. 4.4 illustrates a snapshot in time of the radial dynamics. At early times, prior to collapse, the density evolves perturbatively, so that the $\rho(r)$ profile is similar to the original linear density perturbation $\delta(r)$, simply growing in amplitude. The phase-space density remains very homogeneous before collapse. Near the time of collapse, there is smooth infall towards the halo, and both the density and velocity dispersion rise in concert to keep ρ/σ^3 nearly constant. Orbits do cross in the infall region, however, since particles with different thermal velocities fall into the collapsing halo at different rates.

The initial collapse of the halo produces a roughly r^{-2} density profile, due to our assumption of spherical symmetry. This breaks to a shallower $\rho \sim$ const behavior at the core radius $r_{\rm core}$, where the infalling particles reach periapse. Following periapse, the particles splash back outwards with positive radial velocity. The splash-back surface defines the outermost caustic, where both the density and velocity dispersion jump precipitously. The density jumps at the caustic due to a pile-up of particles with similar apoapses. The velocity dispersion jumps because outside the caustic, particles are all falling inwards, whereas inside the caustic there is both outwards and inwards motion. Inside the caustic, the velocity dispersion remains roughly isothermal, at a value near the halo's virial velocity.

Because $\rho \sim r^{-2}$ and σ is nearly constant with radius, the pseudo-phase space density shows a nearly power-law behavior over much of the virialized region. Outside the outermost caustic, ρ/σ^3 remains nearly identical to the phase space density of the unperturbed material. At the caustic, ρ/σ^3 falls steeply, due to the sudden increase in velocity dispersion. Towards smaller radii, ρ/σ^3 rises smoothly, close to r^{-2}. It is important to stress, however, that ρ/σ^3 is not a good proxy for the actual phase-space density over much of the halo's interior. The velocity dispersion tensor is highly anisotropic, in the sense that radial velocities are much larger than tangential velocities, as can be seen from the predominantly radial orbits shown in Figures 4.1 and 4.4. For this reason, $\sigma \approx \sigma_r$, and so $\sigma^3 \approx \sigma_r^3 \gg \sigma_r \sigma_\theta \sigma_\phi$. Only near the core radius does the velocity dispersion become close to isotropic.

Many of these features are similar to what is found in cold spherical collapse [28][9]. The most obvious difference between warm and cold collapse is the presence of a core radius, caused by the orbits' inability to reach $r = 0$ due to their nonzero angular momenta. We estimate the core radius by fitting the density profile to the functional form

$$\rho = \frac{\rho_c}{\left[1 + \left(\frac{r}{r_{\rm core}}\right)^{\alpha}\right]^{2/\alpha}}. \tag{4.16}$$

The parameter α controls how sharply the profile breaks from r^{-2} behavior to constant

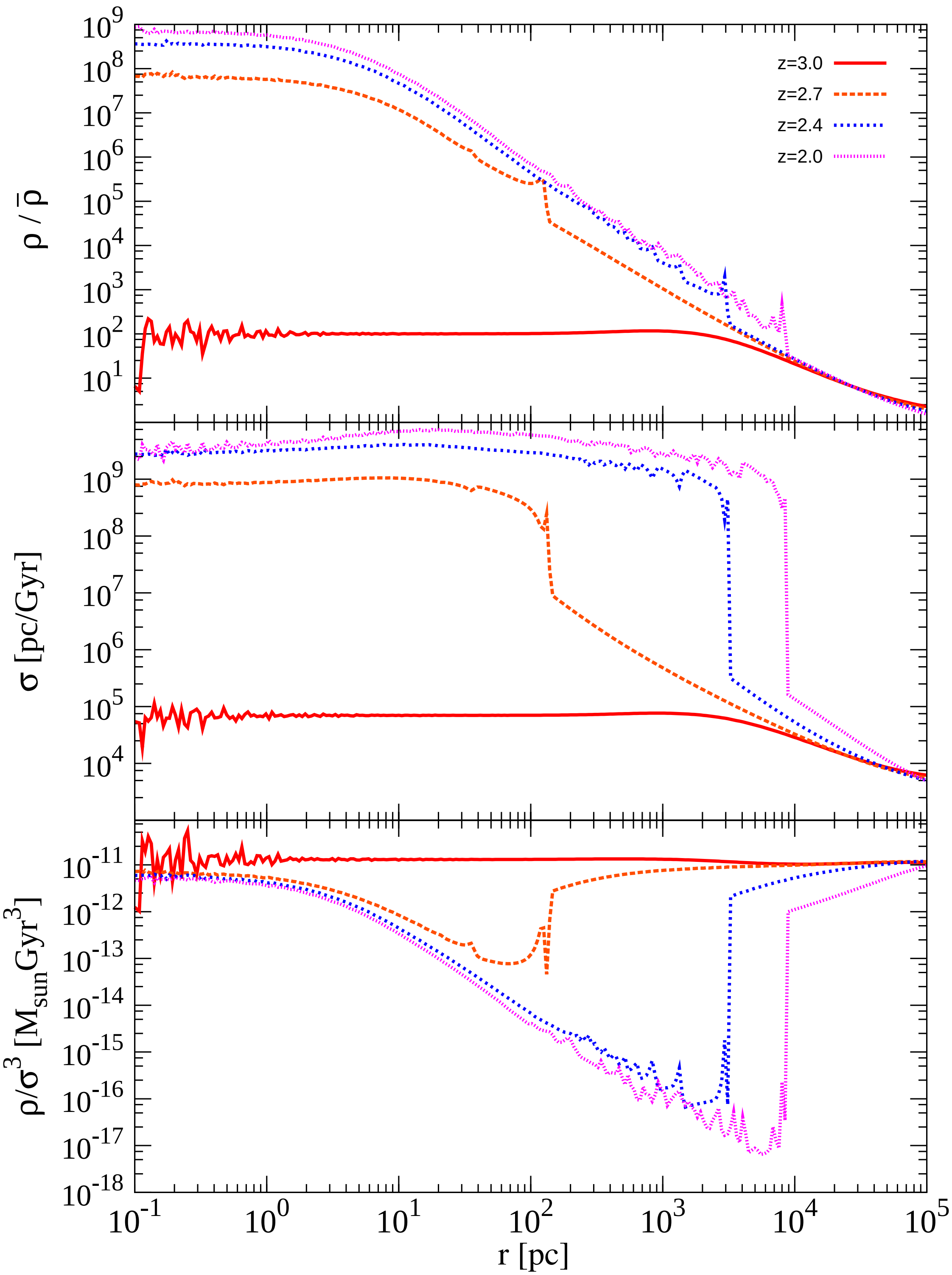

Figure 4.3: Collapsed profile as a function of time. The top panel shows the halo density profile $\rho(r)$, in units of the mean matter density $\bar{\rho}$, at various redshifts before, during, and after collapse at $z \sim 2.7$. The middle panel shows the 3-D velocity dispersion. The bottom panel shows the pseudo-phase-space density ρ/σ^3.

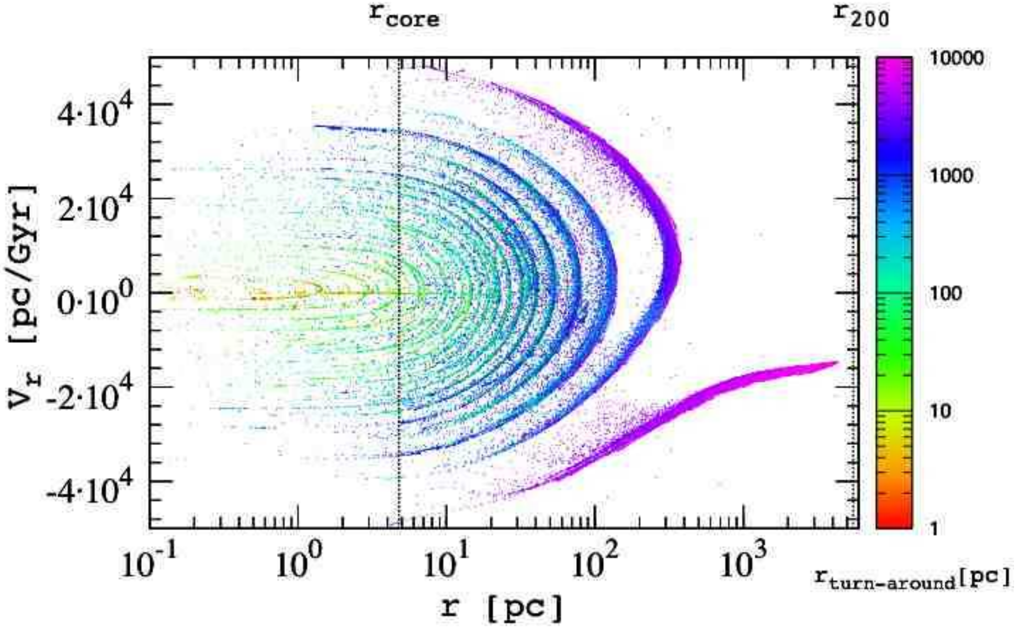

Figure 4.4: Radial behavior. Depicted are the radii r and radial velocities v_r for a subset of particles at $z = 2.7$. The color for each point indicates each particle's turnaround radius.

density, and typically our simulations give $\alpha \approx 1 - 2$. We are mainly interested, however in the core radius. As Figure 4.4 shows, $r_{\rm core}$ coincides with the typical location of the periapse of the infalling particles. Both the density and pseudo-phase space density plateau at $r_{\rm core}$, the latter saturating at a value near the phase space density of unvirialized material outside the halo as expected from the [91] bound.

Figure 4.5 illustrates the evolution of the halo structural parameters over time. Following formation, the halo continues to accrete matter and steadily grows in mass, at a rate determined by the initial linear overdensity profile. By definition, this growth in M_{200} means that r_{200} grows as well. Note, however, that $r_{\rm core}$ decreases as the halo grows, due to adiabatic contraction of the orbits as the halo potential deepens over time. Since $r_{\rm core}$ only shrinks in time, while r_{200} grows in time, the ratio between the two is clearly maximized at the time of formation of the halo.

Lastly, in Figure 4.6 we plot the breakdown of the contributions to the mass profile from various radii. The left panel decomposes the particles into shells of initial radius at $z = 100$, while the middle panel uses bins of turnaround radius $r_{\rm ta}$. At large radii, $r \gg r_{\rm core}$, the mass is dominated by recently infalling particles that originated at large Lagrangian radius and have large turnaround radii, similar to the behavior found in cold spherical collapse [28]. However, this changes on scales of order the core radius. Near $r_{\rm core}$, many different shells spanning decades in radius contribute comparably to the density. When we bin the

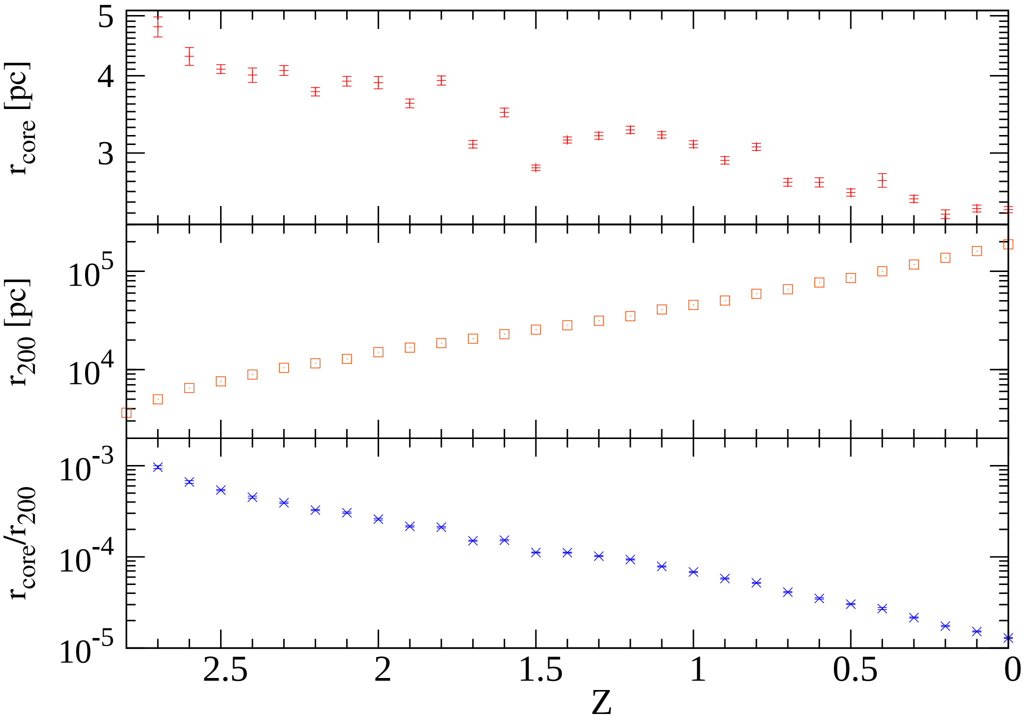

Figure 4.5: Time dependence of halo properties. The upper, middle and lower panels show r_{core}, r_{200}, and the ratio r_{core}/r_{200} respectively, as a function of redshift. As the halo grows in mass over time, the virial radius grows, while the core radius shrinks due to adiabatic contraction. The ratio r_{core}/r_{200} is therefore maximized at the time of halo formation, and only diminishes thereafter.

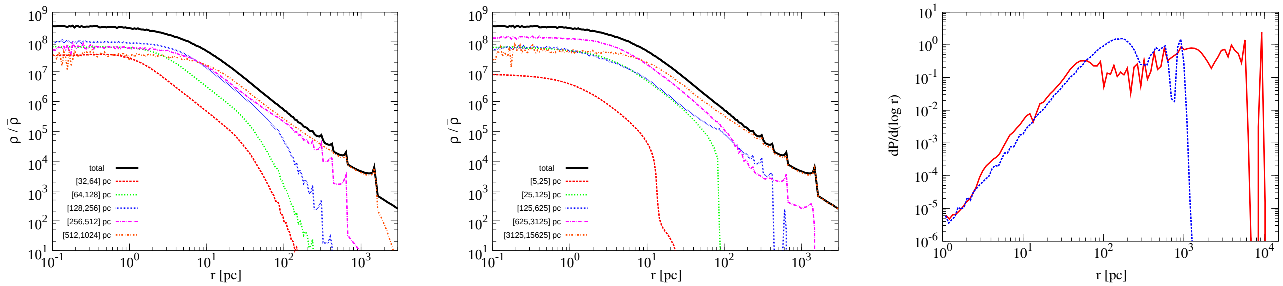

Figure 4.6: Breakdown of the mass distribution. The left panel shows the contribution to the mass density $\rho(r)$ at $z = 2.7$ originating from shells at various initial radii at $z = 100$. The middle panel shows a similar breakdown, instead binning particles based on their radii at turnaround. The right panel shows the distribution of initial radii (blue dashed) and turnaround radii (red solid) for all particles with $r < r_{\text{core}}$ at $z = 2.7$.

particles based on initial, Lagrangian radius, we can see that each shell has a different core radius, roughly scaling as $r_{\rm core} \propto r_{\rm L}$, as may be expected from the arguments given in the introduction. When we bin the particles based on their turnaround radii, we can see that the typical apoapse for each shell scales like the turnaround radius. For shells with $r_{\rm apo} > r_{\rm core}$, the enclosed mass profile behaves as

$$M_{\rm shell}(r) \propto r_{\rm L}^3 \times \frac{r}{r_{\rm apo}} \times \begin{cases} 1 & r \gg r_{\rm core} \\ \left(\frac{r}{r_{\rm core}}\right)^2 & r \ll r_{\rm core} \end{cases} \tag{4.17}$$

and since $r_{\rm core} \propto r_{\rm L}$ for each shell, we see that inside the core radius, the mass profile deposited by each shell of width $d\log r_{\rm L}$ scales as $M_{\rm shell} \propto r^3 \times (r_{\rm L}/r_{\rm apo}) \propto r^3 \times (r_{\rm L}/r_{\rm ta})$. (For shells with $r_{\rm apo} < r_{\rm core}$, the enclosed mass simply behaves as $M_{\rm shell}(r) \propto (r_{\rm L} r/r_{\rm core})^3$, of course.) For cold collapse, there is a one-to-one relationship between the turnaround radius $r_{\rm ta}$ and the initial radius, that depends on the initial linear density profile of the peak collapsing to form the halo. Roughly speaking, if locally the linear density has slope γ, in the sense that $\delta \propto r_{\rm L}^{-\gamma}$, then $r_{\rm ta} \propto r_{\rm L}^{1+\gamma}$ [52]. The tight relationship between $r_{\rm L}$ and $r_{\rm ta}$ degrades somewhat for warm collapse, but we can still use the same basic scaling. For shells inside the free-streaming scale, $r_{\rm L} < r_{\rm fs}$, the peak profile is quite flat with local slope $\gamma \approx 0$, and so $r_{\rm ta} \propto r_{\rm L}$. For these shells, $M_{\rm shell}(r)$ becomes roughly independent of the shell's initial radius for $r < r_{\rm core}$, as is seen in Fig. 4.6. For larger radii, $r_{\rm L} \gtrsim r_{\rm fs}$, the slope of the initial profile becomes nonzero, $\gamma > 0$, implying that shells originating from large radius become subdominant inside the core radius. Thus, the mass inside the core radius is dominated by shells with $r_{\rm L} \lesssim r_{\rm fs}$ and $r_{\rm apo} > r_{\rm core}$, and receives roughly equal contributions per decade within this range, as is seen in the right panel of Figure 4.6.

4.3.2 Dependence on physical parameters

Having established the basic features of the halo structure, we now explore the physics that sets those properties. The two main differences between WDM and CDM are the cutoff in the power spectrum, and the relic thermal velocities of DM particles at the time of halo formation. Both of these differences influence the size of halo core radii. To disentangle the different effects, we have performed collapse simulations in which we hold fixed the linear density profile of the initial peak, but vary the WDM temperature. This corresponds to holding fixed the halo assembly history, but varying the random motions near the time of collapse. The argument given in section 1 (e.g., Eqn. (4.3)) would predict that $r_{\rm core}$ would scale linearly with temperature, and our calculations appear consistent with this, as shown in Fig. 4.7. As we vary the temperature, the overall assembly history and structure of the halo remains unchanged (e.g., the location and height of the caustics), however the core radius varies. We find that a simple linear scaling, $r_{\rm core} \propto T$, appears consistent with our simulations. We note, however, that this linear behavior breaks down at very high temperatures, when the particles' random velocities become of order the Hubble velocity at the time of halo collapse. In this regime, the thermal motions are no longer a small

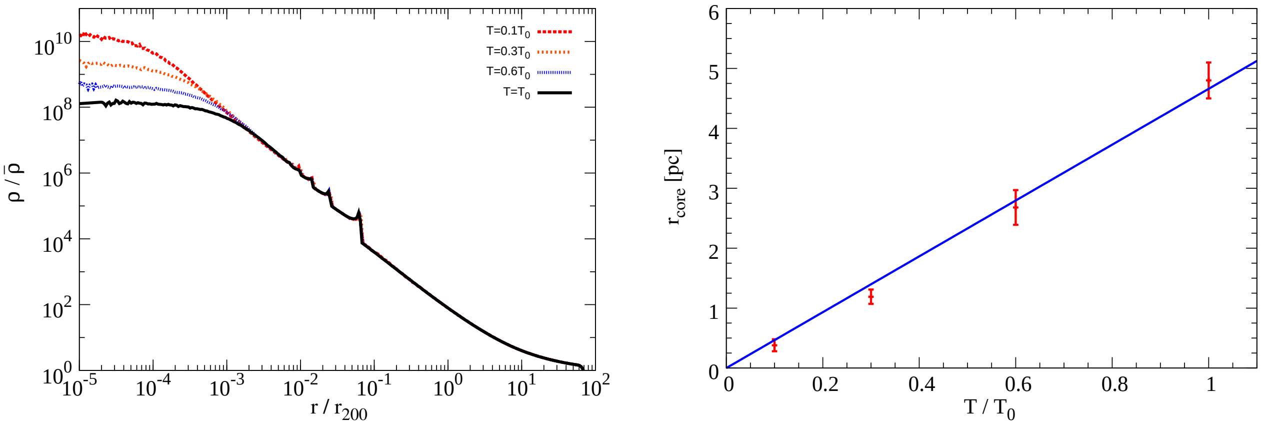

Figure 4.7: Temperature dependence of the halo profile for a fixed initial peak profile. (Left) The black solid curve shows the halo profile at redshift $z = 2.7$ for $T = T_0$, where T_0 is the WDM temperature consistent with the linear overdensity of the initial peak. For comparison, the red, orange and blue curves show the profile for $T = 0.1T_0$, $T = 0.3T_0$ and $T = 0.6T_0$ respectively. (Right) The points show the fitted core radii for the profiles depicted in the left panel, using Eqn. (4.16), while the blue line shows a simple linear scaling $r_{\rm core} \propto T$.

perturbation to the particle dynamics, and the overall collapse of the halo is significantly modified, unsurprisingly. Of course, such calculations are not self-consistent: the large random motions that modify halo collapse at low redshift would have erased the initial linear density perturbations responsible for the halo, at a higher redshift.

This establishes that at fixed initial peak profile (i.e. fixed halo assembly history), the core radius scales linearly with DM temperature. It is inconsistent, however, to hold fixed the initial peak profile while the temperature is varied, since the random thermal motions of DM particles erase structure at high redshift and modify the peak profiles in the linear regime of structure formation. Therefore, we next explore how the core radius behaves as we self-consistently vary both the WDM temperature and the initial peak profile. We know that $r_{\rm fs}$ scales roughly linearly with T, and we have just seen that at fixed $r_{\rm fs}$, the core radius $r_{\rm core}$ also scales linearly with T. Therefore, if $r_{\rm core}$ were independent of the halo assembly rate, then both $r_{\rm core}$ and $r_{\rm fs}$ would scale linearly with T, and the ratio $r_{\rm core}/r_{200}$ would be independent of the WDM temperature, as we argued in Section 1. Figure 4.8 shows that this behavior is not confirmed by our simulations, however. The figure shows the results of simulations using temperatures 5 times larger, and smaller, than our fiducial calculation. The red solid curve shows the density profile for $r_{\rm fs} = 20\,h^{-1}$ kpc, orange dashed shows our fiducial run with $r_{\rm fs} = 100\,h^{-1}$ kpc, and blue dotted shows results for $r_{\rm fs} = 500\,h^{-1}$ kpc. In all three cases, we set the initial peak height so that collapse will occur near $z = 3$. As expected, r_{200} scales close to linearly with $r_{\rm fs}$: the three simulations give $r_{200} = 1.2$, 5.5, and 22.6 kpc at the formation redshift $z = 2.7$. However, $r_{\rm core}$ does not scale linearly with $r_{\rm fs}$: the three simulations give $r_{\rm core}$=0.6, 4.8 and 43 pc respectively. The ratio $r_{\rm core}/r_{200}$ is not independent of $r_{\rm fs}$, but instead behaves roughly as $r_{\rm fs}^{1/2}$ over the range that we have

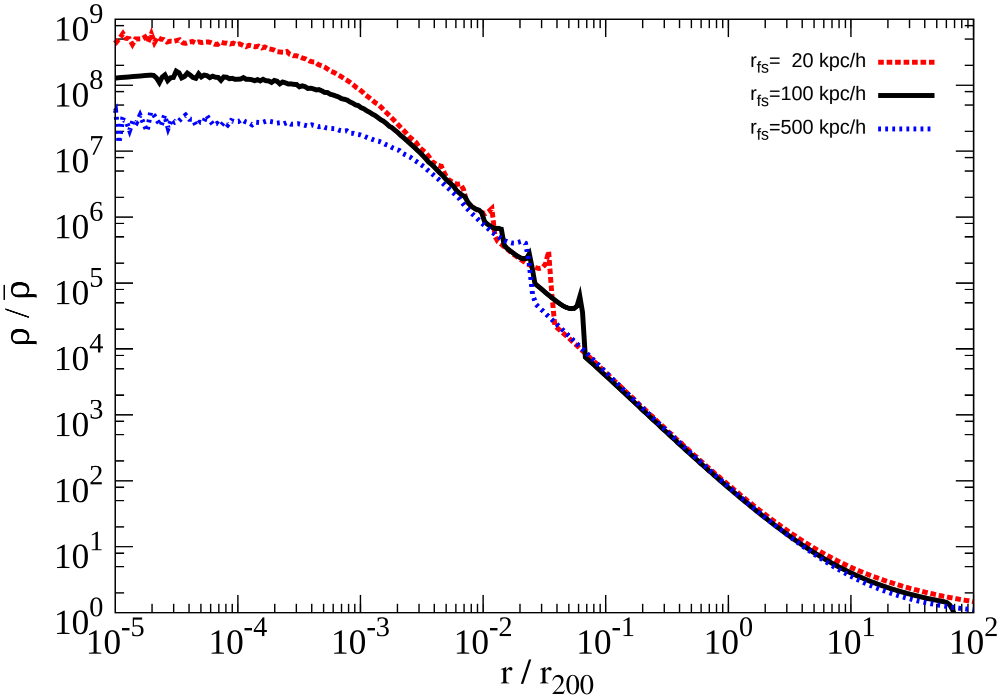

Figure 4.8: Effect of WDM temperature. Density profiles at $z = 2.7$ for different initial peak profiles consistent with WDM temperature that produce $r_{fs} = 20$, 100 and 500 kpc/h are plotted in dashed red, solid black and dotted blue lines respectively.

considered. Evidently, the core radius depends not only on the DM temperature at the time of halo formation, but also upon the halo assembly rate.

Lastly, we examine the dependence of the core radius on the halo formation time. We do so, simply by adjusting the height of the initial peak, holding fixed the WDM temperature and the radial shape of the peak profile. Figure 4.9 shows one example, comparing our fiducial simulation (with $z_{\rm form} = 2.7$) with a run using the same WDM temperature, but with initial peak height a factor of 4 larger. The later simulation has $z_{\rm form} = 13.6$. The halo masses of the two simulations are similar, as expected: $r_{200} = 1.3\,$kpc for the $z = 13.6$ halo, compared to $r_{200} = 5.5\,$kpc for the fiducial $z = 2.7$ halo. The core radius for the earlier-forming halo is $r_{\rm core}$=2.8 pc, compared to 4.8 pc for the fiducial halo, so that the ratio $r_{\rm core}/r_{200}$ changes by a factor of 2.8. The simple argument given in section 1 would have predicted that $r_{\rm core}/r_{200}$ would scale as $(1 + z_{\rm form})^{1/2}$, whereas our simulation appears more consistent with a scaling $r_{\rm core}/r_{200} \propto (1 + z_{\rm form})^{2/3}$. This is only based on one comparison, of course. This is the result at the formation time; at $z = 0$ the ratio $r_{\rm core}/r_{200}$ would be smaller by at least a factor of $1/(1 + z_{\rm form})$, as we argued earlier.

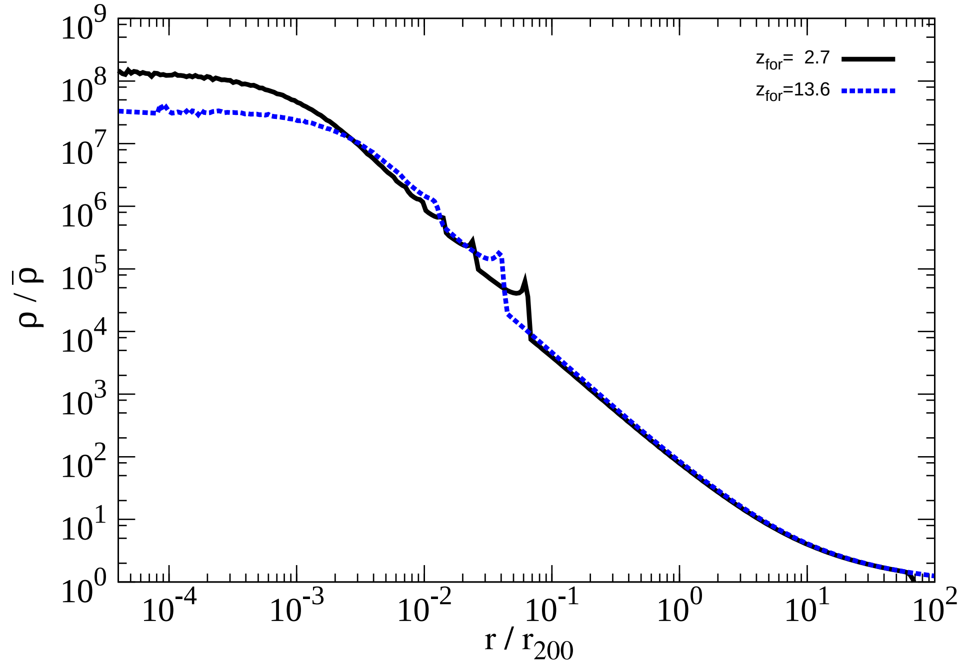

Figure 4.9: Effect of initial peak height. The solid black line shows the profile at collapse time $z = 2.7$ for a peak height normalization of $\bar{\delta}(r_{\rm L} = 100$ Kpc/h, z=3)=1.686. In contrast, dashed blue shows the profile at collapse time z=13.6 for a peak height normalization of $\bar{\delta}(r_{\rm L} = 100\,h^{-1}$ kpc, z=15)=1.686.

4.4 Discussion and summary

We have investigated the formation of halos in warm dark matter cosmologies. Our study of spherical collapse of WDM halos indicates that core radii do indeed arise in these cosmologies, as expected from simple phase-space arguments [91]. However, we find that WDM core radii are generically small, typically of order 10^{-3} of the halo virial radius at the time of formation, and considerably smaller following formation. This is for halos forming at the cutoff scale; higher mass halos will have substantially smaller $r_{\rm core}/r_{200}$. We have investigated the dependence of the core radius on various physical parameters such as the WDM temperature, halo formation redshift, and halo mass. For the allowed range of WDM temperatures (e.g. $M_{\rm fs} \lesssim 10^9 M_\odot$), the core radii of halos observed at $z = 0$ are generically expected to be far smaller than the core sizes measured in certain LSB galaxies, with $r_{\rm core}/r_{200} \approx 0.05$.

Our calculations have all assumed spherical symmetry, whereas halo formation in both CDM and WDM cosmologies is highly nonspherical. We would argue, however, that our conclusions regarding WDM cores are likely to be valid for non-spherical collapse as well. One line of evidence supporting this argument is the fact that the pseudo-phase-space density profiles of our halos are quite similar to the profiles of halos in CDM simulations, with $\rho/\sigma^3 \propto r^{-2}$, roughly speaking [56]. This similarity is presumably a consequence of the virial theorem, which ensures that $\rho/\sigma^2 \sim r^{-2}$. For WDM halos, the power-law rise of the pseudo-phase-space density towards small r saturates when ρ/σ^3 approaches the Tremaine-Gunn bound, and this saturation will occur for both spherical and nonspherical collapse. Now, we would expect the value of the pseudo-phase-space density to be similar at the virial radius for both spherical and non-spherical collapse, since the halo mass and virial radius are by definition the same in the two cases, and so $\rho \sim M/4\pi r^3$ and $\sigma \sim (GM_{200}/r_{200})^{1/2}$ will be similar for the two cases. We have noted that ρ/σ^3 rises as roughly r^{-2} inside the virial radius in spherical and nonspherical collapse, and in both cases the core radius occurs where ρ/σ^3 approaches the Tremaine-Gunn bound. So we have good reason to believe that halo core radii will not be significantly larger for nonspherical collapse than for spherical collapse, just because the ρ/σ^3 profiles appear similar.

The other possible loophole in our argument is that we have assumed that no halos form below the cutoff scale in the power spectrum. N-body simulations have not yet conclusively determined whether or not halos with $M \ll M_{\rm fs}$ arise in WDM cosmologies, due to numerical difficulties associated with simulating truncated power spectra [100]. We have begun investigating this issue, and our preliminary results indicate that halos may form below the cutoff scale, though it is unclear whether they can form in sufficient numbers to account for observed LSB galaxies.

Our results indicate that warm dark matter cosmologies cannot produce halos with core radii large enough to account for the density profiles of observed LSB galaxies. This would suggest that the origin of these observed cores lies within astrophysics, rather than particle physics.

Chapter 5

Neutrino halos in clusters of galaxies and their weak lensing signature

In this chapter we study the possible detection of relic cosmological neutrinos by computing the weak lensing signal of halos of neutrinos, formed in the gravitational potential well of clusters of galaxies. This chapter is a reproduction of the paper:

Neutrino halos in clusters of galaxies and their weak lensing signature, Francisco Villaescusa-Navarro, Jordi Miralda-Escudé, Carlos Peña-Garay & Vicent Quilis, 2011, JCAP, 06, 27

5.1 Introduction

The discovery of neutrino flavour conversion of solar, atmospheric, reactor and accelerator neutrinos implies that at least two of the three light neutrinos are massive. The sum of the neutrino masses is still unknown. It is constrained from above ($\sim$ eV) by tritium beta decay end point data and by cosmological data, and from below (0.05 eV) by neutrino oscillation data. The neutrino mass squared differences are precisely measured by reactor and accelerator experiments, [33]

$$\Delta m^2_{21} = (7.6 \pm 0.2) \times 10^{-5} eV^2 \ , \tag{5.1}$$

$$\Delta m^2_{31} = (2.4 \pm 0.1) \times 10^{-3} eV^2 \ . \tag{5.2}$$

However, the neutrino mass hierarchy, or whether the two neutrinos with the smallest mass difference are heavier or lighter than the other one, is still unknown. Recent forecasts of galaxy clustering have included the neutrino mass ordering in addition to the total neutrino mass among the free model parameters that are considered, and show that future surveys should reach the sensitivity required to explore most of the allowed range of the total neutrino mass and to determine the neutrino hierarchy [43].

Neutrino masses are usually included in the list of parameters of the standard model of cosmology in the linear regime, but this has rarely been done in the nonlinear case. Massive neutrinos suppress the small scale matter power spectrum due to their large thermal velocities, making the shape of the total mass power spectrum a potential probe to neutrino masses. On scales much smaller than the free-streaming distance of neutrinos, the relative suppression is [51],

$$\left|\frac{\Delta P(k)}{P(k)}\right| \simeq 10\frac{\Omega_\nu}{\Omega_m}, \tag{5.3}$$

where $\Omega_\nu h^2 = (\Sigma_i m_i)/(93.14 \text{ eV})$.

Apart from this linear effect, massive neutrinos are also expected to cluster around gravitationally collapsed dark matter haloes as their streaming velocities are reduced and become comparable to the velocity dispersions of the halos, thereby modifying the dark matter halo total mass density profile. Previous work has studied this non-linear neutrino clustering [84, 75, 13, 16, 94, 61]. Here, we present a new calculation with updated parameters and a more realistic halo model. We also examine weak gravitational lensing as a method for an astrophysical detection of the cosmic relic neutrinos. We find that weak gravitational lensing all-sky surveys, such as the planned EUCLID mission, may detect the presence of the neutrino perturbation in the average mass density profile of clusters of galaxies, although systematic uncertainties related to the impact of baryons on the redistribution of the total mass profile are likely to be severe.

In Section 2 we describe our method for computing the relic neutrino clustering within dark matter haloes, and the results are shown in Section 3. Section 4 discusses how the effect of relic neutrino clustering within dark matter haloes can be detected by weak lensing.

We use the ΛCDM flat model with $\Omega_M = 0.27$ and Hubble constant $H_0 = 70\,\mathrm{km\,s^{-1}\,Mpc^{-1}}$ throughout the paper, with a power spectrum normalization $\sigma_8 = 0.9$ and primordial slope $n_s = 0.96$.

5.2 Numerical method

This section describes the method we use to compute the neutrino density profile in a spherical model of the dark matter halo.

5.2.1 Mass density profile

In this study we consider neutrinos as test particles moving in a gravitational potential determined from a spherical model of the distribution of the cold dark matter, which dominates the total mass in clusters. Our model adopts the numerical fits that have been obtained from cosmological numerical simulations of the formation of halos from cold dark matter. We calculate a density profile including the inner virialized region and the outer infall region of a halo by smoothly joining two different pieces. The first piece is the NFW profile

[66], valid inside the virial radius. The second piece is obtained starting from the average initial density perturbation around a halo in a Gaussian random field, and evolving it in the non-linear regime by assuming spherical gravitational collapse without shell-crossing [4, 55]. The two pieces are joined together at an assumed epoch of observation and at a certain radius, which is determined by requiring continuity in the density profile (the derivative of the density profile is allowed to be discontinuous at the junction point).

The NFW profile has two parameters, the halo mass and its concentration parameter, and is given by

$$\rho_{_{NFW}}(r) = \frac{\rho_s}{(r/r_s)(1+r/r_s)^2} \ , \tag{5.4}$$

where the concentration parameter is $c = r_v/r_s$, and the virial radius r_v is obtained from the halo mass as

$$M = \frac{4\pi}{3}\rho_c \Delta_c r_v^3 \ . \tag{5.5}$$

Here, ρ_c is the critical density of the universe at redshift z, and Δ_c is the halo mean density within the virial radius in units of the critical density, which for a flat universe with a cosmological constant is given by [17]:

$$\Delta_c = 18\pi^2 + 82x - 39x^2 \ , \tag{5.6}$$

$$x = \Omega(z) - 1 \ , \tag{5.7}$$

$$\Omega(z) = \frac{\Omega_m(1+z)^3}{\Omega_m(1+z)^3 + \Omega_\Lambda} \ . \tag{5.8}$$

The NFW profile is a fit to the density profile of the halo obtained in numerical simulations for the virialized region. Outside this region, we use instead a density profile obtained from the mean mass distribution around any mass concentration, in a Gaussian field with power spectrum $P(k)$ [55]. Let the rms mass fluctuation within a sphere of radius r be $\sigma_M(r)$. The average linear overdensity $\overline{\delta}_2 = \nu_2 \sigma_M(r_2)$ within a radius r_2, under the condition that the mean linear overdensity within the smaller radius r_1 is equal to $\overline{\delta}_1 = \nu_1 \sigma_M(r_1)$, can be calculated as $\nu_2 = \gamma_{12}\nu_1$, where

$$\gamma_{12} = \frac{9}{2\pi^2 \sigma_M(r_1)\sigma_M(r_2)} \int_0^\infty dk \ P(k) \left[\frac{j_1(kr_1)}{r_1}\right]\left[\frac{j_1(kr_2)}{r_2}\right] \ , \tag{5.9}$$

where j_1 is the spherical Bessel function. We use this equation to obtain the average linear overdensity profile around a halo.

The outer halo density profile beyond a certain radius r_{f0}, which is to be determined by a matching condition that is specified below, is then calculated as follows: we start with a guessed value of r_{f0} with a mean interior overdensity $\overline{\delta}_{f0}$ in the NFW profile. The corresponding initial radius r_{i0} is obtained from $(1 + \overline{\delta}_{f0}) = (r_{i0}/r_{f0})^3$. Assuming the spherical collapse model with no shell-crossing (i.e., a constant interior mass), we calculate the required extrapolated linear overdensity $\overline{\delta}_{i0}(r_{i0})$ to produce the final overdensity $\overline{\delta}_{f0}(r_{f0})$. We then evaluate the linear mean overdensity $\overline{\delta}_i(r_i)$ at any radius $r_i > r_{i0}$ with equation (5.9), using the power spectrum of Eisenstein & Hu [27] with the parameters $\Omega_m = 0.27$, $\Omega_\Lambda = 0.73$, $\sigma_8 = 0.9$, $n_s = 0.96$ and $h = 0.7$. Finally, using again the spherical collapse model, we compute the final radius r_f corresponding to each initial radius r_i and its linear overdensity $\overline{\delta}_i(r_i)$. The non-linear density profile is

$$\rho(r_f) = \rho_m \left(\frac{r_i}{r_f}\right)^2 \frac{dr_i}{dr_f} , \tag{5.10}$$

where the mean density of the universe is $\rho_m = \Omega(z)\rho_c$.

We choose the radius r_{f0} at which the inner NFW and the outer infall density profile are matched by requiring continuity of the mass density profile. The matching point that results from this continuity requirement at a specified redshift is located in all our calculations between 1.5 and 3 times the virial radius. In Figure 5.1, the density profile generated using this procedure is plotted for a dark matter halo of mass $M = 10^{15}h^{-1}M_\odot$ at $z = 0.4$ (red solid line). The dashed line shows the extrapolated NFW profile beyond the matching point. At large radius, the mean density profile obviously approaches the mean density of the universe. The figure also shows the profiles of other halos at a higher redshift with the average mass of the most massive progenitor of the halo at $z = 0.4$, as discussed below. The vertical dotted lines indicate the position of the virial radius of each halo.

5.2.2 Dark matter halo evolution

Modeling the orbits of relic neutrinos in a cluster halo requires the gravitational potential of the halo to be specified as a function of time. To obtain a realistic model for a typical halo, we use the results of [105] to obtain a mass of the halo as a function of time over its entire history of accretion. Obviously, there is a large dispersion in the accretion history of a halo and therefore in the evolution of its potential well, but we take an average history for the most massive progenitor as a typical case to calculate the orbits of the neutrinos in our spherical model.

We use the empirical formula of [105], obtained from a numerical fit to the results of N-body cosmological simulations, to calculate the mass and concentration parameter of the most massive progenitor of our halo of mass M_f at the final redshift z_f, for each earlier epoch at redshift $z > z_f$. This is done for 100 values of the redshift z, distributed logarithmically between $z = z_f$ and $z = 10$.

As this work was being carried out, we initially computed the density profile of the progenitor halo of mass $M_h(z)$ at each redshift z with the same method as for the final halo at redshift z_f, choosing a matching radius and requiring continuity with the average external density profile. However, this method does not conserve the total mass because it does not take into account the requirement that the mass M_f that is assembled into the final halo at z_f must be present in the external region around the progenitor halos within

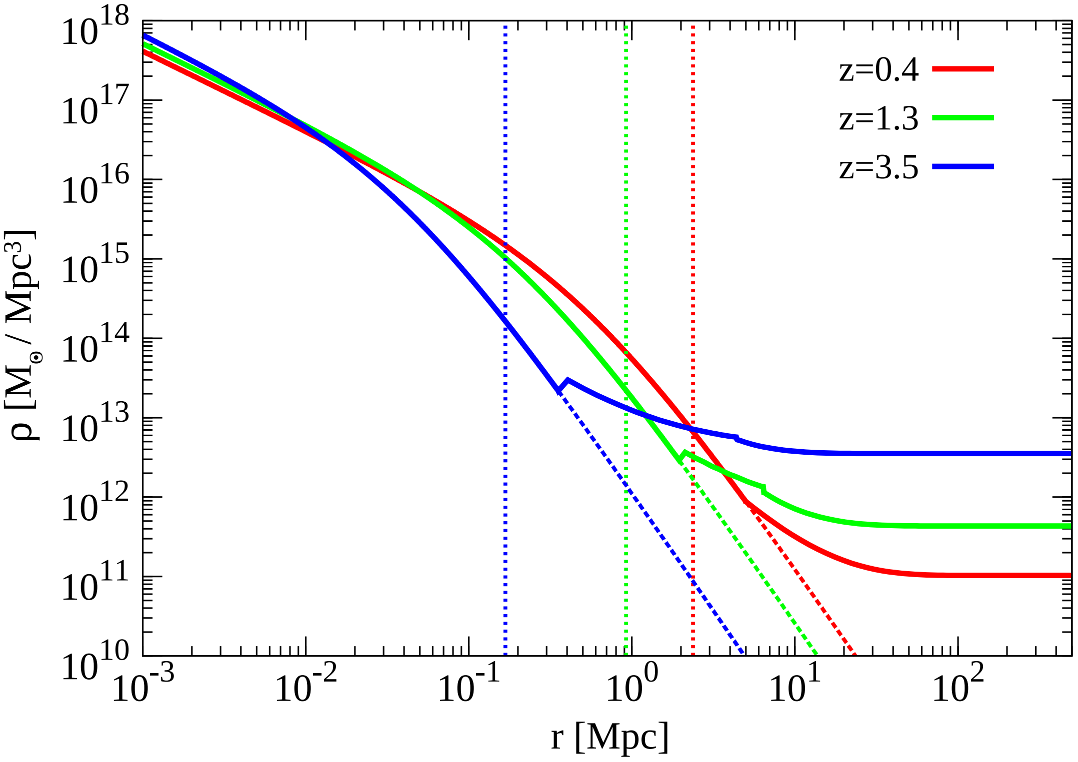

Figure 5.1: Red solid line shows the adopted mean dark matter halo density profile at redshift $z = 0.4$ for $M_\Delta = 10^{15}h^{-1}M_\odot$. The inner profile is the NFW model, matched with the outer profile computed from the average spherical perturbation around a halo evolved according to spherical collapse. The dashed line shows the extrapolation of the NFW model beyond the matching point. The green and blue lines show the density profile of the most massive progenitor at redshifts $z = 1.3$ and $z = 3.5$, respectively, with masses (M_Δ) $2.1 \times 10^{14}h^{-1}M_\odot$ and $8.5 \times 10^{12}h^{-1}M_\odot$. The density profiles of these halos are not continuous at the matching point, and their outer profile is determined by mass conservation as required for assembling the halo at $z = 0.4$. The vertical dotted lines indicate the position of the virial radius for the three halos. The matching point chosen for continuity generally occurs around twice the virial radius.

the shell that will finally collapse onto the halo at redshift z_f. In other words, the density profile around a progenitor halo of mass $M_h(z)$ is not equal to the average one as obtained from equation (5.9), but is modified by the condition that a halo of mass M_f must be assembled at redshift z_f. Therefore, the density profile of the progenitor halo is computed by fixing the matching point to the same fixed multiple of the virial radius r_v as for the final halo at z_f, $r_{f0}(z) = r_{f0}(z_f) \times r_v(z)/r_v(z_f)$, and tracing back in time the position of each spherical shell around the halo. At each step in redshift (backwards in time), the progenitor halo decreases its mass within $r_{f0}(z)$ by an amount δM, and a new spherical shell is added with mass δM with a radius equal to $r_{f0}(z)$. All the spherical shells are traced back in time using the spherical collapse model with no shell-crossing. This results in the density profiles shown in Figure 5.1 for two examples of the progenitor halos, at $z = 1.3$ (with mass $M = 2.1 \times 10^{14}\, h^{-1} M_\odot$) and at $z = 3.5$ (with mass $M = 8.5 \times 10^{12}\, h^{-1} M_\odot$). The density profile is no longer continuous at the matching point, but this does not cause any problem.

We have found that correctly computing the evolution of the conserved external mass distribution around the halo of a cluster is important: if one uses instead the mean density profile around a halo progenitor, the final result for the neutrino density can be underestimated by more than a factor of two.

The evolving potential of the halo is computed by interpolation from the mass profiles calculated at 100 values of the redshift z, as the orbits of test particles representing the neutrinos are integrated.

5.2.3 Neutrino orbits

The initial phase space distribution of neutrinos is determined by their state of thermal equilibrium reached in the early universe with the primordial plasma, i.e., the Fermi-Dirac distribution for highly relativistic particles,

$$f(p)\, dp = \frac{8\pi}{(2\pi\hbar)^3} \frac{p^2 dp}{e^{p/T} + 1} \ . \tag{5.11}$$

The neutrino temperature, evolving as $T = T_0(1 + z)$, is related to the photon temperature $T_{\gamma 0}$ as $T_0 = (4/11)^{1/3} T_{\gamma 0} \approx 1.9$ K.

The orbits followed by neutrinos in our time-dependent spherical potential depend on three orbital parameters: the initial radius and momentum, and the angular momentum of the neutrino. To compute the neutrino density profile, this three-parameter space of neutrino orbits needs to be sampled densely enough to compute their average spatial distribution as a function of time. For this purpose, we divide the initial radius, momentum and angular momentum into several bins, and compute a neutrino orbit for each binned value of the three variables, starting the orbits at $z_i = 10$. This three-dimensional phase-space grid is constructed taking particular care to resolve the particles reaching close to the center of the halo, which are at small initial radius or small angular momentum.

The grid is constructed using 10000 bins in radius from 0 to r_{max}, distributed as $r_i = r_{max}(i/10000)^2$, where r_{max} is large enough to ensure convergence of the final neutrino density profile out to a final radius of at least 30 Mpc. Momentum bins are similarly set by $p_j = p_{max}(j/500)^2$, with 500 bins, where $p_{max} = 0.005(1+z_i)$ eV, sufficient to sample particles out to the largest momenta making any significant contribution. Finally, the angular momentum is sampled from 0 to $L_{max} = r_i p_j$ using 200 bins distributed as

$$\begin{cases} \theta_k = \left(\frac{\pi}{2}\right)\left(\frac{k}{100}\right)^{\alpha} \quad (k \leqslant 100)\ , \\ \\ \theta_k = \pi - \left(\frac{\pi}{2}\right)\left(\frac{k-100}{100}\right)^{\alpha} \quad (k > 100)\ , \end{cases} \tag{5.12}$$

where θ_k is the angle subtended between the initial momentum and radius of the particle. Here, α is a parameter to control the sampling of particles with low angular momentum, which are responsible for the shape of the density profile in the inner parts. Typically, it ranges between 1.5 to 5 depending on both neutrino and dark matter halo mass. At each three-dimensional bin, neutrino orbits are computed by solving the equation

$$\frac{d^2r}{dt^2} - \frac{L^2}{r^3} = -\frac{\partial\phi(r,t)}{\partial r}\ , \tag{5.13}$$

where L is the conserved angular momentum per unit of mass and ϕ is the time-dependent Newtonian gravitational potential, computed from the dark matter density profile specified in Section 2.1. The contribution of each neutrino particle to the final neutrino density profile as a function of time is counted as a spherical shell of radius $r(t)$ and mass proportional to the weight of the bin at radius r_i, momentum p_j and angle θ_k in the phase space distribution,

$$m_p^{i,j,k} \propto \int_{r_i}^{r_{i+1}} r^2\, dr \int_{p_j}^{p_{j+1}} \frac{p^2 dp}{e^{p/T_\nu(z)}+1} \times \|\cos\theta_{k+1} - \cos\theta_k\|\ . \tag{5.14}$$

The final neutrino density profile is obtained by adding the mass of all interior shells at any radius and time. Equation (5.13) is solved for each particle with a Runge-Kutta fourth-order integrator with variable stepsize.

5.3 Neutrino density profiles

We now present the results for the spherical neutrino density profiles. We will discuss four neutrino mass schemes: a) three neutrinos with $m = 0.3$ eV (labelled 0.3 eV), b) three neutrinos with m=0.15 eV (labelled 0.15 eV), c) two neutrinos with 0.05 eV and one massless neutrino (labelled IH 0.05eV) and d) one neutrino with 0.05 eV and two massless neutrinos (labelled NH 0.05eV). We neglect the mass squared differences in schemes a and b and the small mass squared difference in schemes c and d. This approximation is justified because the masses of the neutrinos that we consider to have equal mass differ by less than 1 % (scheme a) , 5% (scheme b), and 2% (scheme c). In scheme c and d, the neutrinos that we neglect have masses smaller than 0.01 eV, and as we shall see their contribution to the

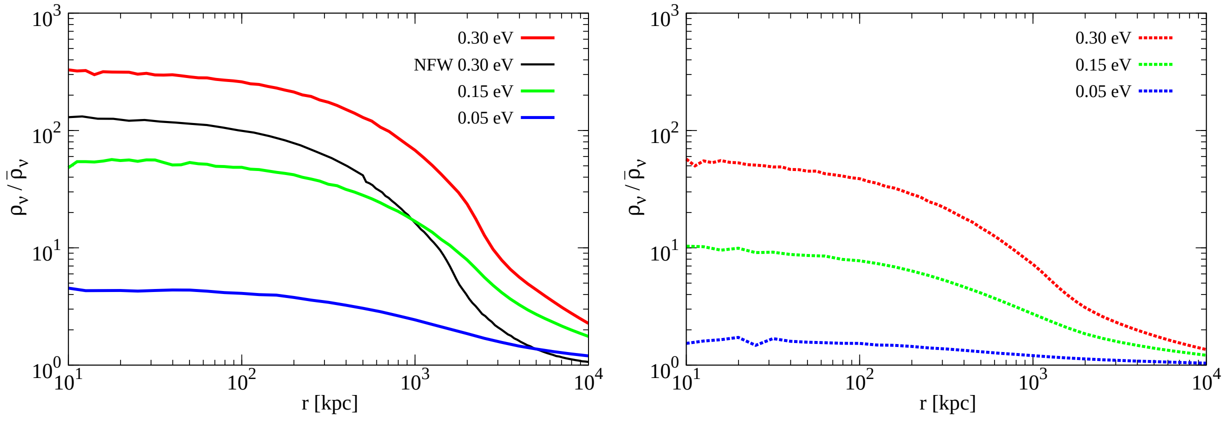

Figure 5.2: Neutrino density profiles at $z = 0.4$, shown as the ratio to the mean neutrino density, for a halo mass of $10^{15}\, h^{-1} M_\odot$ (left panel) and $10^{14}\, h^{-1} M_\odot$ (right panel), and for the indicated neutrino masses. The case where the NFW profile is used at all radii (with a suppressed density at large radius, see Figure 5.1) is shown for one case in the left panel as a black line.

total neutrino mass profile is indeed negligible. With this approximation, neutrino density profiles need to be computed only for masses of 0.3, 0.15 and 0.05 eV.

Neutrino density profiles are shown at $z = 0.4$ in Figure 5.2 in units of the mean cosmic neutrino density, for halos of mass $10^{15}\, h^{-1} M_\odot$ (left) and $10^{14}\, h^{-1} M_\odot$ (right), and for neutrino masses of 0.05, 0.15 and 0.3 eV. The neutrino overdensity increases with both neutrino mass and halo mass, as the ratio of the halo velocity dispersion to the neutrino thermal velocities increases. The size of the core of the neutrino distribution decreases rapidly with this ratio owing to phase space density conservation. The random oscillations at small radius are due to numerical noise arising from the number of particles representing spherical shells in our simulation.

The left panel also shows, for a neutrino mass of 0.3 eV, the case of the NFW mass profile extended over all radii. This results in a reduced density, as seen in Figure 5.1. The reduction of the depth of the potential well in this model reduces the neutrino density.

In Figure 5.3, the ratio of the neutrino to the dark matter mass density profile, ρ_ν / ρ_{DM}, is plotted for a halo of mass $10^{15}\, h^{-1} M_\odot$ at $z = 0.4$, for neutrino masses of 0.3, 0.15 and 0.05 eV. Schemes a and b are used for the two heavier masses (i.e., the red and green curves show the density computed for one neutrino family multiplied by 3), and schemes c and for the lighter mass (the cyan curve is for one neutrino family, and the blue curve is for two). A change of slope occurs at a radius close to 5 Mpc, due to the change of slope in the mass density profile at the matching point between the NFW and the outer infall model of the average density perturbation. Near a radius of 2 Mpc, a feature is present that is particularly strong for the largest neutrino mass and becomes weak as the neutrino mass is decreased. This is the result of a caustic, a special feature of spherical collapse. For perfectly cold particles, a true caustic (where the density becomes formally infinite) would appear at this radius, at which the single infalling stream of particles outside the caustic changes to a superposition of three streams inside the caustic, owing to the particles that are turning around in their first orbit after going through the halo center. The caustic is increasingly smoothed out for neutrinos as their primordial velocity dispersion increases (i.e., the neutrino mass decreases), or as the halo mass decreases. In practice, this caustic feature is present only in a spherically symmetric system. Real clusters collapsing from random initial density perturbations have caustics that are highly irregular and occur at variable radii, influenced by their internal substructure and non-sphericity, and which are largely washed out when averaging over many clusters (see, e.g., [28, 98]). Note also that a caustic should of course also be present in the Cold Dark Matter in a spherical model, which we are not taking into account here because we are using a simple analytic model for the mass profile. The Cold Dark Matter would have its caustic washed out only by the effects of substructure and non-sphericity, while the neutrino caustic is further washed out by the initial thermal velocities.

Comparing our calculations with previously published results, we find that we reproduce the results by [75] when using their dark matter halo (NFW) density profile and halo evolution model, but we do not reproduce those of [84] (see [75] for a discussion of this difference). As we have shown, the NFW halo profile extrapolated to large radius that is used by [75] underestimates the neutrino contribution to the profile at large radius. Our model also improves that of [75] on the cluster evolution, by including the mean redshift dependence of the halo progenitor mass and concentration parameter, instead of a constant halo mass during the accretion history used in [75], and by computing also the mean spherical evolution of the density profile external to the halo.

Finally, in Figure 5.4 we plot the neutrino surface overdensity, which is important for our lensing calculations in the next section,

$$\Sigma_\nu(R) = \int_{-\infty}^{\infty} \left[\rho_\nu(r) - \overline{\rho}_\nu\right] dx \ , \tag{5.15}$$

where $r^2 = x^2 + R^2$, R is the projected radius on the sky and x is the dummy variable for integration along the line-of-sight, and $\overline{\rho}_\nu$ is the mean neutrino density, for the same cases of neutrino mass, and at redshifts $z = 0.4$ and $z = 1$. The left panel is for a halo mass $10^{15}\,h^{-1}M_\odot$, and the right panel for $10^{14}\,h^{-1}M_\odot$. The same main effect is clearly seen as previously: the core radius of the neutrinos is reduced, and their central overdensity increases, as the halo mass or neutrino mass increases.

5.4 Neutrino detection with weak lensing

We now consider the possibility of detecting the perturbation caused by neutrinos on the radial density profile of a cluster using weak gravitational lensing. In this section we consider the idealized case where weak lensing can be measured for a large number of clusters with

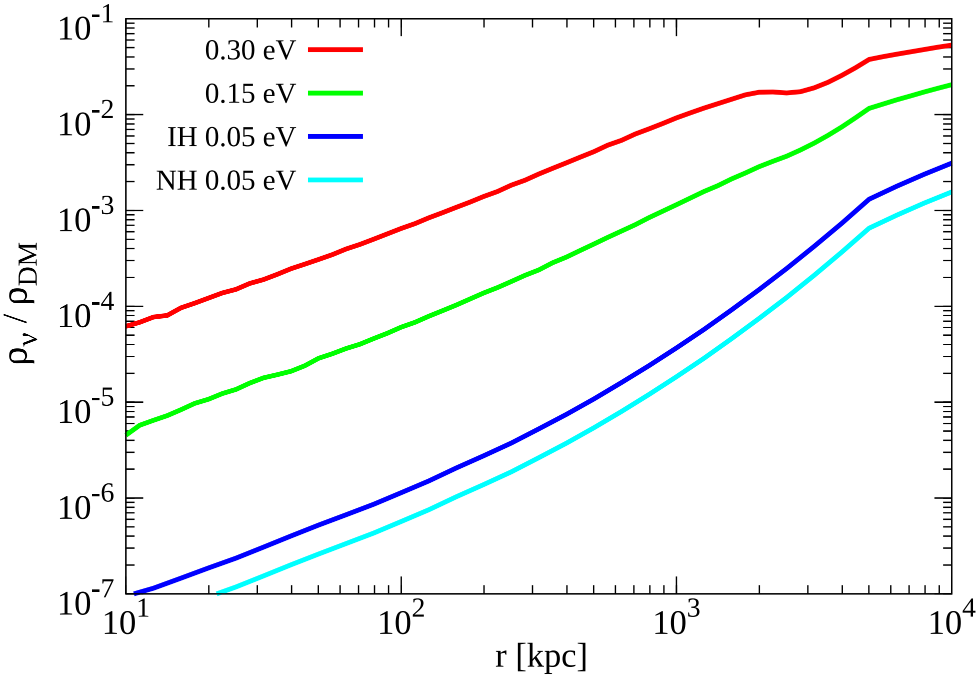

Figure 5.3: The neutrino to dark matter density profiles ratio at $z = 0.4$ for the indicated neutrino masses, in a halo of mass of $10^{15}\, h^{-1} M_\odot$.

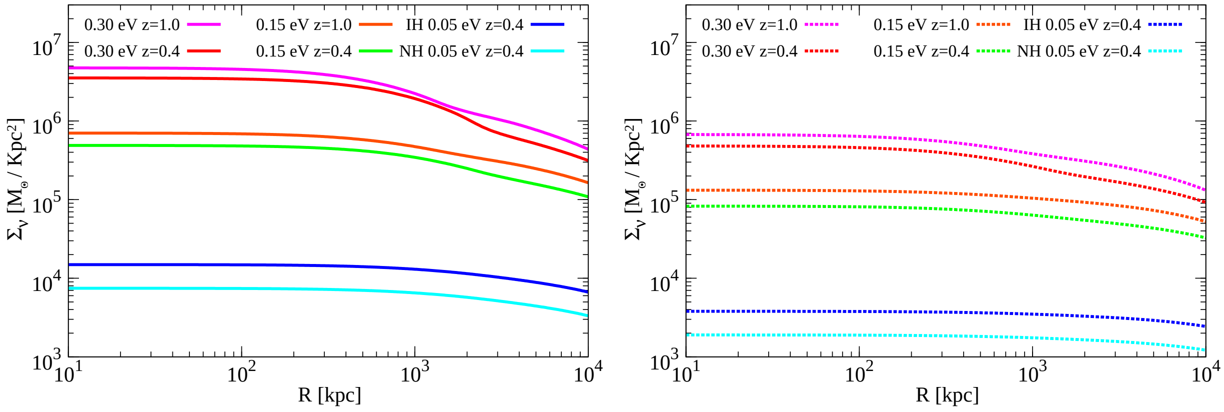

Figure 5.4: Neutrino surface over-density profiles for neutrinos with the indicated masses, at $z = 0.4$ and $z = 1$. Left panel is for halo mass $10^{15}\, h^{-1} M_\odot$, and right panel for $10^{14}\, h^{-1} M_\odot$.

a perfectly known selection function, with statistical errors declining as the square root of the number of clusters.

We summarize first the basic concepts of weak gravitational lensing. The distortion of images behind an extended gravitational lens is determined by the surface density of the lens at every point in projection on the sky, Σ. The convergence is $\kappa = \Sigma/\Sigma_{crit}$, where Σ_{crit} is the critical surface density, which depends on the angular diameter distances to the lens (D_l), to the source (D_s), and from the lens to the source (D_{ls}):

$$\Sigma_{crit} = \frac{c^2 D_s}{4\pi G D_{ls} D_l} \ . \tag{5.16}$$

In general, a spherical source acquires an elliptical shape after being lensed, with axis ratio $(1-\kappa-\gamma)/(1-\kappa+\gamma)$, where γ is the shear (for reviews see, e.g., [11, 77]). In a spherical lens, the shear is given by

$$\gamma(R) = \bar{\kappa}(R) - \kappa(R) \ , \tag{5.17}$$

where $\bar{\kappa}(R)$ is the average convergence within a projected radius R,

$$\bar{\kappa}(R) = \frac{2}{R^2}\int_0^R dR'\, R'\, \kappa(R') \ . \tag{5.18}$$

The weak lensing limit is the case when $\kappa \ll 1$ and $\gamma \ll 1$, in which case the ellipticity acquired by the source is $\epsilon \simeq 2\gamma$.

For an arbitrary mass distribution without spherical symmetry, we can choose any center we may wish and consider the values of the convergence and shear averaged on circles of radius R around the chosen center. The averaged quantity $\bar{\kappa}(R)$ is also obtained by averaging the convergence within a radius R. Equation (5.17) is then just as valid for an arbitrary mass distribution, provided that we define $\kappa(R)$ and $\gamma(R)$ by averaging over circles of radius R (or, in other words, circularly rotating the lens around the chosen center and averaging over all possible angles of rotation).

The quantity $\gamma(R)$ is the one we can directly measure from the shapes of the lensed galaxies, and the density profile of the cluster lens can be reconstructed by the use of inversion methods [44]. A very useful particular case is obtained by considering the integral

$$\int_{R_1}^{R_2} \frac{dR}{R} 2\gamma(R) = \bar{\kappa}(R_1) - \bar{\kappa}(R_2) \equiv C_{12} \ . \tag{5.19}$$

This equality is easily verified from equations (5.17) and (5.18). Hence, we can measure *differences* in the projected mass at two different radii R_1 and R_2, from the directly observable shear in the annulus between the two radii.

The shear cannot be measured exactly because the sources have random ellipticities with dispersion σ_e. If the sources have a number density n (considering them to be all at the same redshift for simplicity), the error in the measurement of the average γ in an annulus of radius R and width ΔR is

$$\sigma_\gamma = \frac{\sigma_e}{2}(2\pi R\, n\, \Delta R)^{-1/2} \ . \tag{5.20}$$

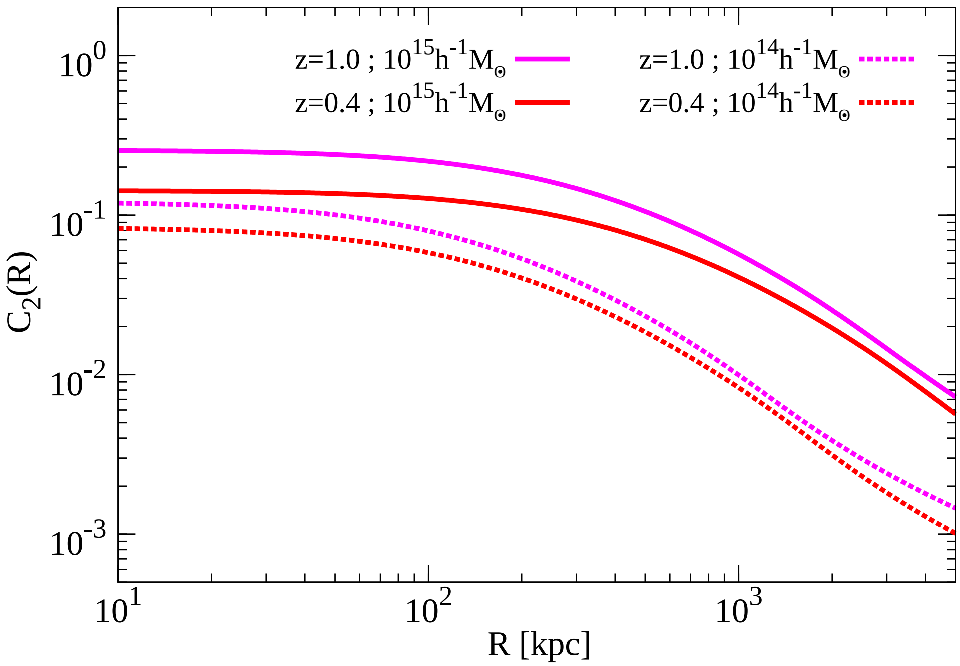

Figure 5.5: The function $C_f(R)$, with $f = 2$, for four dark matter halos with the masses and redshifts indicated.

The error in the quantity C_{12} is then given by

$$\sigma_C = \frac{\sigma_e}{2\sqrt{\pi n R_1^2}\sqrt{1 - R_1^2/R_2^2}} \; . \tag{5.21}$$

The mean value of C_{12} averaged over a large sample of clusters depends on the mass distribution of the clusters and any cosmological parameters that affect the average halo density profiles. Ideally, if a sample of clusters is selected in a perfectly controlled way, one can predict their mean density profile and the function C_{12}. The density profile is affected by neutrinos, and if all other physical factors and selection effects influencing the mean density profile are correctly known and taken into account, the presence of neutrinos may be detected from the observed shape of the cluster shear profile using weak lensing.

As a specific example, we consider the case $R_2 = fR_1$, where f is a constant that we fix to $f = 2$. In Figure 5.5, the function $C_f(R) \equiv \bar{\kappa}(R) - \bar{\kappa}(fR)$ is plotted for four cases, with cluster masses of $10^{15}\, h^{-1}M_\odot$ and $10^{14}\, h^{-1}M_\odot$ at $z = 0.4$, and masses $10^{15}h^{-1}M_\odot$ and $10^{14}\, h^{-1}M_\odot$ at $z = 1$. The sources are assumed to lie all at $z_s = 1.5$.

The effect of neutrinos is to modify the observable function $C_f(R)$ by a fractional amount $\Delta C_f/C_f$, where ΔC_f is calculated for the neutrino density profile in the same way as C_f for the total mass profile. This ratio is plotted in Figure 5.6 for various neutrino masses and for two different dark matter halo masses. The ratio increases with neutrino mass and

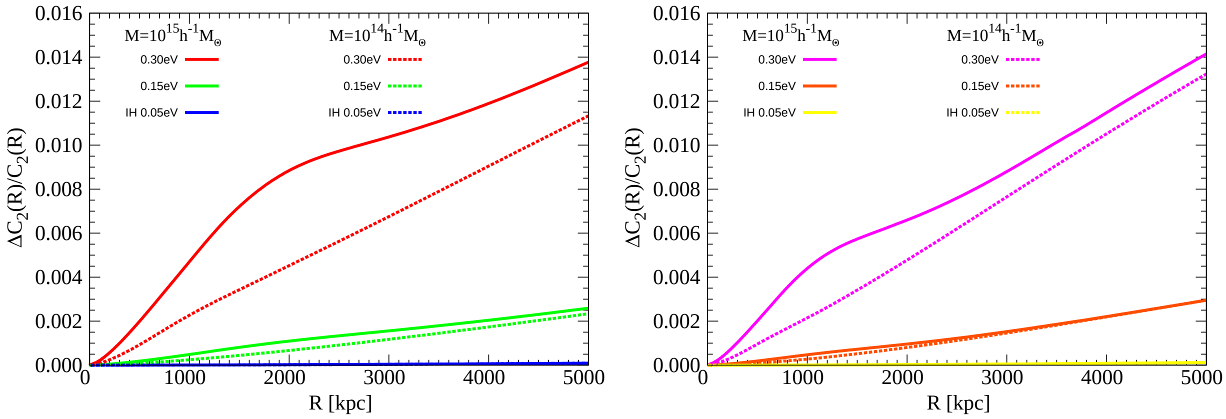

Figure 5.6: Fractional neutrino perturbation on the weak lensing profile, $\Delta C_f/C_f$, versus radius, for the cluster masses and neutrino masses indicated. The left panel is for clusters at $z = 0.4$, and the right panel at $z = 1$.

grows with radius because the neutrino density profile is extended. For the cases that are shown, the fractional weak lensing effect of neutrinos does not change much with halo mass, although the observable effect, ΔC_f, obviously increases with halo mass, as shown in Figure 5.7.

The predicted neutrino effect is very small, and it might only be observable as a perturbation in the mean cluster shear profile by averaging over many clusters. The requirement for detecting the neutrino effect can be estimated by considering the cluster in Figure 5.5 with a halo mass $10^{15}\,h^{-1}M_\odot$ at $z = 0.4$, and sources with number density $n = 30\,\mathrm{arcmin}^{-2}$ located at $z = 1.5$ and at the radius $r_1 = 2$ Mpc (corresponding to 6 arc minutes). The 1-σ error on C_f is $\sigma_C = 0.002$ if we use $\sigma_e = 0.2$, while its value is $C_f(r_1) \simeq 0.01$. Therefore, we may reach an accuracy of 20% on the measurement of C_f with a single cluster. To be able to measure the difference between different neutrino models of $\Delta C_f/C_f < 0.01$, as expected from Figure 5.6 for a neutrino mass of 0.3 eV, one would need to average the measurement of the shear over 10000 clusters to obtain a 5-σ result.

This is approximately the number of massive clusters that might be observed in an all-sky weak lensing survey of sufficient depth. Therefore, the measurement of the neutrino perturbation on the mean density profile of clusters is extremely difficult. Apart from the need to observe a very large number of clusters to reduce the statistical error, systematic uncertainties would in practice be even more difficult to resolve. The theoretical prediction for the precise density profile in the absence of neutrinos needs to be sufficiently reliable, but this profile is affected by several variables that may be hard to control: the precise selection function of clusters of different masses and different spatial orientations and projection effects would need to be accurately modeled using numerical simulations of structure formation, and the contribution from baryons would be subject to uncertainties related to radiative cooling, galactic winds, and generally the way that galaxy formation may alter the mass distribution.

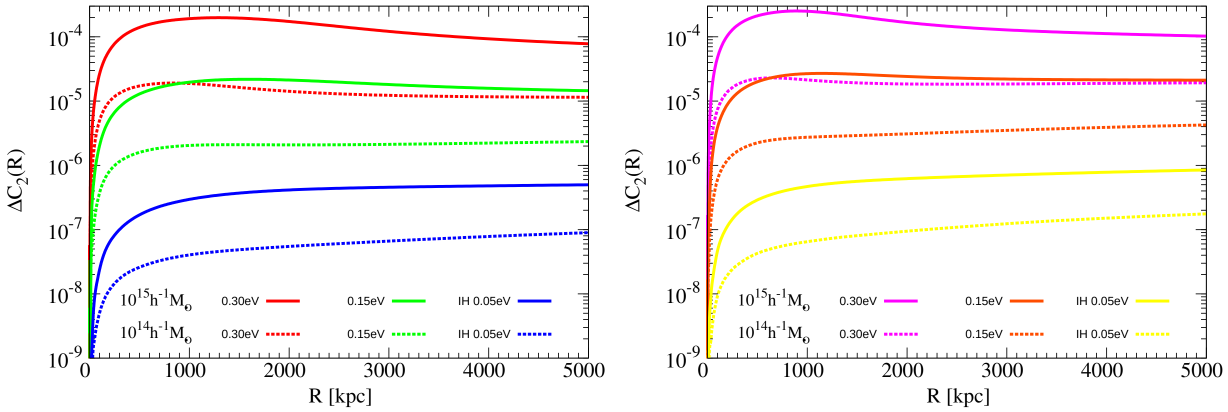

Figure 5.7: Neutrino perturbation on the weak lensing profile, ΔC_f, versus radius, for the same cluster and neutrino masses as in Figure 5.6. Left panel is for halos at $z = 0.4$ and right panel at $z = 1$.

The detection of the gravitational effect of neutrinos from lensing seems therefore a very difficult challenge.

The calculation presented in this paper should be considered only as an illustrative case. In practice, a better approach for attempting to measure the clustering effects of neutrinos may be to examine directly the power spectrum and bispectrum of the weak lensing shear over the whole field, thereby avoiding the issue of selection effects in a cluster sample. However, this would necessarily average out the effects of neutrinos in the regions where they are strongest, in massive clusters of galaxies. The cross-correlation of lensing shear with massive galaxies or diffuse X-ray emission that are associated with clusters would also likely be subject to similar uncertainties arising from the precise selection function.

5.5 Conclusion

We have presented the clustering of relic neutrinos around spherical dark matter for various illustrative cases. Neutrinos produce an extended distribution of mass with a large core determined by their primordial thermal velocities, which cause a perturbation on the total density profile. The non-linear collapse of neutrinos in massive clusters should modify their impact on the overall mass power spectrum of fluctuations calculated in the linear regime.

The presence of the neutrino perturbation in the average mass density profile of clusters of galaxies using weak gravitational lensing would constitute a remarkable astrophysical detection of the cosmic relic neutrinos, which cannot be detected by any other known method, except for their linear contribution to the total matter power spectrum. However, this measurement is a very difficult one owing to the small contribution that neutrinos make to the cluster mass even at very large radius. For a neutrino mass of 0.3 eV, the largest value that is compatible with current experimental constraints, the lensing shear profile of a massive cluster is affected by neutrinos roughly at the level of 1%. This small signal can only be detected by averaging lensing measurements over observable clusters in a large fraction of the sky. Although this observation can be done with an all-sky weak lensing space mission, such as the planned EUCLID mission, systematic uncertainties related to the impact of physical effects such as the distribution of baryons and the precise cluster selection function would make this detection a difficult one.

Chapter 6

Neutrino Signatures on the High Transmission Regions of the Lyman-α Forest

In this chapter we present the paper:

Neutrino Signatures on the High Transmission Regions of the Lyman-α Forest, Francisco Villaescusa-Navarro, Mark Vogelsberger, Matteo Viel & Abraham Loeb, 2011, arxiv: 1106.2543.

In this paper we find that the regions of low baryon density, or high transmission regions, are very sensitive to the masses of the neutrinos. Here we propose a method to measure the masses of the neutrinos by measuring the properties of the high transmission regions of the Lyman-α forest.

6.1 Introduction

Neutrino oscillation experiments revealed that neutrinos are not massless particles. Since then a major effort has been dedicated to measure or constrain neutrino masses. Current laboratory bounds constrain the electron neutrino mass to $m_{\nu_e} < 2.05$ eV [53, 48]. Cosmological bounds for the sum of all neutrino masses are still significantly stronger: constraints from WMAP7 alone yield $\Sigma_i m_{\nu_i} < 1.3$ eV [47], while combined with large scale structure (LSS) measurements they constraint the mass to $\Sigma_i m_{\nu_i} < 0.3$ eV [99, 89, 34, 73]. The tightest 2σ upper limit of $\Sigma_i m_{\nu_i} < 0.17$ eV, is obtained by combining cosmic microwave background (CMB) results, LSS and Lyman-α forest[79] data sets (see [1] for a summary of current and future neutrino mass constrains). Among all the different observables the Lyman-α forest is particularly constraining since it probes structures over a wide range of redshift, in a mildly non-linear regime and on small scales where the neutrino signature is present [51, 72, 62].

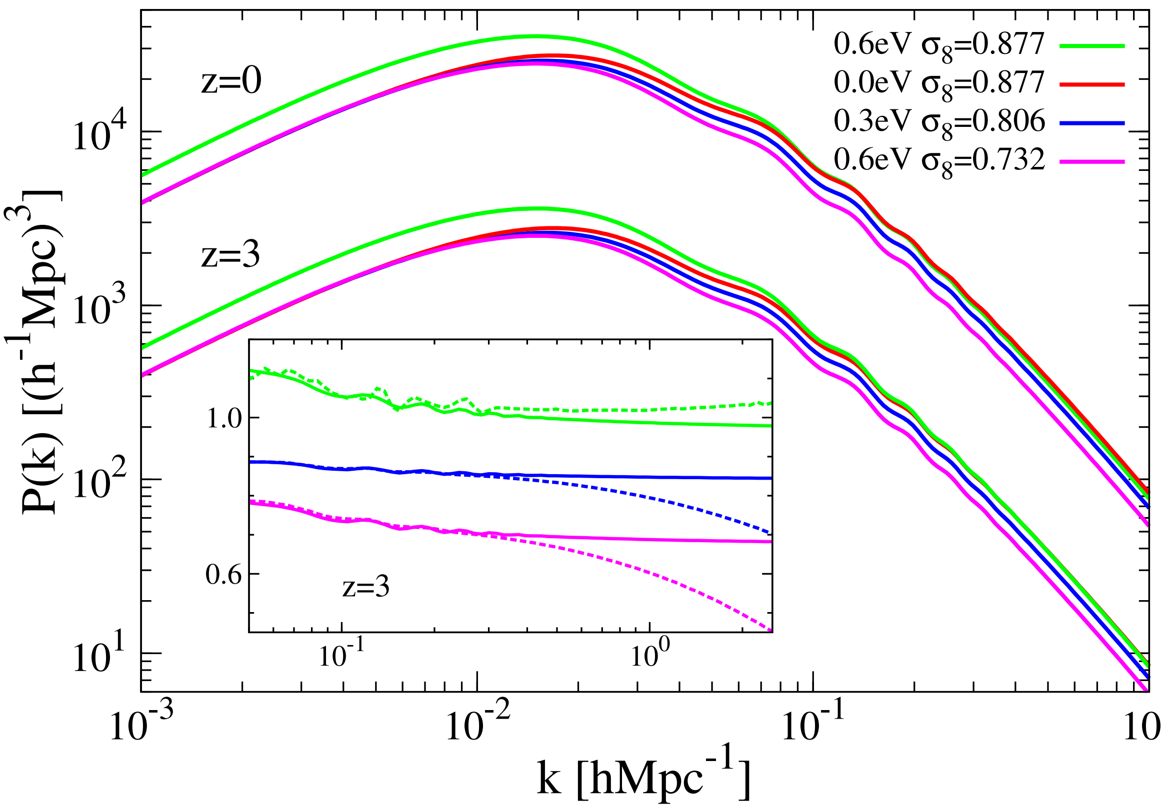

Figure 6.1: Linear power spectra for different neutrino masses at z = 0 (upper lines) and z = 3 (bottom lines). The inner panel shows the linear (solid lines) and non-linear (dotted lines) power spectrum at z=3 normalized to the case without neutrinos. On scales $k < 0.03$ h Mpc^{-1} changes in the non-linear power spectra are driven by the differences in the linear power spectra.

The dynamics of cosmological neutrinos is very different from that of the dominant cold dark matter (CDM) component. The large velocity dispersion of neutrinos suppresses their power spectrum of density fluctuations on small scales, making the shape of the total power spectrum a potential probe of neutrino masses.

Previous studies have addressed the role of neutrinos in dark matter halos [84, 75, 96], LSS [57, 14, 13, 15, 16, 61] and the intracluster medium [94], using both linear theory and N-body/hydrodynamic techniques for the non-linear regime. It has been shown that on scales of 1-10 h^{-1}Mpc the non-linear suppression is redshift and mass dependent in a way that is different from a naive extrapolation of linear theory.

In this *Letter* we study the effect of massive neutrinos on the properties of low density regions or *voids* in the intergalactic medium (IGM). Naturally, neutrinos have only a mild effect on dark matter halos [84, 75, 96], since their large velocity dispersion prevents their clustering on small scales. In contrast, we find that the impact of neutrinos on void properties is much stronger. Voids are relatively empty regions with $\delta = \rho_m/\bar{\rho}_m - 1$ ranging from almost -1 in their cores to ~ -0.7 at radii $10-20$ Mpc at $z=0$ [19]. By solving the dynamical equations for an isolated spherical top-hat underdense perturbation, we find that neutrinos modify the evolution of underdense regions by making them smaller and denser. Neutrinos contribute to the interior mass of the underdense region delaying the rate at which CDM is being evacuated from its interior and slowing down the velocity of the shell surrounding it. We find that the linearly extrapolated density contrast when the underdense region enters into its non-linear phase decreases by $\sim 10\%$ for neutrinos with $\Sigma_i m_{\nu_i} \sim 1$ eV. Using the analytic model presented in [80] we find that the statistics of voids depend on both σ_8 and $\Sigma_i m_{\nu_i}$. Lyman-α voids and their dependence on other cosmological parameters have been studied in [93]. Here we study the dependence of void properties on the sum of the neutrino masses. We focus our attention on the Lyman-α signature of low density regions, and introduce a new and simple statistical tool that samples most of the IGM volume and appears highly sensitive to neutrino masses.

6.2 Numerical Method

Our mock quasar spectra are based on cosmological simulations run with the TreePM-SPH code GADGET-3 [86]. The code has been extended to include neutrinos either by solving their potential on the mesh or by representing them as discrete particles [61]. Here, we use primarily the first implementation and refer the reader to [61, 14, 13] for a critical comparison of the two methods. Our simulations consist of 2×512^3 CDM plus gas particles sampling a periodic box of 512 h^{-1}Mpc. We adopt a flat ΛCDM background with cosmological parameters $\Omega_{\rm CDM} + \Omega_\nu = 0.25$, $\Omega_\Lambda = 0.7$, $\Omega_b = 0.05$, $h = 0.7$ and $n_{\rm s} = 1$. We consider three degenerates neutrino species with a total mass of $\Sigma_i m_{\nu_i} = 0.0, 0.3$ and 0.6 eV. The initial power spectra of most of our simulations, produced with CAMB[1], are normalized for all neutrino masses at a wavenumber $2 \times 10^{-3} h$ Mpc^{-1}, corresponding to the scale constrained by CMB data. This produces different values of $\sigma_8 = 0.877,\ 0.806$ and 0.732 at $z = 0$ for the models with $\Sigma_i m_{\nu_i} = 0.0,\ 0.3$ and 0.6 eV, respectively (see Fig. 6.1). Our initial conditions are generated at $z = 49$.

For each simulation we consider snapshots at redshifts $z = 2.2$ and $z = 4$ that bracket the range of interest for the observed Lyman-α forest in quasar spectra from ground-based telescopes. For each snapshot we sample 4500 random line of sights (RLOSs) uniformly distributed along each x, y or z direction. For each RLOS we extract the baryon density contrast $\rho_b(r)/\overline{\rho}_b$ and the peculiar velocity $V_p(r)$ along the line of sight and then compute the transmitted flux $e^{-\tau(u)}$ in redshift space (with u in km s^{-1}), where τ is the Lyman-α optical depth, by using the *Fluctuating Gunn Peterson Approximation*:

$$\tau(u) = A \int_{-\infty}^{+\infty} dx\ \delta[u - x - V_p(x)] \left(\frac{\rho_b(x)}{\overline{\rho}_b}\right)^{1.6}, \tag{6.1}$$

---

[1] `http://camb.info/`

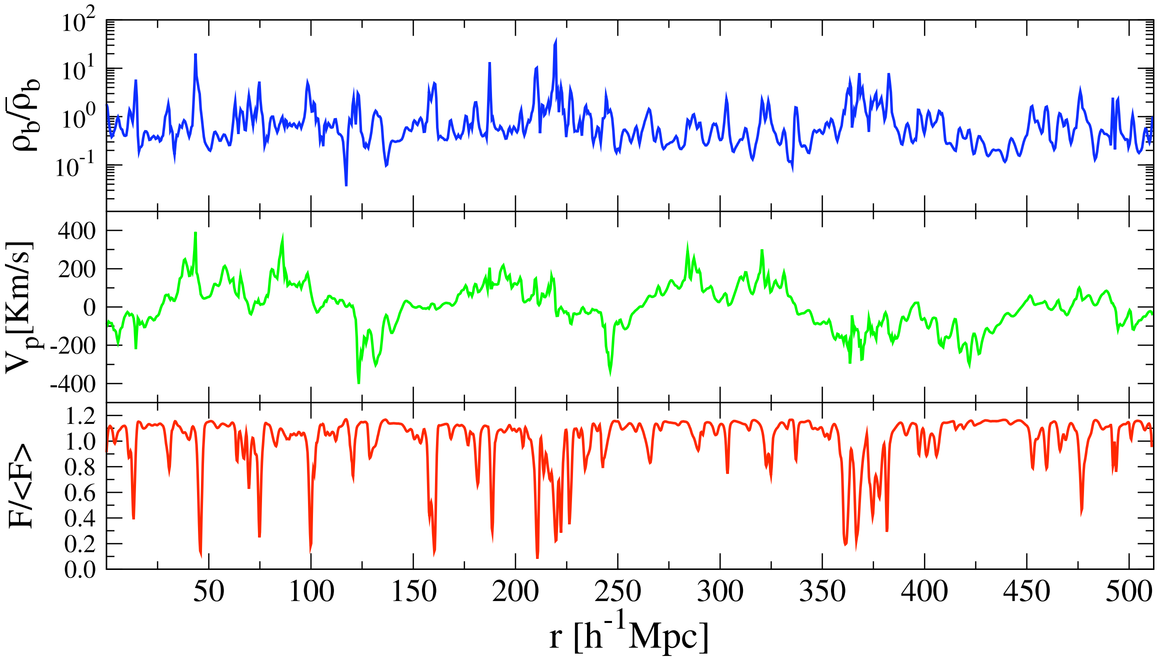

Figure 6.2: Real space distribution of the baryon density contrast, $\rho_b/\overline{\rho}_b$ (top panel), and the peculiar velocity, V_p (middle), along a random line-of-sight (RLOS). In the bottom panel we plot the transmitted flux $F = e^{-\tau}$, in units of the mean flux $\langle F \rangle$, in redshift space.

where $x = H(z)r/(1+z)$ is the redshift space coordinate and A is a factor that depends on the global thermal history of the IGM [23],

$$A = 0.433\left(\frac{1+z}{3.5}\right)^6\left(\frac{\Omega_b h^2}{0.02}\right)^2\left(\frac{0.65}{h}\right)\left(\frac{3.68H_0}{H(z)}\right)\times \left(\frac{1.5\times10^{-12}s^{-1}}{\Gamma_{HI}}\right)\left(\frac{6000K}{T_0}\right)^{0.7}, \quad (6.2)$$

with Γ_{HI} being the hydrogen photoionization rate. The power-law index in the scaling with $\rho_b/\overline{\rho}_b$ arises from the equation of state for the IGM temperature, $T = T_0(\rho_b/\overline{\rho}_b)^\alpha$ [42], with $\alpha \approx 0.6$. In all our calculations we adopt $T_0 = 10^4$K and choose Γ_{HI} such that the mean flux over the whole set of RLOS reproduce the observed mean flux at redshift z [64] $\langle F \rangle = e^{-\tau_{eff}(z)}$ with $\tau_{eff}(z) = 0.0023(1+z)^{3.65}$ [46]. We neglect effects of thermal broadening. Finally, we smooth the flux over a scale of 1 h^{-1}Mpc which is larger than the Jeans length to avoid sensitivity to substructure below the Jeans scale which is affected by numerical resolution and astrophysical processes (e.g. feedback from galactic winds).

Figure 6.2 shows the baryon density contrast, $\rho_b/\overline{\rho}_b$, and peculiar velocity, V_p, extracted along a RLOS as a function of the comoving coordinate r together with the corresponding transmitted flux $F = e^{-\tau}$ in redshift space, plotted in terms of the mean flux at redshift z.

6.3 Analysis of the simulations

We focus our analysis on the statistical properties of low density regions that produce weak absorption features. A region is a continuous domain in the transmitted flux profile which remains always above a given threshold. The higher the threshold, the lower the absorption in that region. For each RLOS we extract the transmitted flux from $\rho_b/\overline{\rho}_b$ and V_p and count the number of regions above the selected threshold. This results in a statistical estimate of the low absorption contribution to the Lyman-α signal, and allows us to quantify the impact of neutrinos on those regions.

In Fig. 6.3 we plot the probability distribution function (PDF) for the number of regions per path length of 100 h^{-1}Mpc[2] above a threshold of $F/\langle F\rangle = 1.14$ at redshift $z = 2.2$ (top) and at redshift $z = 4.0$ for a threshold $F/\langle F\rangle = 1.70$ (bottom) for three different neutrino masses, $\Sigma_i m_{\nu_i} = 0.0,\ 0.3,\ 0.6$ eV. We have verified that these PDFs do not change if we increase the number of RLOS, i.e. our statistical sample of RLOS is large enough to reliably measure the PDF. Figure 6.3 shows that the neutrino mass has a significant impact on the mean of the distributions. In Fig. 6.4 we plot the mean of the distributions, i.e. the average number of regions per path length of 100 h^{-1}Mpc above a given threshold, as a function of the threshold for the three different neutrino masses ($\Sigma_i m_{\nu_i} = 0.0,\ 0.3,\ 0.6$ eV) at redshift $z = 2.2$ (top) and $z = 4.0$ (bottom). This shows clearly that the higher the threshold, the larger are the differences between the various neutrino cosmologies. This is the expected neutrino signature as we discuss below.

σ_8-Ω_ν degeneracy. In order to investigate the degeneracy between σ_8 and Ω_ν we run one simulation with $\Sigma_i m_{\nu_i} = 0.6$ eV and the same $\sigma_8 = 0.877$ as the $\Sigma_i m_{\nu_i} = 0.0$ eV model. This mimics the case for which σ_8 is measured independently and one would like to constrain Ω_ν. We find that the PDF for the number of regions above a threshold of 1.14 at $z = 2.2$ is close to the one with $\Sigma_i m_{\nu_i} = 0.0$ eV (see Fig. 6.3), but not identical. Larger differences between these two models show up at $z = 4.0$ (see Fig. 6.4). Given that neutrinos affect the growth factor, we conclude that the degeneracy between σ_8 and Ω_ν can be broken by examining the redshift evolution of the PDFs.

6.4 Numerical convergence

We explicitly checked that relative differences between our neutrino models are numerically converged against mass and spatial resolution. Furthermore, we used the neutrino particle implementation and found the same trends in the neutrino signature as with the grid method, although relative differences between the different models are even slightly larger when we use the particle implementation. This is due to the fact that non-linear neutrino effects, such as phase mixing, are only captured properly by using the particle implementation. We note however that the grid implementation in the mildly non-linear Lyman-α regime

---

[2] Non-integer numbers are due to the path length normalization.

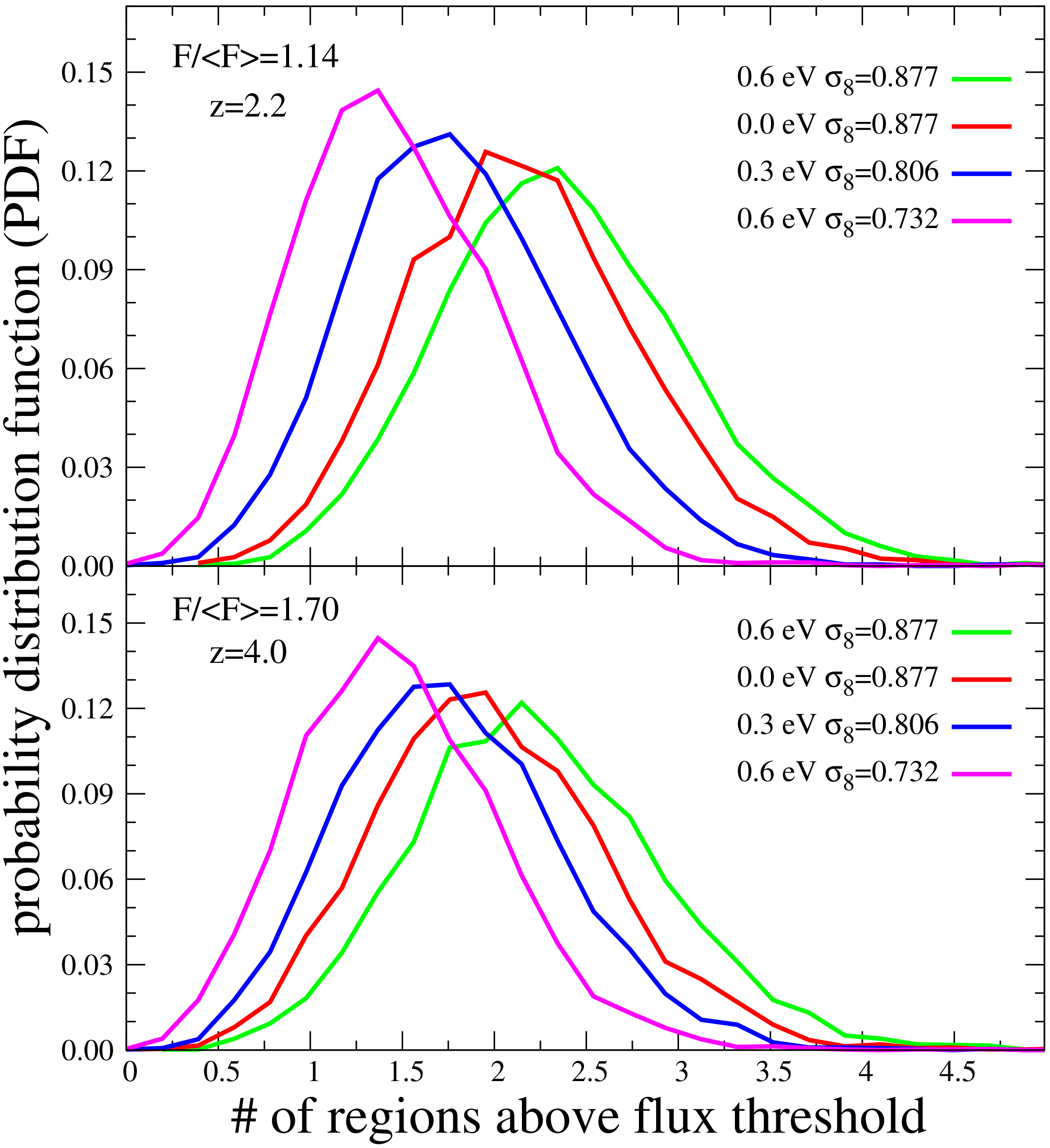

Figure 6.3: Probability distribution function (PDF) for the number of regions per path length of 100 h^{-1}Mpc above a threshold of $F/\langle F\rangle = 1.14$ (top), 1.70 (bottom) as a function of $\Sigma_i m_{\nu_i}$ and σ_8 at $z = 2.2$ (top) and $z = 4$ (bottom). The PDFs have long tails with a very low probability that extend up to 10-12. The $\sigma_8 - \Omega_\nu$ degeneracy is not perfect and can be broken by studying the spectra at different redshifts.

is fully justified since non-linear neutrinos effects should not be particularly important at those redshifts and at $k < 1\ h\ \mathrm{Mpc}^{-1}$.

6.5 Discussion and Conclusions

We have presented a novel and simple method to measure neutrino masses by studying the properties of low density regions in the Lyman-α forest of quasar spectra. Those regions correspond to the inner parts of non-linear voids. We find that the number of regions above a given threshold in the flux is strongly affected by neutrinos, especially once the amplitude of the matter power spectrum is fixed at large scales (i.e. normalized by the CMB anisotropies). The changes between different models are due to two factors: the change in amplitude and slope in the linear power spectrum driven by neutrinos and non-linear effects associated with CDM and neutrinos (note that neutrinos modify the non-linear evolution of the CDM distribution). The inner panel of Fig. 6.1 shows the linear (solid lines) and non-linear (dotted lines) versions of the power spectrum at $z = 3$ normalized to the case without neutrinos. Whereas the modification on large scales ($k < 0.03\ h\ \mathrm{Mpc}^{-1}$) is driven by the linear power spectrum, we find that on smaller spatial scales the non-linear effects dominate. We have also shown that the $\sigma_8 - \Omega_\nu$ degeneracy can be broken by studying the redshift evolution of low density regions in the Lyman-α forest flux.

Our method can be used to constrain neutrino masses by measuring the average number of regions as a function of threshold. In the subplot of Fig. 6.4 we show the average number of regions per path length of 100 h^{-1}Mpc as a function of the threshold at $z = 2.2$ normalized to the neutrinoless model. The black error bars show the 90% (interior tick marks) and 99% (exterior tick marks) confident intervals for a mock catalog consisting of 200 RLOS taken from the simulation with ($\Sigma_i m_{\nu_i} = 0.0$ eV, $\sigma_8 = 0.877$). We find that with a catalog consisting of 200 RLOS we can rule out models ($\Sigma_i m_{\nu_i} = 0.3$ eV, $\sigma_8 = 0.806$) and ($\Sigma_i m_{\nu_i} = 0.6$ eV, $\sigma_8 = 0.732$) with a high significance. The best way to distinguish models with the same σ_8 would be by adding more quasar spectra and combining results at different redshifts. Although regions at high transmissivity are prone to systematic errors (such as the continuum fitting procedure which provides the main systematic uncertainty in calibrating the flux at weak absorption levels), we believe that statistics of large-scale voids such as the one presented here could be important for upcoming and present spectroscopic surveys of quasars (e.g. [85]). Variations in the thermal and ionization histories of the IGM are expected to impact on the Lyman-α properties of large size voids [93] and the neutrino signatures should be seeked by marginalizing over all the other relevant parameters. However, the generic redshift evolution and threshold (scale) dependence of the neutrino effects can be used to separate them from the redshift evolution of the IGM properties. Independent constraints on thermal evolution obtained by different techniques and data sets can be put as priors in the analysis performed.

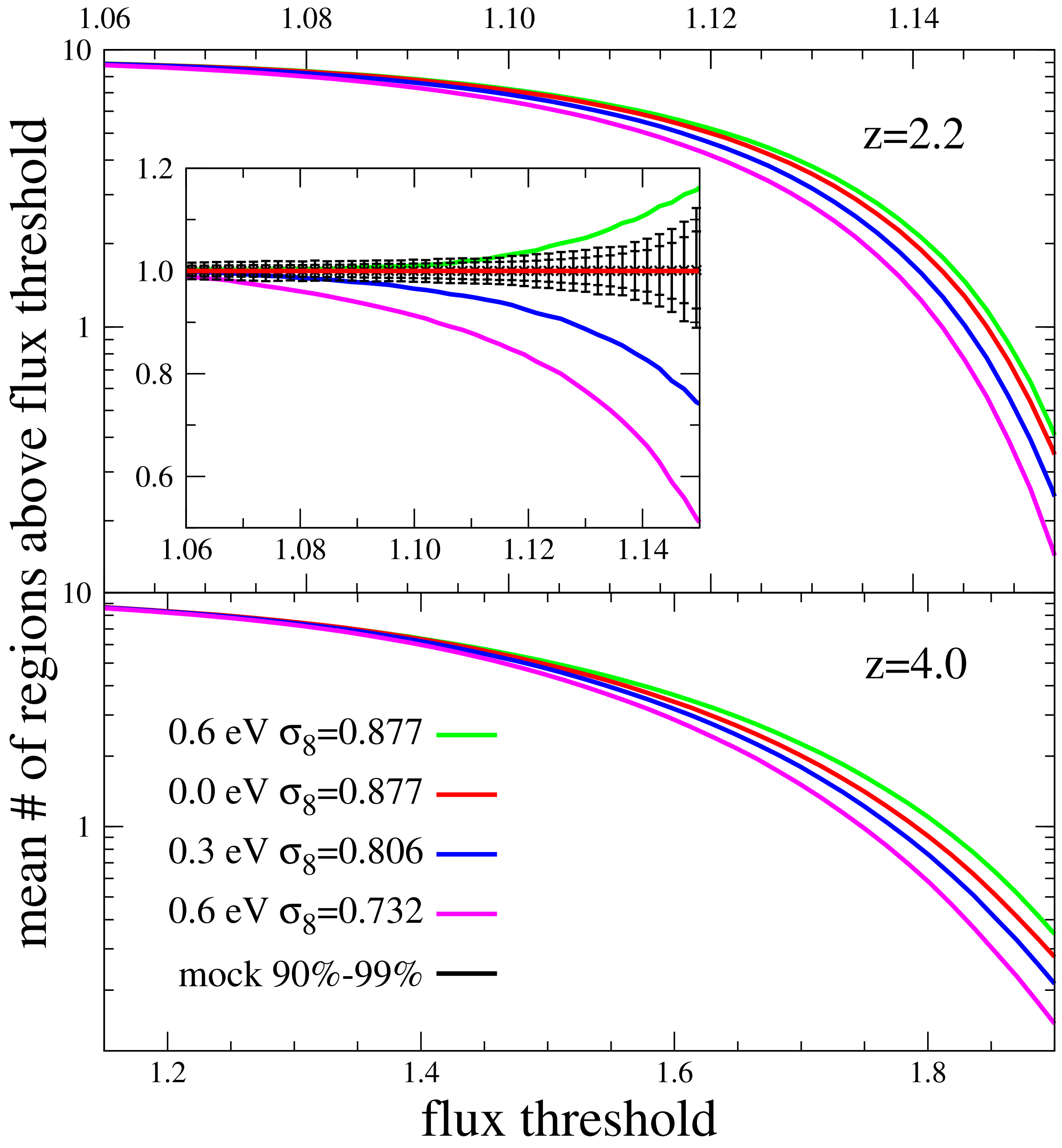

Figure 6.4: Average number of regions per path length of 100 h^{-1}Mpc as a function of flux threshold at redshift $z = 2.2$ (top) and $z = 4$ (bottom) for different neutrino masses and σ_8. The subplot in the upper panel shows the ratio between models with $\Sigma_i m_{\nu_i} \neq 0.0$ and the model with $\Sigma_i m_{\nu_i} = 0.0$. The black error bars indicate the 90% (interior tick marks) and 99% (exterior tick marks) confident intervals for a mock catalog consisting of 200 RLOS taken from the simulation with ($\Sigma_i m_{\nu_i} = 0.0$ eV, $\sigma_8 = 0.877$). Models with $\Sigma_i m_{\nu_i} = 0.3, 0.6$ and $\sigma_8 = 0.806, 0.732$ respectively can be ruled out with a high significance by using a catalog of 200 QSO spectra.

Part III

Summary and Conclusions

Chapter 7

Summary and Conclusions

This thesis has been motivated by the necessity of studying the impact on the large scale structure of the universe by a dominant (warm dark matter), or subdominant (relic neutrinos) non-cold component of the dark matter. On one side, we have given an answer to the question whether warm dark matter can solve or alleviate the cusp/core problem, and on the other side, by studying the impact of relic neutrinos on non-lineal structures such as galaxy clusters or cosmological voids, we have searched for new cosmological observables that would be sensitive to the masses of the neutrinos.

Warm dark matter arises as a possible solution to several problems related with cold dark matter: the observed core in the dark matter density profile of low surface brightness (LSB) galaxies and the number of dark matter halos surrounding Milky Way size galaxies. N-body simulations with cold dark matter show that the density profiles of dark matter halos are well described by the Navarro-Frenk-White (NFW) profile. This profile presents a cusp at the halo center because the dark matter density grows as $1/r$ towards the center. In contrast, the dark matter density profiles of some galaxies, such as those found in low surface brightness galaxies, seem to present a core instead of a cusp. Warm dark matter, constituted by particles with non-negligible thermal velocities, is expected, due to the Tremaine-Gunn bound, to cluster in halos presenting a core in their density profile. In order to preserve the bottom-up structure formation process, we have considered in this thesis a generic type of warm dark matter made up of particles with thermal velocities such as their free-streaming is ~ 100 kpc/h. Given that the resolution of current N-body simulations[1] is not large enough to resolve the sizes of the cores found in LSB galaxies, we have used instead a method to compute warm dark matter halo density profiles which are consistent with the velocity dispersion of their particles. We have also investigated the dependence of our results with the warm dark matter halo formation time, with its mass and with the warm dark matter temperature (i.e. with the free-streaming of the warm dark matter). Our results indicate that warm dark matter produces indeed cores in the halo density profiles, but those cores are not large enough to reproduce the observed ones in LSB galaxies. We find that, in contrast

---

[1] Note that this thesis has been written on december 2011

to the typical core size observed in the density profiles of LSB galaxies, $r_{core}/r_{200} \approx 0.05$, warm dark matter can only, at most, produce cores fifty times smaller $r_{core}/r_{200} \approx 10^{-3}$. We conclude that the solution to the cusp/core puzzle should arrive from astrophysics, from supernova explosions for instance, rather than from the nature of the dark matter.

Neutrinos are one of the most mysterious particles in nature and from the discovery of the neutrino oscillations we know that they have mass. The Big Bang theory predicts the existence of a cosmic neutrino background with a current temperature close to 2 K. Even though at that temperature neutrinos are non-relativistic, they still have pretty large thermal velocities. For that reason, neutrinos are commonly considered as hot dark matter. In a universe dominated by hot dark matter, the structure formation process would be up-bottom, in contrary to what it is observed. Therefore, relic neutrinos can not be the dominant component of the dark matter. On the other hand, due to the fact that they have mass, they constitute a subdominant hot component of the dark matter. Trying to answer one of the most important questions in physics, What are the masses of the neutrinos?, we have studied in this thesis the impact of the relic neutrinos on non-lineal structures, searching new cosmological observables that would be sensitive to the masses of the neutrinos.

Relic neutrinos have a mean velocity approximately equal to $150(1+z)(eV/m_\nu)$ km/s. Therefore, their velocity is small enough to allow them to cluster within gravitational potentials deep enough as those present in galaxies or clusters of galaxies. In this thesis we have studied the formation of halos of neutrinos in clusters of galaxies and how their presence could be detected using weak lensing. We find that, as expected, these halos of neutrinos present three big differences with respect to their dark matter cousins: neutrino halos have much larger sizes than dark matter halos, their density contrast is much smaller and they present a large core in its density profile. Those features are just a consequence of the neutrino thermal velocities (which depend exclusively on the neutrino masses); the smaller they are, the closer neutrino halos are to dark matter halos. These halos of neutrinos contribute to the total mass of the dark matter halo and this contribution can be measured using weak lensing. The shape of an object situated behind an extended gravitational lens is being modified by the deflection of its light rays through the lens. That distortion depends on the projected mass profile of the lens. Since neutrino halos modify the density profiles of galaxy clusters (i.e. the projected mass profile of the lens), adding a contribution to their total masses, neutrino masses could be constrained using a catalog of weak lensed objects. We have computed the perturbation produced by relic neutrinos on the shape of lensed objects, and we find that the value of this perturbation, at the virial radius for 3 degenerate neutrinos of masses 0.3 eV each one, is approximately equal to 1%. We find smaller perturbations for smaller neutrino masses and/or smaller radii. The method proposed in this thesis is able to measure these neutrino effects on the galaxy clusters, i.e. to put constrains on the neutrino masses, if other effects that also affect the properties of lensed objects are well controlled. Because those effects, such as the selection function or the distribution of baryons, are very hard to control, the detection of the cosmic neutrinos by weak lensing is challenging.

In this thesis we have also investigated the impact of relic neutrinos on cosmological voids. Cosmological voids are regions of the universe, with densities below the mean of the universe, where the dark matter is being evacuated to its outskirts at a speed larger than the Hubble flow. Neglecting effects such as tidal forces or substructure, the evacuation rate at a certain distance from the center of the void is controlled by the mass of the void contained within a sphere of that radius. Therefore, the emptier a void is, the larger its evacuation rate is. Given that relic neutrinos have pretty large thermal velocities, they will not be as sensitive to the dynamics associated with voids as the rest of the dark matter. Therefore, it is expected that while the cold dark matter feels the dynamics of the void and evacuate it, emptying even more the void, the relic neutrinos would remain within the void, adding a contribution to its mass and thus, delaying the process of dark matter evacuation. Using the spherical collapse model, we have found that neutrinos have indeed a pretty large impact on the properties of the cosmological voids. We find that neutrinos delay both, the void formation time and the dark matter evacuation rate. In a universe with massive neutrinos, voids would be smaller, denser and less evolved than their equivalents in a massless neutrino universe.

In order to fully study the impact of neutrinos masses on the properties of cosmological voids (taking into account all effects affecting the void dynamics such as tidal forces and substructure), we have run N-body simulations with cold dark matter, baryons and massive neutrinos and we have compared the results with those obtained by running N-body simulations with cold dark matter, baryons and massless neutrinos. We find that the results are in agreement with what we expected, i.e. we find that voids are smaller, denser and less evolved in a universe with massive neutrinos than in one with massless neutrinos. We have searched for a new cosmological observable that would be sensitive to void properties and that could be used to put constrains on the neutrino masses. We have found this observable by studying the properties of the high transmission regions in the Lyman-α forest of QSO spectra. Our results indicate that, for a set of QSO spectra, the mean number of coherent regions above a given threshold in the transmitted flux spectra is strongly affected by Ω_ν. Using the Fisher matrix formalism, we find that with a set of ~ 400 high resolution QSO spectra, we could put constrains on the masses of the neutrinos of about $\Sigma_i m_{\nu_i} < 0.35$ eV, making this method one of the most promising observables to place tight constrains on the neutrino masses.

We can summarize the main conclusions and achievements of this thesis as follow:

- Warm dark matter can not solve the cusp/core problem.
- Halos of neutrinos are formed in the largest bound structures of the universe. Those halos of neutrinos modify the density profile of the host dark matter halo and this perturbation can be observed using weak lensing, although their detection is challenging.
- Relic neutrinos play an important role in the properties of the cosmological voids. A tight constraint on Ω_ν can be placed using a set of few hundred high resolution QSO spectra, and computing the mean number of coherent regions above a threshold in the transmitted flux spectra as a function of the threshold.

Part IV

Appendices

Appendix A

Publications

During the time this thesis was developed, the following papers were published:

F. Villaescusa-Navarro, N. Dalal, 2011, JCAP, 03, 24

F. Villaescusa-Navarro, J. Miralda-Escudé, C. Peña-Garay, V. Quilis, 2011, JCAP, 06, 27

F. Villaescusa-Navarro, M. Vogelsberger, M. Viel, A. Loeb, arxiv:1106.2543, submitted

Another paper, which is not directly related with the topic of this thesis was also published:

O. Mena, S. Razzaque, F. Villaescusa-Navarro, 2011, JCAP, 02, 30

Appendix B

Introducción, resumen y conclusiones en castellano

B.1 Introducción y motivaciones

Numerosas observaciones apuntan hacia la existencia de una componente de materia no barionica en el universo, que hoy conocemos bajo el nombre de materia oscura. Décadas atrás se especulaba con la posibilidad de que los neutrinos fueran los constituyentes de la misma. La hipótesis de que la materia oscura fuera caliente, expresión usada cuando la materia oscura esta compuesta de partículas de velocidades elevadas, fue rápidamente excluida ya que bajo tal circunstancia las primeras estructuras que se formarían en el universo tendrían tamaños colosales. Objetos de menor tamaño tales como galaxias, estrellas, planetas...etc, solo podrían formarse por fragmentación de las primeras estructuras gigantes. El hecho de no observar tales estructuras unido al enorme número de estructuras de pequeño tamaño observadas, ha permitido excluir de forma definitiva la hipótesis de que los neutrinos fueran el componente único o principal de la materia oscura.

Recientemente, el descubrimiento del cambio de sabor en diversas fuentes de neutrinos, conocidas como oscilaciones de neutrinos, han demostrado que los neutrinos tienen masa y por lo tanto, constituyen una fracción de la materia oscura. Aunque su proporción en el conjunto de toda la materia oscura sea pequeña, los neutrinos se comportan de manera diametralmente opuesta al resto. Las altas velocidades térmicas de los neutrinos cosmológicos afectan, entre otros, al proceso de formación de estructuras, retrasando la formación y evolución de las mismas. Si bien el efecto de los neutrinos en el régimen lineal ha sido estudiado y entendido correctamente, el impacto de estos en el régimen no-lineal no ha sido investigado en detalle. En la era de precisión cosmológica en la que estamos entrando, resulta imperativo entender correctamente los efectos que cada componente energética produce, por lo que es necesario estudiar y cuantificar los efectos generados por los neutrinos para la correcta estimación de los otros parámetros cosmológicos. En esta tesis, todos los cálculos se han realizado en el régimen no-lineal, comparando los resultados con los obtenidos en el régimen lineal cuando se consideró oportuno.

Una de las cuestiones actuales más importantes en física es ¿cuál es la masa de los neutrinos? En esta tesis se han buscado observables cosmológicos, fuera del régimen lineal, que sean sensibles a la masa de los neutrinos. Por una parte se ha estudiado la posible detección, usando lentes gravitatorias, de halos de neutrinos que se forman en las mayores estructuras gravitatorias del universo, los grupos de galaxias. Por otra parte se ha estudiado la manera en que la masa de los neutrinos modifican la forma, tamaño y evolución de los agujeros cosmológicos. Para la identificación observacional de este efecto, se han estudiado las señales que los neutrinos producen en las regiones de alta transmisividad de los espectros de objetos quasi-estelares.

Descartada la posibilidad de que la materia oscura sea caliente, el modelo cosmológico estandar asume que la materia oscura es fría. A lo largo de los años este modelo ha salido exitoso de los numerosos tests realizados y hoy en día es el modelo cosmológico más aceptado por la comunidad científica. Sin embargo, tiene varios serios problemas que el modelo debe de solucionar para preservar su validez.

Las simulaciones cosmológicas de N-cuerpos se utilizan como laboratorio en donde se crean universos virtuales y se estudian sus propiedades, evolución...etc. Las simulaciones cosmológicas con el modelo estándar predicen que los perfiles de densidad de materia oscura en galaxias, grupos de galaxias...etc corresponden a los de Navarro-Frenk-White (NFW). En estos perfiles, la densidad de materia oscura se aproxima al centro del halo como $\sim 1/r$. Sin embargo, hay ciertos tipos de galaxias en donde la densidad de materia oscura no crece en el centro, sino que permanece constante, formando lo que se conoce como un núcleo en el perfil de densidad. Otro problema del modelo estándar cosmológico radica en el número de halos que rodean galaxias como la vía láctea. Las simulaciones cosmológicas predicen un número mucho mayor al encontrado en las observaciones.

En la actualidad se está llevando a cabo un gran esfuerzo teórico y observacional con el fin de conciliar las simulaciones con las observaciones. Una de las posibles soluciones a ambos problemas consiste en asumir que la materia oscura no es fría sino templada, y por lo tanto, considerar que la materia oscura esta formada por partículas con velocidades no despreciables, pero que no son relativistas. Bajo esta hipótesis, el número de halos en la vecindad de una galaxia como la vía láctea se vería reducido al tiempo que al tener las partículas una velocidad mayor, los perfiles de materia oscura estarían obligados a presentar un núcleo en el perfil de densidad.

Las simulaciones cosmológicas de N-cuerpos realizadas hasta el momento, septiembre de 2011, no tienen resolución suficiente como para responder a la pregunta de si la materia oscura templada puede producir los núcleos de los perfiles de densidad de materia oscura observados en ciertas galaxias. En esta tesis, en colaboración con el Dr. Neal Dalal, hemos dado respuesta a la pregunta de si la materia oscura templada puede producir perfiles de densidad de materia oscura que estén en consonancia con los observados.

La tesis esta organizada en 5 bloques: introducción teórica, investigación científica, conclusiones, apéndices y bibliografía.

En el bloque 1, introdución teórica, se describen elementos básicos en cosmología, se presenta la materia oscura y se exponen las propiedades de los neutrinos así como el impacto, en el régimen lineal, de estos en cosmología. Este bloque consta de 3 capítulos.

En el capítulo 1, modelo cosmológico ΛCDM, se presenta el modelo cosmológico estándar, las bases teóricas y los observables que dan validez a este modelo.

En el capítulo 2, materia oscura, se muestra la evidencia experimental que sustenta la existencia de la materia oscura, los posibles candidatos y se describe brevemente las simulaciones cosmológicas de *N-cuerpos* con materia oscura.

En el capítulo 3, neutrinos cosmológicos, se exponen las propiedades fundamentales de estas partículas y se describen el fondo de neutrinos cosmológicos que predice el modelo cosmológico estándar. Se describen los principales efectos que estos neutrinos inducen en cosmología.

En el bloque 2, investigación científica, se presenta el trabajo científico realizado en esta tesis. Este bloque esta compuesto por 3 capítulos, correspondiendo cada uno de ellos a una publicación científica.

En el capítulo 4, picos y núcleos en cosmologías de materia oscura templada, se responde a la pregunta acerca de si la materia oscura templada puede producir los perfiles de densidad de materia oscura observados en cierto tipo de galaxias.

En el capítulo 5, halos de neutrinos en grupos de galaxias y su detección mediate métodos de lente débil, se presenta un estudio detallado acerca de la formación de halos de neutrinos en los potenciales gravitatorios creados por los grupos de galaxias y de como estos podrían ser detectados utilizando el efecto de lente gravitatoria.

En el capítulo 6, señales de neutrinos en las regiones de alta transmisividad del bosque de lyman-α, se presenta un nuevo observable cosmológico, el cual demuestra ser muy sensible a la masa del neutrino. Se muestra cómo las zonas de baja densidad bariónica, y por ende, de baja densidad en materia oscura, son regiones muy sensibles a la masa de los neutrinos cósmicos. Se describe a su vez una metodología con la cual se podría medir la masa de los neutrinos utilizando un conjunto de espectro de objetos quasi-estelares.

En el bloque 3, conclusiones, mostramos los principales logros conseguidos en esta tesis y describimos los planes futuros de investigación en el campo. En el bloque 4 presentamos un resumen de la tesis en castellano y un apéndice que completa el capítulo 6. Finálmente, en el bloque 5 mostramos la bibliografía.

B.2 El modelo cosmológico estándar

En esta sección se muestra el modelo cosmológico estándar. La sección esta dividida en dos grandes subsecciones: el modelo cosmológico en sí mismo, donde exponemos el modelo, los conceptos básicos, las ecuaciones más importantes que usaremos en el resto de la tesis y una breve descripción de los principales métodos que se usan para calcular el valor de los parámetros cosmológicos.

B.2.1 Modelo teórico

En esta subsección revisamos los principios de la teoría de la relatividad general y de la cosmología y mostramos las ecuaciones de Einstein y Friedmann. También presentamos una descricción, en términos de la relatividad general, del concepto de fluido ideal en cosmología. Finalmente introducimos algunos de los parámetros que aparecen en el modelo cosmológico estándar y describimos algunos conceptos básicos como el del *redshift*.

Pilares de la cosmología

Uno de los pilares de la cosmología es el llamado principio cosmológico. Este afirma que el universo es homogéneo e isótropo en grandes escalas. Este principio ha sido comprobado por observaciones [88][20], las cuales muestran que en escalas mayores a ~ 100 Mpc, el universo parece el mismo en todas direcciones. En escalas más pequeñas, el universo es altamente no homogeneo. Una prueba de esto es el hecho que observemos planetas, estrellas, galaxias, grupos de galaxias y agujeros cosmológicos.

Otro pilar de la cosmología moderna es la teoría de la relatividad general, que a día de hoy es la teoría de gravedad más exitosa. Formulada por Albert Einstein en 1916 [25], es la teoría estándar usada para describir la fuerza gravitatoria. Einstein construyó su teoría bajo los siguientes supuestos:

- La velocidad de la luz en el vacío como un invariante en cualquier sistema de referencia
- El principio de equivalencia[1]

En relatividad general, la geometría y estructura causal del universo puede ser descrita por una variedad cuatridimensional.

$$ds^2 = g_{\mu\nu} dx^\mu dx^\nu \ , \tag{B.1}$$

donde $g_{\mu\nu}$ es un tensor simétrico 4×4 llamado la métrica y dx^μ es un cuadrivector. ds es la distancia propia entre dos eventos x^μ y $x^\mu + dx^\mu$.

En relatividad general, los objectos se mueven a lo largo de geodésicas en el espacio-tiempo cuadridimensional descrito por la métrica B.1. Las ecuaciones de movimiento de una partícula de prueba[2] vienen dadas por

---

[1] El principio de equivalencia establece que en cualquier campo gravitatorio, siempre existe un sistema de referencia en el cual los efectos de gravedad están ausentes.

[2] Por partícula de prueba nos referimos a una partícula con una masa muy pequeña o nula, de forma que la geometría del universo no se vea afectada por la propia presencia de la partícula.

$$\frac{d^2x^\mu}{d\lambda^2} + \Gamma^\mu_{\nu\gamma}\frac{dx^\nu}{d\lambda}\frac{dx^\gamma}{d\lambda} = 0 \ , \tag{B.2}$$

donde λ es una variable usada para parametrizar la trajectoria $x^\mu = x^\mu(\lambda)$. $\Gamma^\mu_{\nu\gamma}$ es la conexión afín (también conocida como los símbolos de Christoffel)

$$\Gamma^\mu_{\nu\gamma} = \frac{1}{2}g^{\mu\sigma}\left[\frac{\partial g_{\sigma\nu}}{\partial x^\gamma} + \frac{\partial g_{\sigma\gamma}}{\partial x^\nu} - \frac{\partial g_{\nu\gamma}}{\partial x^\sigma}\right] \ , \tag{B.3}$$

donde el tensor $g^{\mu\sigma}$ satisface la relación $g^{\alpha\beta}g_{\beta\gamma} = \delta^\alpha_\gamma$, con δ^α_γ siendo:

$$\delta^\alpha_\gamma = \left\{ \begin{array}{ll} 1, & si\ (\alpha = \gamma) \\ 0, & si\ (\alpha \neq \gamma) \end{array} \right. \ . \tag{B.4}$$

Métrica de FRW

Se puede demostrar que la métrica más general de un universo en el cual se cumple el principio cosmológico (es decir, un universo homogéneo e isótropo) viene dado por la métrica de Friedmann-Roberson-Walker (véase por ejemplo [103] para una derivación detallada)

$$ds^2 = c^2dt^2 - a^2(t)\left[\frac{dr^2}{1-Kr^2} + r^2\big(d\theta^2 + sin^2\theta d\phi^2\big)\right] \ , \tag{B.5}$$

donde t es el tiempo propio, $a(t)$ es una función que contiene la evolución temporal del universo y que se denomina el factor de expasión y r, θ and ϕ son las coordenadas esféricas espaciales. K es un parámetro que toma valores iguales a 1, 0 ó -1 dependiendo de si el universo es cerrado, plano o abierto respectívamente.

Para el resto de la tesis, usaremos la métrica B.5 para un universo plano ($K = 0$). Aún a pesar de que esta métrica no describe adecuadamente la geometría del espacio-tiempo en la vecindad de planetas, estrellas o galaxias, describe muy bien al universo a primer orden, es decir, al universo en escalas mayores a ~ 100 Mpc.

Fluido ideal

Toda la información sobre la densidad y el flujo de energía y momento en el espacio-tiempo esta contenida dentro del tensor de energía-momento $T^{\mu\nu}$. En relatividad general, la ley de conservación de este objecto viene dada por

$$T^{\mu\nu}_{;\nu} = \frac{\partial T^{\mu\nu}}{\partial x^\nu} + \Gamma^\mu_{\gamma\nu}T^{\gamma\nu} + \Gamma^\nu_{\gamma\nu}T^{\mu\gamma} = 0 \ . \tag{B.6}$$

Esta ecuación representa la versión relativista de las leyes clásicas de conservación de energía y momento.

El universo se modela a menudo como un fluido perfecto. Un fluido perfecto se define como un medio en el cual, en cualquier punto, existe un sistema de referencia inercial, que se mueve con el fluido, en el cual el fluido parece isótropo. Bajo ese sistema de referencia, el tensor energía-momento adquiere la forma:

$$T^{\mu\nu} = \begin{pmatrix} \rho & 0 & 0 & 0 \\ 0 & p & 0 & 0 \\ 0 & 0 & p & 0 \\ 0 & 0 & 0 & p \end{pmatrix}$$

donde ρ y p son la densidad y presión respectivamente. La expresión covariante (válida bajo cualquier sistema de coordenadas) de un fluido perfecto es

$$T^{\mu\nu} = pg^{\mu\nu} + (p+\rho)u^\mu u^\nu \ . \tag{B.7}$$

u^μ se comporta como un cuadrivector bajo transformaciones generales de coordenadas satisfaciendo $u^0 = 1$, $u^i = 0$ en un sistema de referencia inercial. El cuadrivector esta normalizado de forma que cumple $g_{\alpha\beta}u^\alpha u^\beta = -1$.

Las ecuaciones de Einstein

Intentando formular las ecuaciones que gobiernan gravedad, Einstein sabía que esas ecuaciones tenían que estar escritas en forma covariante y que para campos gravitarios débiles y que cambian lentamente, tenían que reproducir la ecuación de Poisson

$$\bigtriangledown^2 \phi = 4\pi G T^{00}. \tag{B.8}$$

Einstein además impuso que el orden de la derivadas presentes en las ecuaciones no debería de ser mayor que 2 (recuerdese que las ecuaciones de Newton tienen derivadas de segundo orden como máximo). La única ecuación que satisface las tres anteriores condiciones viene dada por

$$R_{\mu\nu} - \frac{1}{2} g_{\mu\nu} R = -8\pi G T_{\mu\nu}, \tag{B.9}$$

donde $T_{\mu\nu} = g_{\mu\alpha} g_{\nu\beta} T^{\alpha\beta}$, $R_{\mu\nu}$ es el tensor de Ricci

$$R_{\mu\nu} = \frac{\partial \Gamma^\gamma_{\mu\gamma}}{\partial x^\nu} - \frac{\partial \Gamma^\gamma_{\mu\nu}}{\partial x^\gamma} + \Gamma^\sigma_{\mu\gamma}\Gamma^\gamma_{\nu\sigma} - \Gamma^\sigma_{\mu\nu}\Gamma^\gamma_{\gamma\sigma} \ , \tag{B.10}$$

y R es el escalar de Ricci $R = g_{\alpha\beta} R^{\alpha\beta}$. Las ecuaciones B.9 pueden ser generalizadas añadiendo un nuevo término, que no viola ninguna de las anteriores 3 premisas, y que describe el contenido energético del universo presente en la constante cosmológica.

$$R_{\mu\nu} - \frac{1}{2} g_{\mu\nu} R + g_{\mu\nu}\Lambda = -8\pi G T_{\mu\nu},^{3} \tag{B.11}$$

Las ecuaciones de Friedmann

La geometría y la evolución del universo (como un todo) queda completamente descrita por la métrica B.5, la cual tiene 2 variables: la curvatura del universo, K, y el factor de expansión, $a(t)$. El valor de K depende de la masa total del universo mientras que la dependencia temporal del factor de expansión depende de la proporción de los diferentes componentes energéticos del universo. Si asumimos que en grandes escalas el universo puede ser descrito como un fluido perfecto y usamos las ecuaciones de Einstein B.11, obtendremos las llamadas ecuaciones de Friedmann [30][31]:

$$\begin{aligned} H^2 = \left(\frac{\dot{a}}{a}\right)^2 &= \frac{8\pi G}{3}\rho - \frac{Kc^2}{a^2} + \frac{\Lambda c^2}{3} \\ \dot{H} + H^2 = \frac{\ddot{a}}{a} &= -\frac{4\pi G}{3}\left(\rho + \frac{3p}{c^2}\right) + \frac{\Lambda c^2}{3}\ . \end{aligned} \tag{B.12}$$

$H(t) = \dot{a}/a$ es conocida como la función de Hubble. $H_0 \equiv H(t_0)$, con t_0 siendo el tiempo actual, es comúnmente parametrizado como $H_0 = 100\ h\frac{\text{km}}{\text{s Mpc}}$, donde $h \sim 0.7$. Para el resto de esta tesis consideraremos que la constante cosmológica es un fluido con densidad $\rho_\Lambda = \Lambda c^2/8\pi G$ y presión $p_\Lambda = -\rho_\Lambda c^2$.

En un universo que posee tres tipos de componentes energéticas, materia, radiación y una constante cosmológica, la densidad de energía total evolucionará de acuerdo a

$$\rho(a) = \rho_c^0 \left[\Omega_m^0 a^{-3} + \Omega_R^0 a^{-4} + \Omega_\Lambda^0\right]. \tag{B.13}$$

Donde hemos definido:

$$\Omega_i^0 = \frac{\rho_i^0}{\rho_c^0} \qquad \Omega_i = \frac{\rho_i(a)}{\rho_c(a)}\ . \tag{B.14}$$

Es interesante observar que la siguiente relación siempre se cumple

$$\Omega_m + \Omega_R + \Omega_\Lambda + \Omega_K = 1\ , \tag{B.15}$$

donde $\Omega_K = -\frac{Kc^2}{a^2H^2}$. Finálmente, mencionamos que la función de Hubble puede ser expresada como

---

[3] En el resto de esta tesis usaremos estas ecuaciones de Einstein

$$H(a) = H_0\sqrt{\Omega_\Lambda^0 + \Omega_K^0 a^{-2} + \Omega_m^0 a^{-3} + \Omega_R^0 a^{-4}}\ . \tag{B.16}$$

Redshift

Uno de los conceptos más usados en cosmología es el corrimiento al rojo o símplemente, redshift. Se puede mostrar, véase la sección 1.1.6, que la expansión del universo no solo modifica la frecuencia a la cual un objecto emite radiación, sino también la energía de los fotones que llegan a la Tierra. El redshift se define como el cambio entre las longitudes de onda emitidas y recibidas en la Tierra por un objecto

$$z = \frac{\lambda_{\rm obs} - \lambda_{\rm emi}}{\lambda_{\rm emi}} \tag{B.17}$$

donde λ_{obs} es la longitud de onda observada en la Tierra y λ_{emi} es la longitud de onda a la que emite el objecto. La relación entre el redshift y el factor de expasión viene dada por

$$1 + z = \frac{a_0}{a}\ . \tag{B.18}$$

El redshift es muy usado en cosmología y astrofísica ya que puede ser directamente medido usando los espectros de estrellas, galaxias...etc. Es una cantidad que esta íntimamente relacionada con distancias en cosmología: a mayor redshift mayor distancia.

B.2.2 Parámetros Cosmológicos

En esta subsección describimos brévemente cómo son medidas las proporciones de las diferentes componentes energéticas del universo. Los parámetros cosmológicos del modelo cosmológico estándar ($\Omega_{\rm CDM}$, $\Omega_{\rm b}$, Ω_Λ, Ω_K, H_0...etc) pueden constreñirse de diferentes formas, entre las que destacan el uso de supernovas, las anisotropías en el fondo cósmico de microondas y la estructura a gran escala del universo. Aquí mostramos la física que hay detras de cada método y cómo se extraen los parámetros cosmológicos en cada uno de ellos.

Supernovas

El estudio de las distancias de luminosidad de ciertas supernovas es considerado la primera prueba que apuntó hacia la existencia de una constante cosmológica.

Se puede demostrar que la relación entre la luminosidad aparente (también conocida como flujo) y la luminosidad absoluta de un objeto viene dada por (véase por ejemplo 1.2.1)

$$l = \frac{L}{4\pi r^2 a^2(t_0)(1+z)^2}\ , \tag{B.19}$$

donde r es una cantidad que depende de los parámetros cosmológicos de la siguiente forma

$$r(z) = S\left[\frac{1}{H_0}\int_{1/(1+z)}^{1}\frac{dx}{x^2\sqrt{\Omega_\Lambda + \Omega_K x^{-2} + \Omega_\mathrm{m} x^{-3} + \Omega_\mathrm{R} x^{-4}}}\right] , \tag{B.20}$$

siendo $S[y]$ el funcional

$$S[y] = \begin{cases} sin\ y & K \ = +1 \\ y & K \ = \ \ 0 \\ sinh\ y & K \ = -1 \end{cases} . \tag{B.21}$$

Las supernovas de tipo Ia son consideradas como candelas estándar porque se cree que su luminosidad absoluta es siempre la misma. Esto es de particular importancia ya que midiendo la luminosidad aparente y el redshift de este tipo de supernovas se puede extraer la función $r(z)$, la cual depende de los parámetros cosmológicos Ω_Λ, Ω_K, Ω_m, Ω_R y H_0.

Dado un conjunto de luminosidades aparentes de supernovas de tipo Ia a diferentes redshifts, y usando el hecho de que L es una constante, las expresiones B.19 y B.20 se pueden usar para constreñir los parámetros cosmológicos Ω_m, Ω_b, Ω_Λ, Ω_K y H_0. En la figura 1.1 se muestra la cantidad m-M (esta cantidad representa el cociente l/L) en función del redshift para diferentes supernovas de tipo Ia. De esos datos fue posible descartar la hipótesis de que el universo contuviera solo materia ($\Omega_m = 1$). El modelo que mejor reproduce los datos es uno que correponde a un universo plano ($K = 0$) con $\Omega_m \sim 0.3$ y $\Omega_\Lambda \sim 0.7$, indicando de esta forma la presencia de la energía oscura.

Fondo cósmico de microondas

Estudios de la distribución de las anisotropías en el fondo cósmico de microondas han permitido la determinación de los parámetros cosmológicos con una precisión sin precedente. En este apartado presentamos los principios físicos sobre los que se fundamenta este método.

En el universo primigenio, los fotones y los bariones estaban acoplados a través de la dispersión de Thompson formando un plasma. Cuando la temperatura del universo descendió suficiéntemente, los electrones se unieron a los protones formando átomos de hidrógeno, mientras que los fotones se liberaron de su interacción con los bariones, pudiendo viajar líbremente a través de todo el universo. Algunos de esos fotones llegan a la Tierra provenientes de todas direcciones con un increible grado de isotropía, presentado un espectro de cuerpo negro

$$I(\nu, T) = \frac{2h\nu^3}{c^2}\frac{1}{e^{h\nu/K_BT} - 1} , \tag{B.22}$$

donde $I(\nu, T)$ es la energía por unidad de tiempo, por unidad de área de la superficie que emite, por unidad de ángulo sólido y por unidad de frecuencia, con una temperatura promedio igual a 2.725 K.

La temperatura de este fondo de microondas no es totálmente isótropa, sino que presenta desviaciones de cerca de 1 parte en cien mil. Diferentes valores de los parámetros cosmológicos conducen a diferentes distribuciones de esas anisotropías. Por esa razón, el estudio de la distribución de las anisotropías del fondo cósmico de microondas puede ser usado para determinar el valor de los parámetros cosmológicos.

Una forma estándar de estudiar las perturbaciones en la temperatura del fondo de microondas es mediante su expansión en términos de los armónicos esféricos Y_l^m

$$\triangle T(\widehat{n}) = T(\widehat{n}) - T_0 = \sum_{lm} a_{lm} Y_l^m(\widehat{n}) \ , \tag{B.23}$$

donde $\widehat{n}$ es un vector normalizado en una dirección dada, $T(\widehat{n})$ es la temperatura en esa dirección y T_0 es la temperatura promedio del fondo cósmico de microondas,

$$T_0 = \frac{1}{4\pi} \int d^2\widehat{n} T(\widehat{n}) \ . \tag{B.24}$$

La cantidad más simple que caracteriza la distribución de anisotropias del fondo cósmico de microondas viene dada por el valor promedio del producto de dos $\triangle T(\widehat{n})$ (una cantidad aún más sencilla, $< \triangle T(\widehat{n}) >$, es explicitamente nula ya que hemos asumido que el universo es invariante bajo rotaciones):

$$< \triangle T(\widehat{n}) \triangle T(\widehat{n}') >= \sum_{lm} C_l Y_l^m(\widehat{n}) Y_l^{-m}(\widehat{n}') = \sum_l C_l \left(\frac{2l+1}{4\pi} \right) P_l(\widehat{n} \cdot \widehat{n}') \ , \tag{B.25}$$

donde P_I son los polinomios de Legendre. En la figura 1.2 mostramos el valor de los coeficientes C_l como función del momento del multipolo l según se ha medido con diferentes instrumentos. La posición, altura y anchura de los diferentes picos presentes en esa gráfica esta íntimamente relacionada con el valor de varios parámetros cosmológicos, los cuales pueden constreñirse usando este método. Para una descripción más detallada se recomienda la lectura del apartado 1.2.2.

Estructura a gran escala del universo

La distribución de materia en grandes escalas puede ser usada para constreñir los parámetros cosmológicos. En este apartado mostramos brévemente los métodos más usados para estudiar la distribución de materia en el universo y cómo los parámetros cosmológicos pueden ser inferidos a partir de tal distribución.

En el universo, las estrellas se agrupan en cúmulos de estrellas o galaxias, las galaxias a su vez se asocian en grupos o cúmulos de galaxias. Rodeando gigantescos agujeros cosmológicos, paredes y filamentos con miles o millones de galaxias forman lo que se denomina la red cósmica.

La distribución de materia en esas grandes escalas contiene información muy importante sobre el valor de los parámetros cosmológicos. La conocida como función de correlación, es una cantidad estadística que contiene información sobre la distribución de materia en el universo. Para un campo continuo se define como

$$\xi(|\mathbf{r}-\mathbf{r}'|) =< \delta(\mathbf{r})\delta(\mathbf{r}') > \tag{B.26}$$

mientras que para un campo discreto (por ejemplo un catálogo de galaxias) se define mediante

$$dP = \bar{n}^2(1+\xi(r_{12}))dV_1 dV_2 \ . \tag{B.27}$$

En la anterior ecuación dP es el diferencial de probabilidad de encontrar un par de galaxias separadas por una distancia r_{12}. $\bar{n}$ es el número medio de galaxias y dV_1 and dV_2 son los diferenciales de volumen de dos esferas cuyos centros están separados por una distancia r_{12}. Nótese que en la anterior ecuación, la función de correlación depende solo del módulo, no de la dirección del vector. Esto ocurre porque asumimos que el universo es invariante bajo rotaciones.

Ámpliamente usado en cosmología y encapsulando la misma información que la función de correlación, el espectro de potencias, $P(k)$, se define como transformada de fourier de la función de correlación:

$$P(\mathbf{k}) = \int \xi(\mathbf{r})e^{i\mathbf{k}\cdot\mathbf{r}}d^3\mathbf{r} \qquad\qquad \xi(\mathbf{r}) = \int P(\mathbf{k})e^{-i\mathbf{k}\cdot\mathbf{r}}\frac{d^3\mathbf{k}}{(2\pi)^3} \tag{B.28}$$

La forma del espectro de potencias depende críticamente del valor de los parámetros cosmológicos (véase por ejemplo la dependencia del espectro de potencias con la masa de los neutrinos en la figura 3.4). Mediante catálogos de galaxias, el espectro de potencias puede ser reconstruido, al menos en un intervalo de k's (véase por ejemplo [37][38][60]). El uso de métodos complementarios como el estudio de anisotropias en el fondo cósmico de microondas ó el bosque de Lyman-α tiene el potencial para reconstruir el espectro de potencias en un amplio rango de k, permitiendo una mejor estimación de los parámetros cosmológicos.

También merece especial atención formas adicionales de determinar los parámetros cosmológicos usando la estructura a gran escala del universo como las oscilaciones acústicas bariónicas o el estudio del bosque de Lyman-α. Para una descripción detallada de estos métodos referimos al lector al apartado 1.2.3.

B.3 Materia oscura

En esta sección presentamos la inmensa evidencia que apunta hacia la existencia de la materia oscura y los candidatos más plausibles a ser los constituyentes de la misma.

B.3.1 Evidencia observacional

La evidencia de la presencia de la materia es abrumadora. Desde la primera pista encontrada por Zwicky en 1933 al reciente descubrimiento del *bullet cluster*, la existencia de materia oscura en el universo es sustentada por numerosas observaciones. En esta subsección revisamos las más importantes. Para un análisis más extenso y profundo referimos al lector a [76][7].

Sistemas gravitacionalmente unidos

La primera pista sobre la existencia de materia oscura fue encontrada por Fritz Zwicky en 1933 [108] después de estudiar las propiedades del cúmulo de Coma. Usando el teorema del virial, Zwicky concluyó que la masa del cúmulo de Coma excedía muchas veces la masa estimada a través de la materia visible. En este apartado introducimos el teorema del virial y mostramos cómo Zwicky alcanzó su conclusión acerca de la presencia de materia oscura en el cúmulo de Coma.

Asumamos que un cúmulo de galaxias contiene N galaxias, cada una de las cuales tiene una masa promedio M_g y se mueve dentro del cúmulo a una velocidad promedio V_g. La energía cinética total del sistema viene dada por

$$T = \frac{1}{2} N M_g V_g^2 \ . \tag{B.29}$$

Para un cúmulo con N galaxias el número de pares de estas es $N(N-1)/2$, por lo tanto, la energía potencial total es

$$U = -\frac{1}{2} N(N-1) \frac{G M_g^2}{R} \ , \tag{B.30}$$

donde R es la distancia media entre galaxias. El teorema del virial afirma que para un sistema estable y autogravitacional, compuesto por objectos de la misma masa y esféricamente simétrico, la energía cinética total es igual a menos un medio de la energía potencial total del sistema

$$T = -\frac{1}{2} U \ . \tag{B.31}$$

La masa total del cúmulo puede, por lo tanto, ser estimada midiendo R y V_g y usando el teorema de virial

$$M_{cluster} = NM_g \cong \frac{2RV_g^2}{G} \ . \tag{B.32}$$

Zwicky midió el tamaño del cúmulo de Coma y la velocidad radial de las galaxias dentro del mismo. Aplicó el teorema del virial y calculó la masa total del cúmulo. Encontró que la masa del cúmulo tenía que ser cientos de veces mayor que su masa visible. Zwicky concluyó que el cúmulo de Coma estaba lleno de algún tipo de materia no visible que era la responsable de mantener unido gravitacionalmente el cúmulo.

Curvas de rotación de las galaxias espirales

Otra pista sobre la existencia de la materia oscura viene de las curvas de rotación de las galaxias espirales, que apunta hacia la existencia de un halo de materia oscura dentro de las mismas.

Las galaxias espirales son un tipo de galaxia que consisten en un disco plano que contiene estrellas y gas que rota, y en una concentración central de estrellas conocido como el bulbo. Tanto el gas como las estrellas rotan alrededor del centro de la galaxia en órbitas casi circulares. El perfil de velocidades de la galaxia puede ser fácilmente calculado igualando la fuerza centrífuga mv^2/r y la fuerza gravitatoria $GM(r)m/r^2$, donde m es o bien la masa de una partícula de gas o bien la masa de una estrella y $M(r)$ es la masa dentro de una esfera de radio r.

$$v = \sqrt{\frac{GM(r)}{r}} \tag{B.33}$$

De forma intuitiva, esperaríamos que lejos del centro de la galaxia, la función $M(r)$ no creciera mucho, y por lo tanto, el perfil de velocidad fuera como $\sim 1/\sqrt{r}$. Sorprendéntemente, este comportamiento no es el observado cuando se miden las curvas de rotación de las galaxias espirales. Por contra, la velocidad permanece casi constante para radios mayores que $\sim 5 \ kpc$.

En la figura 2.3 mostramos la medición del perfil de velocidades de la galaxia NGC3198. La contribución a la masa por parte del disco no es suficiente para explicar las propiedades observadas. Un halo de materia oscura es necesario para poder reproducir tales características.

Rayos X

El medio intergaláctico está lleno de gas caliente tal y como muestran las observaciones de rayos X. Asumiendo que ese gas esta en equilibrio hidrostático y que es esféricamente simétrico, se puede escribir la siguiente ecuación

$$\frac{GM(r)}{r^2} = \frac{1}{\rho(r)}\frac{dP(r)}{dr} \ , \tag{B.34}$$

donde $M(r)$ es la masa total dentro de una esfera de radio r, $\rho(r)$ es el perfil de densidad del gas y $P = nk_BT$ es la presión del gas. Usando la temperatura del gas $T(r)$ y su densidad $\rho = \mu m_p m$, con $\mu = 0.61$ siendo la masa promedio de las particulas del gas en unidades de la masa del protón m_p, es posible derivar el perfil de masa, $M(r)$, del cúmulo de galaxias.

Estudios de este tipo conducen a $M_{total}/M_b \geqslant 3$, indicando que la masa bariónica del cúmulo representa, como mucho, una tercera parte de la masa total. Por lo tanto, una componente no bariónica de masa hace falta para reproducir los perfiles observados de densidad y temperatura del cúmulo de galaxias.

Lente gravitacional

Dado que la luz se mueve a lo largo de geodésicas del espacio-tiempo, es de esperar que las trajectorias de los fotones emitidos por un objeto astrofísico (como por ejemplo una estrella o un quasar) sean desviadas cuando se aproximen al potencial gravitacional creado por una galaxia, un cluster de galaxias...etc.

En 1919, Sir Arthur Eddington verificó la desviación de los rayos de luz procedentes de estrellas cercanas a la posición del sol durante un eclipse. Esto es considerado como la primera prueba a favor de la validez de la teoría de la relatividad general.

El método de lente gravitacional permite medir la distribución de materia en la lente (el objeto astrofísico cuyo campo gravitacional curva los rayos de luz) estudiando la distribución espacial del objecto que sufre la deflección (para un resumen en este tema véase por ejemplo [77]). Los resultados muestran cláramente que la masa dentro de las lentes, tales como galaxias ó cúmulos de galaxias, es mucho mayor que la observada a través de su materia visible. De esta forma, una muy importante cantidad de materia contribuye a la masa total pero no al brillo total. La explicación más sencilla para este fenómeno es la presencia de materia oscura en esos objetos.

Fondo cósmico de microondas

El descubrimiento del fondo cósmico de microondas en 1964 [71] dio lugar al nacimiento de una era de precisón en cosmología. Tal y como hemos visto anteriormente, el fondo cósmico de microondas ha sido ampliamente usado para constreñir los parámetros cosmológicos. El estudio de las anisotropías en el fondo cósmico de microondas, y en particular el estudio de las correlaciones a diferentes tamaños angulares del cielo, ha permitido medir el contenido de materia oscura en el universo. El tercer pico de la función $C_l = C_l(l)$ (véase la figura

1.2) contiene información sobre Ω_m. Por lo tanto, midiendo su posición, altura y forma es posible inferir la existencia de una componente de materia oscura en el universo.

Las medidas más actuales indican que el contenido energético del universo esta formado por bariones ($\sim 4.5\%$), materia oscura ($\sim 23\%$) y energía oscura ($\sim 72\%$).

Oscilaciones acústicas bariónicas

En el plasma primordial, los fotones y los electrones estaban acoplados a través de la dispersión de Thompson. Las anisotropías en el campo de densidad produjo ondas acústicas que se propagaron a través del plasma hasta el momento del desacoplamiento. Esas ondas dejaron una huella en la distribución de bariones que puede ser observada a través de catálogos de galaxias.

Esas ondas, cuyos radios pueden ser fácilmente calculados, representan lo que se denomina una *regla estándar* puesto que su tamaño permaneció inalterado tras el instante del desacoplamiento. La escala de las oscilaciones acústicas bariónicas depende del contenido de materia oscura en el universo y de la constante de Hubble, h. El cociente Ω_b/Ω_m puede ser medido, obteniéndose un valor de 0.18 ± 0.04, que está en perfecto acuerdo con las medidas del fondo cósmico de microondas.

El ***bullet cluster***

El cúmulo de galaxias 1E0657-56 [59], también conocido como el bullet cluster, es el resultado de la colisión de dos cúmulos de galaxias. Constituye una de las evidencias más directas de la presencia de materia oscura y un auténtico desafío para teorias como MOND (MOdified Newtonian Dynamics).

El método de lente gravitacional ha encontrado que la mayor parte de la masa del sistema se encuentra en dos regiones diferentes de cúmulo, mientras que la emisión más fuerte en forma de rayos X no tiene lugar en esas zonas. En la figura 2.4 se muestra con líneas verdes los contornos de masa de la reconstrucción por lente gravitatoria mientras que la emisión en rayos X se muestra sobre ellos. La explicación más sencilla de esta configuración es que dos cúmulos de galaxias colisionaron, y mientras que tanto las estrellas como la materia oscura no fueron significativamente alterados y se cruzaron sin mucha interacción (aparte de la interacción gravitatoria producida por el otro cúmulo), el gas presente en los cúmulos interaccionó electromagnéticamente entre sí, reduciendo en gran medida su velocidad. Esta descripción explica muy bien la morfología del bullet cluster mientras que teorias como MOND requieren de escenarios mucho más exóticos para reproducirla.

B.3.2 Candidatos

Tal y como hemos descrito en la subsección anterior, la presencia de materia oscura está sustentada por numerosas observaciones. En esta subsección revisamos brévemente los candidatos a constituir la materia oscura[4]. Resaltamos a su vez que a día de hoy no se ha encontrado evidencia experimental por parte de experimentos de física de partículas.

MACHO's

Uno de los posibles candidatos a ser la materia oscura pueden ser objetos que tienen una luminosidad muy baja o casi nula tales como planetas, enanas marrones, estrellas de neutrones o agujeros negros. Estos objetos pertenecen a la categoría de MACHO's (Massive Astrophysical Compact Halo Objects) y la ventaja de considerarlos es que están compuestos de materia bariónica, y por lo tanto, no hay necesidad de introducir ninguna partícula más allá de modelo estándar.

La hipótesis que afirma que la materia oscura esta compuesta de objetos con baja o nula luminosidad puede ser comprobada buscando eventos de microlente gravitatoria que tendrían lugar cuando uno de esos objetos astrofísicos pasara por delante de una estrella. El proyecto MACHO encontró entre 13 y 17 eventos de microlente tras 5.7 años de observación fotométrica de 11.9 millones de estrellas [3]. Ese número tan pequeño de eventos es capaz de descartar totalmente la posibilidad de que la materia oscura este compuesta de MACHO's.

WIMP

El modelo estándar de partículas presenta ciertos problemas como por ejemplo las masas de los neutrinos, que ese modelo considera nulas mientras que los experimentos de oscilación de neutrinos demuestran que la suma de sus masas debe ser igual ó mayor que $\Sigma m_\nu \sim 0.05$ eV. Extensiones del modelo estándar representan una manera natural de resolver esos problemas. Una de esas extensiones es conocida como supersimetría. En supersimetría, cada partícula del modelo estándar tiene tiene un supercompañero que difiere de él por 1/2 en spín. En otras palabras, cada bosón del modelo estándar está asociado con un fermión supersimétrico y cada fermión del modelo estándar está asociado con un bosón supersimétrico. Si esta simetría fuera perfecta, las masas de los supercompañeros tendrían que ser las mismas que la de sus compañeros del modelo estándar. Dado que esas partículas no se han encontrado, esa simetría tiene que estar rota, permitiendo a los supercompañeros ser mucho mas pesados que las partículas del modelo estándar. En muchos modelos, supersimetría asigna un nuevo número cuántico multiplicativo, R, que es igual a +1 para partículas del modelo estándar y -1 para partículas supersimétricas. Este número es conservado en cualquier reacción, lo que significa que la partícula supersimétrica más ligera debe ser estable y que solo puede decaer a partículas del modelo estándar a través de aniquilaciónes consigo misma. El nombre WIMP surge de *Weakly Interacting Massive Particles* y supersimetría introduce un candidato de manera natural.

La importancia de este tipo de partículas es que pueden, de forma natural, reproducir

---

[4] Hacemos saber que la lista de candidatos a materia oscura es muy large, sin embargo, en esta tesis solo presentamos a los más populares

el valor de $\Omega_m \sim 0.3$ símplemente asumiendo que tienen una masa en el rango de 10 GeV-1 TeV. Dado que esas partículas solo se ven afectadas por la interacción débil y la gravitatoria, su detección supone un reto. Una de las formas estándar de buscar este tipo de partículas es mediante el retroceso que ellas producen en núcleos atómicos cuando colisionan con los mismos. Hasta la fecha, ninguna evidencia definitiva se ha encontrado al respecto.

Axiones

Los axiones son otro candidato a materia oscura. Estas partículas surgen como una solución natural al problema fuerte de CP en cromodinámica cuántica. Este problema aparece como consecuencia de que no existe ninguna motivación teórica de que la simetría CP deba ser conservada en cromodinámica cuántica. Por lo tanto, cuando escribimos todos los posibles términos en el lagrangiano de QCD (cromodinámica cuántica), uno de ellos, el cual viola CP, aparece de forma natural. Este término implica que el neutrón debe de tener un momento eléctrico dipolar. Para satisfacer los límites experimentales en esta cantidad, el coeficiente de este término tiene que ser extremadamente pequeño. La razón por la cual este término es tan pequeño o nulo representa un problema para QCD.

Como una posible solución a este problema, Peccei and Quinn [69] postularon la existencia de una nueva simetría, la simetría de Peccei-Quinn, la cual se rompe espontáneamente. Cuando esta simetría se rompe, una nueva partícula, el axión, aparece. El papel del término que viola CP en el lagrangiano de QCD es jugado ahora por el axión.

Los axiones tienen que ser eléctricamente neutros, deben tener una masa muy pequeña y una sección eficaz muy baja para las fuerzas débil y fuerte. Debido a estas débiles interacciones, los axiones no estuvieron en equilibrio con otras partículas. Aunque tienen masa muy pequeñas, ellos pueden ser fríos (es decir, puede tener velocidades térmicas muy bajas). Estas propiedades hacen de los axiones un candidato muy interesante a ser la materia oscura.

B.4 Neutrinos

En esta sección introducimos los neutrinos y sus principales propiedades. Discutimos las oscilaciones de neutrinos y los límites actuales sobre sus masas. Presentamos los neutrinos cosmológicos, tal y como son predichos por el modelo cosmológico estándar y acabamos la sección mostrando los principales efectos que inducen en cosmología en el régimen lineal.

B.4.1 Introducción

Los neutrinos fueron postulados en 1930 por Wolgang Pauli para evitar los problemas de violación de energía, momento y spin en el proceso de decaimiento beta

$$n \longrightarrow p^{+} + e^{-} + \overline{\nu}_e \ . \tag{B.35}$$

Las implicaciones de esa hipótesis eran:

- La masa del neutrino tiene que ser pequeña.
- Los neutrinos tienen que ser eléctricamente neutros.
- Los neutrinos no pueden ser sensibles a la interacción fuerte.

Los neutrinos fueron detectados experimentalmente en 1956 en un experimento llevado a cabo por Clyde Cowan y Frederick Reines [22]. Ellos usaron una fuente de $\sim 5 \times 10^{13}$ ν/s, que venía de un reactor nuclear, y buscaron señales de la reacción

$$\overline{\nu}_e + p^{+} \longrightarrow n + e^{+} \ . \tag{B.36}$$

El positrón generado en esa reacción se desintegra rápidamente con un electrón e^{-}, produciendo un par de rayos gamma. La detección de esos rayos gamma mas la captura posterior del neutrón produce una señal inequívoca de la existencia de los neutrinos. Esa señal fue encontrada por Cowan y Reines en su famoso experimento, demostrando experimentalmente la existencia de los neutrinos.

Los neutrinos son un componente del modelo estándar de partículas. Son fermiones de spin 1/2 y dentro de ese modelo, son partículas sin masa. El decaimiento del boson Z indica que el número de neutrinos que son sensibles a la interacción débil es $N_\nu = 2.994 \pm 0.012$ [68]. Debido a su pequeña sección eficaz, la detección de estos neutrinos es especiálmente complicada. De los experimentos de oscilación de neutrinos sabemos que la masa, de al menos dos de ellos, no es nula. Esto sugiere que el modelo estándar de partículas debe ser ampliado para acomodar tanto a neutrinos masivos como a un candidato a materia oscura.

B.4.2 Masas

Por casi 40 años, una importante discrepancia surgió entre el número de neutrinos que llegan a la Tierra desde el sol y el número esperado de estos a través de cálculos teóricos. Esta discrepacia es conocida como el problema de los neutrinos solares:

Los neutrinos son producidos en el centro del sol por procesos nucleares como

$${}^{1}_{1}H + {}^{1}_{1}H \longrightarrow {}^{2}_{1}H + e^{+} + \nu_e \ . \tag{B.37}$$

Esos neutrinos, debido a su débil sección eficaz, viajan hasta la Tierra sin casi interacciones con otras partículas. Sin embargo, el número de neutrinos que alcanzan la Tierra, tal y como muestran los experimentos, es cerca de un factor 3 más pequeño que la predicción de los modelos teóricos.

La solución a este problema viene de las llamadas oscilaciones de neutrinos, implicando que los neutrinos tienen masa: en el sol, los neutrinos son producidos como neutrinos electrónicos, ν_e, por reacciones como B.37, pero existe una probabilidad no nula de que esos neutrinos cambien su sabor en su camino hacia la Tierra. Aproximádamente 2/3 de los neutrinos electrónicos más energeticos producidos en el centro del sol oscilan, cambiando su sabor a μ-neutrinos, ν_μ, en su camino hacia la Tierra. Como consecuencia, el número de neutrinos energéticos (en el rango de varios MeV) sensibles a detección se reduce en 1/3, explicando la discrepancia entre el número medido y el número esperado. Esta solución también fue confirmada por la observación de la desaparición de $\overline{\nu}_e$ neutrinos en el detector Kamland. Una situación parecida ocurre con los conocidos como neutrinos atmosféricos.

Las oscilaciones de neutrinos, medidas con neutrinos solares, atmosféricos, de reactores y de aceleradores, nos informan de la diferencia de sus masas al cuadrado y de sus ángulos de mezcla $sin\ \theta_{ij}$ [33] (véase 3.2 para una descripción más completa)

$$\triangle m_{21}^2 = (7.6 \pm 0.2) \times 10^{-5}\ eV^2\ , \tag{B.38}$$

$$|\triangle m_{31}^2| = (2.4 \pm 0.1) \times 10^{-3}\ eV^2\ . \tag{B.39}$$

$$\theta_{12} = 34.4 \pm 1.0 \tag{B.40}$$

$$\theta_{23} = 42.8^{+4.7}_{-2.9} \tag{B.41}$$

$$\theta_{13} = 5.6^{+3.0}_{-2.7} \tag{B.42}$$

$$\delta_{\mathrm{CP}} \in [0, 360] \tag{B.43}$$

El valor absoluto presente en $\triangle m_{31}^2$ da lugar a dos posibles jerarquías dependiendo de si el signo es positivo (jerarquía normal), o si el signo es negativo (jerarquía inversa). En la figura 3.1 mostramos las 2 diferentes jerarquías y la distribución de masas asociadas con ellas. En la figura 3.2 mostramos, para los dos esquemas, la suma de las tres masas de los neutrinos, $\Sigma_i m_{\nu_i}$ en función de la masa del más ligero.

Los actuales límites superiores en la masa del neutrino electrónico que vienen de experimentos de física de partículas se obtienen del decaimiento beta del tritio. En un intervalo de confianza del 95%, la masa del neutrino electrónico está por debajo de $m < 2.05 - 2.3$ eV [53][48].

Los límites cosmológicos son mucho más fuertes, estableciendo límites superiores en la suma de la masa de los neutrinos, $\Sigma_i m_{\nu_i}$, por debajo de ~ 1 eV. Las anisotropias del fondo cósmico de microondas son sensibles a las masas de los neutrinos. Límites de $\Sigma_i m_{\nu_i} < 1.3$ eV [47] se obtienen usando únicamente esas anisotropías, mientras que al combinarlos con datos de la estructura a gran escala del universo se reducen a $\Sigma_i m_{\nu_i} < 0.3$ eV [99, 89, 34, 73].

B.4.3 Neutrinos cósmicos

En los primeros instantes tras el Big Bang, los neutrinos estaban en equilibrio térmico con otras partículas en el plasma primordial mediante reacciones como

$$e^+ \; + e^- \longrightarrow \; \nu \; + \; \overline{\nu} \; . \tag{B.44}$$

Estando en equilibrio térmico, la densidad de neutrinos con masa m_ν y momento entre p and $p + dp$ viene dado por la distribución de Fermi-Dirac

$$n_\nu(p,T) = \frac{4\pi g p^2}{(2\pi\hbar)^3} \left(\frac{1}{e^{\sqrt{p^2+m_\nu^2}/k_B T} + 1} \right) \; , \tag{B.45}$$

con $g = 2$ siendo el número de estados de spín de los neutrinos. Cuando la temperatura bajó por debajo de $T \sim 10^{10}$K ($k_B T \sim 1$ MeV[5]), el ritmo de expansión del universo fue mayor que el ritmo de colisiones que mantenían a los neutrinos en equilibrio térmico con las otras partículas. En ese momento, los neutrinos se desacoplaron del plasma y pudieron viajar como partículas libres. Aquí mostramos que la distribución de neutrinos cósmicos se *congela* una vez estos se desacoplan.

Asumiendo que las masas de los neutrinos son, como máximo, del orden del eV, podemos afirmar que en el momento del desacoplo los neutrinos eran relativistas ($k_B T \gg m_\nu$), de forma que podemos hacer la aproximación $E = \sqrt{p^2 + m^2} \cong p$. Una vez los neutrinos se desacoplaron, su momento escala con la expansión del universo como

$$p_\nu \sim a^{-1} \; , \tag{B.46}$$

de forma que podemos escribir la densidad de los neutrinos en un tiempo posterior a su desacoplamiento como

$$n_\nu(p,z) = \frac{4\pi g p^2}{(2\pi\hbar)^3} \left(\frac{1}{e^{p/k_B T_\nu(z)} + 1} \right) \; , \tag{B.47}$$

donde $T_\nu(z) = T_\nu^0(1 + z)$. T_ν^0 es la temperatura actual del fondo cósmico de neutrinos. Se puede mostrar que esa temperatura esta relacionada con la temperatura de los fotones del fondo cósmico de microondas mediante [104]

$$T_\nu = \left(\frac{4}{11} \right)^{1/3} T_\gamma \; . \tag{B.48}$$

Dado que la temperatura actual del fondo cósmico de microondas es de $T_\gamma^0 = 2.725$ K, concluimos que la distribución del fondo cósmico de neutrinos tiene una temperatura igual

---

[5] $k_B = 8.617 \times 10^{-5}$ eV/K

a $T_\nu^0 = 1.95$ K $(1.68 \times 10^{-4}$ eV). La densidad actual de neutrinos cósmicos por especie viene dada por

$$n_\nu^0 = \frac{4\pi g}{(2\pi\hbar)^3} \int_0^\infty \frac{p^2 dp}{e^{p/k_B T_\nu^0} + 1} \simeq 113 \frac{\nu}{\mathrm{cm}^3} \ . \tag{B.49}$$

La densidad de energía y presión de los neutrinos puede ser calculada mediante:

$$\rho_\nu(z) = \int_0^\infty n_\nu\,(p,z)\, dp \sqrt{p^2 + m_\nu^2} \ , \tag{B.50}$$

$$P_\nu(z) = \int_0^\infty n_\nu\,(p,z)\, dp \frac{p^2}{3\sqrt{p^2 + m_\nu^2}} \ . \tag{B.51}$$

En el régimen donde $m_\nu \gg T_\nu$ podemos aproximar el factor $\sqrt{p^2 + m_\nu^2}$ por m_ν, y usar las anteriores expresiones para encontrar que $\rho_\nu(z) = \rho_\nu^0(1+z)^3$ y $P_\nu(z) \sim 0$. Esto demuestra el hecho de que cuando los neutrinos dejan de ser relativistas (a bajo redshift), se comportan como materia. Por contra, en el régimen donde $m_\nu \ll T_\nu$, el factor $\sqrt{p^2 + m_\nu^2}$ puede ser aproximado por p. Esto conduce a una dependencia temporal $\rho_\nu(z) = \rho_\nu^0(1+z)^4$ y $P_\nu(z) = \rho_\nu(z)/3$ que reproduce el comportamiento de radiación.

Los neutrinos dejan de ser relativistas aproximadamente a un redshift

$$z_{\mathrm{non-relativistics}} \sim 2000 \left(\frac{m_\nu}{1 \ \mathrm{eV}}\right) \ . \tag{B.52}$$

En el régimen en el que los neutrinos son altamente no-relativistas, el cociente entre la densidad energética de los neutrinos y la densidad crítica puede ser fácilmente calculada usando la ecuación B.50 y teniendo en cuenta que $m_\nu \gg T_\nu$. Esto produce $\rho_\nu^0 \cong 113 \ \mathrm{eV/cm}^3 \times \Sigma_i m_{\nu_i}$ que junto con $\rho_c^0 = 1.054 \times 10^4 \ h^2 \ \mathrm{eV/cm}^3$ genera:

$$\Omega_\nu h^2 \simeq \frac{\Sigma_i m_{\nu_i}}{93.3 \ eV} \ . \tag{B.53}$$

La velocidad térmica promedio de los neutrinos cósmicos, cuando estos no son relativistas, puede ser fácilmente calculada a partir de la distribución B.47, y es aproximadamente igual a

$$\overline{v}_\nu = 150(1+z) \left(\frac{1 \ \mathrm{eV}}{m_\nu}\right) \ \mathrm{km \ s}^{-1} \ . \tag{B.54}$$

B.4.4 Impacto en cosmología

Los neutrinos cósmicos juegan un papel muy importante en cosmología. Sus grandes velocidades hacen que se comporten de un manera radicalmente opuesta a la de la materia oscura fría. En esta subsección explicamos como las altas velocidades de los neutrinos impactan en el crecimiento de las perturbaciones de materia oscura fría y por lo tanto, en la estructura a gran escala del universo.

Aquí mostramos dos efectos que los neutrinos inducen en el proceso de formación de estructuras si una parte de la materia oscura esta compuesta por neutrinos. Esto es equivalente a mantener fija la densidad total de materia oscura, Ω_{dm}, separándola entre materia oscura fría y neutrinos $\Omega_{\mathrm{dm}} = \Omega_{\mathrm{CDM}} + \Omega_\nu$.

El primer efecto inducido es que los neutrinos modifican el tiempo al cual tiene lugar la igualdad materia-radiación. Este tiempo representa la época en la cual la contribución de la radiación a la energía total del universo se iguala a la contribución de la materia, y es dada por

$$a_{\mathrm{eq}} = \frac{\Omega_{\mathrm{r}}}{\Omega_{\mathrm{b}} + \Omega_{\mathrm{CDM}}} \tag{B.55}$$

con Ω_{r} reciviendo contribuciones de fotones y neutrinos. Dado que ambos modelos, con neutrinos masivos o con neutrinos sin masa, contribuyen de igual forma a Ω_{r} en esa época (en esa época, neutrinos de masas $\Sigma_i m_{\nu_i} \lesssim 1$ eV son muy relativistas, de forma que contribuyen a la densidad de energía como radiación en lugar de materia), el decrecimiento en Ω_{CDM}, debido a los neutrinos masivos, modifica ese tiempo por un factor $(1 - f_\nu)^{-1}$

$$a_{\mathrm{eq}}^{f_\nu} = a_{\mathrm{eq}}^{f_\nu = 0}(1 - f_\nu)^{-1} \ , \tag{B.56}$$

con f_ν definido como:

$$f_\nu = \frac{\Omega_\nu}{\Omega_{\mathrm{m}}} = \frac{\Omega_\nu}{\Omega_{\mathrm{b}} + \Omega_{\mathrm{CDM}} + \Omega_\nu} \ . \tag{B.57}$$

Dado que las perturbaciones de materia oscura fría no crecen tan rápido en la era de radiación dominante ($\delta \propto \ln(a)$) como en la era de materia dominante ($\delta \propto a$), el retraso en la igualdad materia-radiación, en comparación con el modelo con neutrinos sin masa, inducido por las masas de los neutrinos, producirá que las estructuras esten menos desarrolladas en un universo con neutrinos masivos que en uno con neutrinos sin masa.

El segundo efecto tiene lugar una vez las perturbaciones de materia oscura fría entran en la era de materia dominante. Los neutrinos ralentizan el ritmo al cual esas perturbaciones crecen. Para entender mejor este efecto, escribamos las leyes de conservación de la masa y el momento para un fluido ideal:

$$\left(\frac{\partial \rho}{\partial t}\right)_{\mathbf{r}} + \vec{\nabla}_{\mathbf{r}} \cdot (\rho \mathbf{u}) = 0 \tag{B.58}$$

$$\left(\frac{\partial \mathbf{u}}{\partial t}\right)_{\mathbf{r}} + (\mathbf{u} \cdot \vec{\nabla}_{\mathbf{r}})\mathbf{u} = -\vec{\nabla}_{\mathbf{r}} \Phi \tag{B.59}$$

con $\rho(\mathbf{r},t)$, $\mathbf{u}(\mathbf{r},t)$ y $\Phi(\mathbf{r},t)$ siendo la densidad, velocidad y potencial gravitatorio del fluido perfecto respectivamente. Estas ecuaciones junto con la ecuación de Poisson,

$$\nabla^2_{\mathbf{r}}\Phi = 4\pi G\rho \ , \tag{B.60}$$

especifican completamente la evolución del fluido ideal una vez las condiciones iniciales están dadas. La ecuación linearizada que gobierna la evolución de perturbaciones de materia oscura fría puede encontrarse usando las anteriores ecuaciones (véase por ejemplo [65])

$$\ddot{\delta}_{\rm CDM} + 2\frac{\dot{a}}{a}\dot{\delta}_{\rm CDM} = 4\pi G\overline{\rho}_{\rm CDM}\delta_{\rm CDM} \ , \tag{B.61}$$

donde $\overline{\rho}_{\rm CDM}$ es la densidad del fondo de materia oscura fría, $\delta_{\rm CDM}$ es la perturbación de materia oscura fría $\rho_{\rm CDM}(\mathbf{x},t) = \overline{\rho}_{\rm CDM}(t)[1+\delta_{\rm CDM}(\mathbf{x},t)]$ y $\mathbf{x} = \mathbf{r}/a$ es la coordenada comovil. La ecuación B.61 tiene como solución general:

$$\delta_{\rm CDM}(\mathbf{x},t) = A(\mathbf{x})D_1(t) + B(\mathbf{x})D_2(t) \ , \tag{B.62}$$

con D_1 and D_2 siendo los modos creciente y decreciente respectivamente. Se puede demostrar (véase la sección 3.4) que en la época de materia dominante, el modo creciente va como $D_1(a) \simeq a^{1-(3/5)f_\nu}$. Por lo tanto, en un universo con neutrinos sin masa, las estructuras crecerán a un ritmo mayor que en un universo con neutrinos masivos.

Uno de los conceptos más útiles en cosmología es el llamada *espectro de potencias*. Se define como la función de correlación a dos puntos de fluctuaciones de materia no-relativista en el espacio de Fourier

$$P(k,z) =< |\delta_{\rm m}(k,z)|^2 > \ , \tag{B.63}$$

siendo $\delta_m = \delta\rho_m/\overline{\rho}_m$ el contraste de densidad de materia. Es posible resolver numéricamente las ecuaciones que gobiernan el crecimiento de perturbaciones en el régimen lineal, y por lo tanto, calcular el espectro de potencias. En la figura 3.4 mostramos el espectro de potencias en el régimen lineal para un universo con neutrinos sin masa y parámetros cosmológicos: $\Omega_{\rm CDM} = 0.25$, $\Omega_b = 0.05$, $\Omega_\Lambda = 0.7$, $n_{\rm s} = 0.95$, $h = 0.7$ and $\sigma_8 = 0.8$. También mostramos el espectro de potencias lineal de diferentes modelos cosmológicos que satisfacen $\Omega_\nu + \Omega_{\rm CDM} = 0.25$.

Como se puede ver en esa figura, los neutrinos suprimen el espectro de potencias en pequeñas escalas. Esta supresión es una consecuencia de los dos efectos discutidos anteriormente.

B.5 Resumen y conclusiones

La motivación de esta tesis ha sido la necesidad de estudiar el impacto de una componente dominante (la materia oscura templada) y de una componente subdominante (los neutrinos cosmológicos) de materia oscura no fría en la estructura a gran escala del universo. Por una parte hemos dado respuesta al interrogante sobre si la materia oscura templada puede solucionar, o al menos aliviar, el problema de los picos/núcleos. Por otra parte, hemos buscando observables cosmológicos que sean sensibles a las masas de los neutrinos a través del estudio del impacto de los neutrinos cosmológicos en estructuras no-lineales tales como cúmulos de galaxias o agujeros cosmológicos.

La materia oscura templada surge como una posible solución a varios problemas presentes al considerar que la materia oscura es fría: la observación de núcleos en el perfil de materia oscura de galaxias de baja luminosidad superficial y el número de halos de materia oscura que rodean galaxias como nuestra Vía Láctea. Las simulaciones cosmológicas de N-cuerpos con materia oscura fría muestran que el perfil de densidad de los halos de materia oscura ajusta muy bien al perfil de Navarro-Frenk-White (NFW). Este perfil presenta un pico (la densidad tiende a infinito) en el centro del halo dado que la densidad de materia oscura crece como $1/r$ al aproximarse al centro del halo. Por contra, el perfil de materia oscura de ciertas galaxias, como por ejemplo las galaxias de baja luminosidad superficial, parece presentar un núcleo en lugar de un pico. Debido al límite de Tremaine-Gunn, se espera que la materia oscura templada, constituida por partículas que no tienen una velocidad térmica despreciable, forme estructuras que presenten un núcleo en su perfil de densidad. Con el fin de preservar la jerarquía del proceso de formación de estructuras (de estructuras pequeñas a estructuras grandes), en esta tesis hemos considerado un tipo genérico de materia oscura templada compuesto por partículas con velocidades térmicas tales que su recorrido libre sea de ~ 100 kpc/h. Puesto que la resolución actual de las simulaciones cosmológicas de N-cuerpos[6] no es suficiente como para resolver los tamaños de los núcleos encontrados en las galaxias de bajo luminosidad superficial, hemos usado un método para calcular el perfil de densidad de la materia oscura templada que es consistente con la distribución de velocidades de sus constituyentes. Hemos investigado la dependencia de nuestros resultados con el tiempo al que el halo de materia oscura templada colapsa, con la masa y con la temperatura de sus constituyentes. Nuestros resultados indican que la materia oscura templada produce, en efecto, núcleos en el perfil de densidad de los halos, pero su tamaño no es lo suficientemente grande como para reproducir los observados en las galaxias de baja luminosidad superficial. Nosotros encontramos que a pesar de que tamaño típico de los núcleos en el perfil de densidad suelen ser de $r_{core}/r_{200} \approx 0.05$, la materia oscura templada sólo puede producir núcleos 50 veces más pequeños $r_{core}/r_{200} \approx 10^{-3}$. Concluimos que la solución al problema de los picos/núcleos debe venir de procesos astrofísicos, como explosiones de supernovas, en lugar de la naturaleza de la materia oscura.

Los neutrinos son una de las partículas más misteriosas de la naturaleza, y desde el descubrimiento de las oscilaciones de neutrinos sabemos que tienen masa. La teoría del Big

---

[6] Nótese que esta tesis ha sido escrita en diciembre de 2011

Bang predice la existencia de un fondo cósmico de neutrinos con una temperatura actual cercana a los 2 K. Aun a pesar de que a esa temperatura los neutrinos no son relativistas, tienen velocidades térmicas elevadas. Por esa razón, los neutrinos son comúnmente considerados como materia oscura caliente. En un universo dominado por materia oscura caliente, el proceso de formación de estructuras sería de arriba hacia abajo, en contra de lo que se observa. Por lo tanto, los neutrinos cósmicos no pueden ser la componente dominante de la materia oscura. Por otra parte, dado que tienen masa, los neutrinos constituyen una componente subdominante caliente de la materia oscura. Intentando responder a una de las cuestiones más importantes en física, ¿cual es la masa de los neutrinos?, en esta tesis hemos estudiado el impacto de los neutrinos cosmológicos en estructuras no lineales, buscando nuevos observables cosmológicos que sean sensibles a las masas de los neutrinos.

Los neutrinos cósmicos tienen una velocidad térmica promedio aproximádamente igual a $150(1+z)(eV/m_\nu)$ km/s. Por lo tanto, sus velocidades son lo suficientemente bajas como para caer en pozos de potencial suficientemente profundos como los que existen en los cúmulos de galaxias. En esta tesis hemos estudiado la formación de halos de neutrinos en los pozos de potencial de cúmulos de galaxias y como su presencia podría ser detectada usando el método de lente débil. Tal y como se espera, hemos encontrado que esos halos de neutrinos presentan tres grandes diferencias con respecto a sus primos de materia oscura: los halos de neutrinos tienen tamaños mucho más grandes que los de materia oscura, su perfil de densidad es mucho más pequeño y presentan un núcleo muy grande en el mismo. Estas propiedades surgen como consecuencia de las velocidades de los neutrinos (las cuales dependen exclusívamente de las masas de los neutrinos); cuanto más pequeñas sean las velocidades de los neutrinos, más parecidos serán sus perfiles a los de materia oscura. Estos halos de neutrinos contribuyen a la masa total del halo de materia oscura y su contribución puede ser medida usando métodos de lente débil. La forma de un objeto que está situado tras una lente gravitatoria extensa es modificada por la desviación, por parte de la lente, de sus rayos de luz. Esa distorsión depende del perfil de masa projectada de la lente. Dado que los neutrinos cósmicos modifican el perfil de densidad de los cúmulos de galaxias (y por lo tanto el perfil de masa projectada de la lente), añadiendo una contribución a sus masas totales, las masas de los neutrinos pueden ser constreñidas usando un catálogo de objetos débilmente distorsionados por una lente gravitatoria. Hemos calculado la perturbación producida por los neutrinos cosmológicos en la forma de los objetos distorsionados y encontramos que el valor de esa perturbación, en el radio virial para 3 familias degeneradas de neutrinos, cada una con una masa de 0.3 eV, es aproximadamente igual al 1%. Para masas de neutrinos más pequeñas y/o radios más pequeños las perturbaciones ocasionadas por los neutrinos son más pequeñas. El método propuesto en esta tésis es capaz de medir los efectos de los neutrinos cósmicos en los cúmulos de galaxias, y por lo tanto constreñir las masas de los neutrinos, si otros efectos que también afectan las propiedades de los objetos distorsionados están bajo control. Puesto que esos efectos, tales como la función de selección o la distribución de bariones, son muy difíciles de controlar, la detección de los neutrinos cósmicos usando el método de lente débil supone un reto.

En esta tesis también hemos estudiado el impacto de los neutrinos cósmicos en los agujeros cosmológicos. Los agujeros cosmológicos son regiones del universo, con densidades por debajo de la densidad promedio del universo, donde la materia oscura esta siendo evacuada hacia las partes exteriores del agujero a una velocidad superior a la de la expansión del universo. Ignorando efectos tales como las fuerzas de marea o las subestructuras, la tasa de evacuación de materia oscura a una determinada distancia del centro del agujero es controlada por la masa del agujero contenida en una esfera de ese radio. Por esa razón, cuanto más vacío este el agujero más rápido estará evacuando materia oscura. Dado que los neutrinos cosmológicos tienen velocidades térmicas muy grandes, ellos no se verán tan afectados por la dinámica de los agujeros cosmológicos como lo hará la materia oscura. Por lo tanto, es de esperar que mientras que la materia oscura sienta la dinámica de los agujeros y los evacúe, vaciando aún más el agujero, los neutrinos cosmológicos se mantendrán dentro del agujero cosmológico, añadiendo una contribución a su masa y de esta forma, ralentizando el ritmo de evacuación de materia oscura. Usando el modelo de colapso esférico, hemos encontrado que los neutrinos producen, en efecto, un fuerte impacto en las propiedades de los agujeros cosmológicos. Hemos hallado que los neutrinos retrasan tanto el tiempo al cual el agujero entra en su fase no lineal como el ritmo de evacuación de la materia oscura. En un universo con neutrinos masivos, los agujeros cosmológicos serán más pequeños, más densos y estarán menos desarrollados que sus equivalentes en un universo sin neutrinos masivos.

Para estudiar de forma general y sin hacer ninguna suposición (tales como que las fuerzas de marea y las subestructuras no juegan un papel importante) las propiedades de los agujeros cosmológicos, hemos corrido simulaciones de N-cuerpos con materia oscura fría, bariones y neutrinos masivos y hemos comparados los resultados con los que se obtienen de correr simulaciones de N-cuerpos con materia oscura fría, bariones y neutrinos sin masa. Hemos encontrado que los resultados concuerdan con lo que esperabamos, es decir, hemos encontrado que los agujeros cosmológicos son más pequeños, más densos y están menos desarrollados en un universo con neutrinos masivos que en un universo con neutrinos sin masa. Hemos buscado nuevos observables cosmológicos que sean sensibles a las propiedades de los agujeros cosmológicos y que pudieran ser usados para constreñir la masa de los neutrinos. Hemos encontrado un observable que satisface esas características estudiando las propiedades de las regiones de alta transmisión en el bosque de Lyman-alfa de espectros de objetos quasi-estelares (QSO). Nuestros resultados indican que para un conjunto de espectros de QSO, el número promedio de regiones coherentes por encima de un cierto valor en el espectro de flujo transmitido es profundamente afectado por Ω_ν. Usando el formalismo de la matriz de Fisher, concluimos que con un catálogo de ~ 400 espectros de alta resolución de QSO, podemos constreñir las masas de los neutrinos por debajo de $\Sigma_i m_{\nu_i} < 0.35$ eV, haciendo de este método uno de los observables más prometedores para poner bajos límites superiores en la masa de los neutrinos.

Podemos resumir las principales conclusiones y logros de esta tesis como sigue:

- La materia oscura templada no puede solucionar el problema de los picos/núcleos.
- Se forman halos de neutrinos en las mayores estructuras, gravitacionalmente unidas, del universo. Esos halos de neutrinos modifican el perfil de densidad del halo de ma-

teria oscura que los alberga. Esa perturbación puede ser detectada usando el método de lente débil.

- Los neutrinos cosmológicos juegan un papel muy importante en las propiedades de los agujeros cosmológicos. Se puede poner un fuerte límite en Ω_ν usando un catálogo con varios cientos de espectros de QSO de alta resolución, y calculando el número promedio de regiones coherentes por encima de un valor en el espectro de flujo transmitido como función de ese valor en el espectro de flujo transmitido.

Appendix C

Ω_ν sensitivity

C.1 Introduction

In order to estimate the sensitivity of the method described in the chatper 6, we have performed a detailed study of the degeneracies between the parameters which are expected to impact on the properties of the high transmission regions of the Lyman-α forest. For the analysis, we use the observable described in the chapter 7, i.e. the function mean number of regions above a threshold as a function of the threshold. We create mock QSO spectra catalogs to study the impact of the systematic errors such as the noise in the spectrum and the continuum fitting procedure. We also compute the Fisher matrix for catalogs with $S/N = 100$ and $S/N = \infty$ to study the marginalized error in $\Sigma_i m_{\nu_i}$. We use the prescription of McDonald et al.[58] for the continuum fitting.

C.2 Systematic errors

We have found that both, the continuum fitting procedure and the noise in the QSO spectra, affect the properties of the high transmission regions of the Lyman-α forest, but those changes are not large enough (for high resolution QSO spectra with S/N larger than 50 and $\Delta\lambda < 0.1\mathring{A}$) to erase the signal produced by the masses of the neutrinos. Using the observable described in the text, we find the same trend as this presented in the chapter 6, with differences between models decreasing as the S/N of the mock QSO spectra became smaller. The presence of metal lines should not affect our findings since in high resolution spectra these lines can be identified and metal-free regions can be conservatively used in the analysis and, by smoothing the transmitted flux over a region which is typically ~ 1 com. h^{-1}Mpc (roughly twenty times larger than the typical width of a metal line) we should be less sensitive to these contaminants.

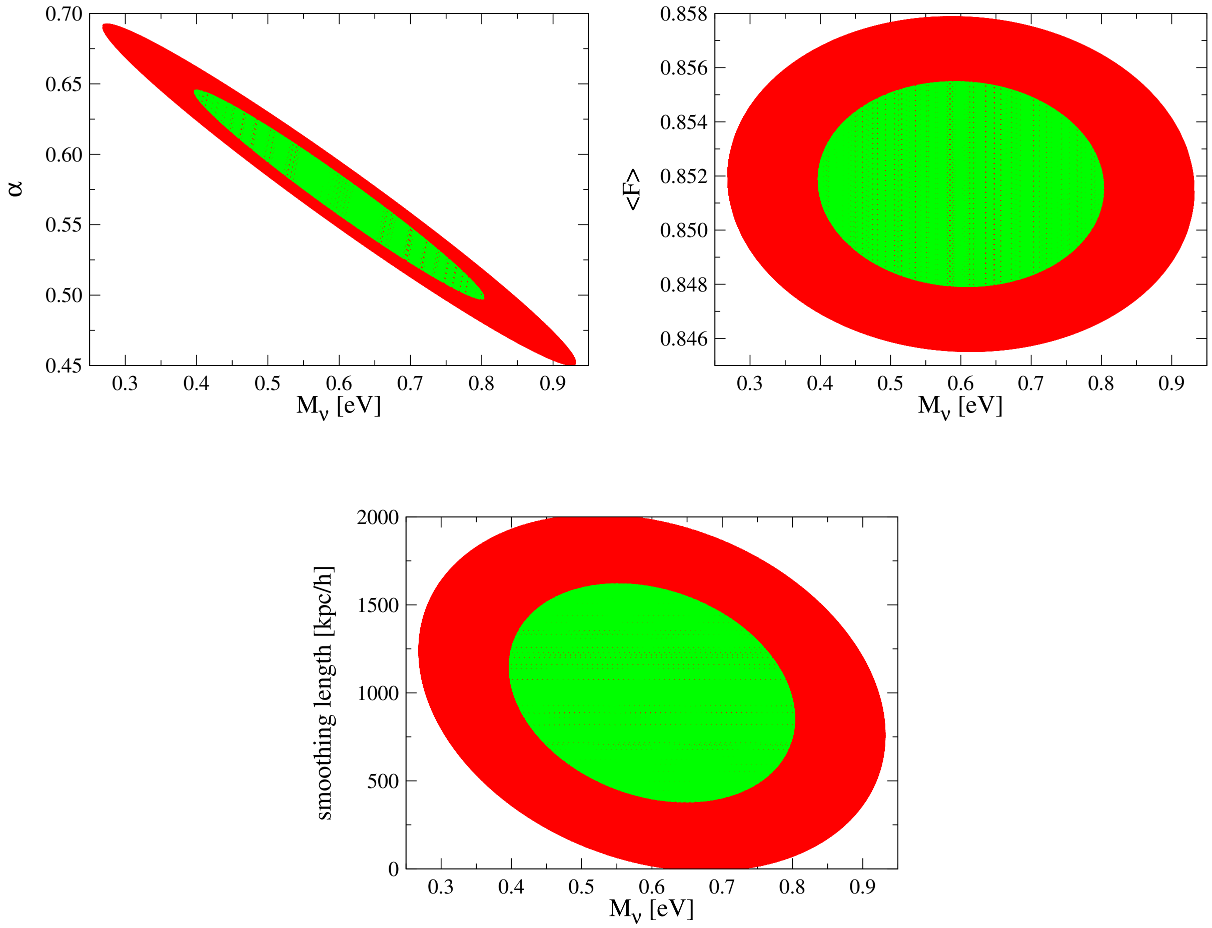

Figure C.1: $1-2\sigma$ contour plots for a catalog consisting on 200 high resolution QSO spectra with $S/N \approx 100$ and $\Delta\lambda = 0.05\mathring{A}$. We have assumed a prior of 10% for the error in α while the other parameters are taken with no priors.

C.3 Uncertainty in the parameters

By using the Fisher matrix formalism, we find that the effect of Ω_ν in the high transmission regions is strongly correlated with the thermal history of the gas. In our particular case, we find a strong degeneracy between Ω_ν and the parameter α present in the temperature-density relation of the IGM, $T = T_0(\rho_b/\overline{\rho}_b)^\alpha$. We find much smaller degeneracies with other parameters such as $< F >$ or the smoothing length. The marginalized error in $\Sigma_i m_{\nu_i}$ ranges from $0.25\sqrt{200/N}$ eV, with N being the number of QSO spectra in the catalog, for catalogs with $S/N = \infty$ and $\Delta\lambda = 1\mathring{A}$ to $0.5\sqrt{400/N}$ eV for catalogs with $S/N \approx 100$ and $\Delta\lambda = 0.05\mathring{A}$. Those errors are computed without assuming any priors for the parameters. We find that the main source of error to those values comes from the strong correlation with α. Those errors can be dramatically reduced by adding some prior over α or measuring its value from an independent measurement. In the Figure C.1 we plot the contour plots at 1(green) and 2(red) sigmas for a catalog consisting on 200 high resolution QSO spectra with $S/N \approx 100$ and $\Delta\lambda = 0.05\mathring{A}$. We have assumed that α is known with a 10% precision. We do not take any assumption over the other parameters.

As we show in the chapter 6, our method works better in the case where the amplitude of the power spectrum is fixed on large scales. The accuracy is smaller if σ_8 is fixed. In this case, to obtain accuracies smaller than 0.5 eV a larger number of QSO spectra are needed, with larger S/N and a better knowledge of the $T - \rho$ relationship.

C.4 Conclusion

Overall, we found that our method provides interesting, independent and competitive constraints on the total mass of the neutrinos. The number of QSO spectra that could be used is not unreasonable: at present there are indeed around more than one hundred spectra that have been used in the literature. Unfortunately, this signal is not visible with low resolution spectra such as those provided by SDSS.

Part V

Bibliography

Bibliography

[1] Abazajian K. N., et al., 2011, arXiv, arXiv:1103.5083

[2] Abramo L. R., Batista R. C., Liberato L., Rosenfeld R., 2007, Journal of Cosmology and Astroparticle Physics, 11, 12

[3] Alcock C., et al., 2000, Astrophysical Journal, 542, 281

[4] Bardeen J. M., Bond J. R., Kaiser N., Szalay A. S., 1986, Astrophysical Journal, 304, 15

[5] Barnes J., Hut P., Goodman J., 1986, Astrophysical Journal, 300, 112

[6] Belokurov V., et al., 2007, Astrophysical Journal, 654, 897

[7] Bertone G., Hooper D., Silk J., 2005, Physics Reports, 405, 279

[8] Bertschinger E., 1985, Astrophysical Journal, Supplement, 58, 1

[9] Bertschinger E., 1985, Astrophysical Journal, Supplement, 58, 39

[10] Blais-Ouellette S., Carignan C., Amram P., Côté S., 1999, Astronomical Journal, 118, 2123

[11] Blandford R., Narayan R., 1986, Astrophysical Journal, 310, 568

[12] Bode P., Ostriker J. P., Turok N., 2001, Astrophysical Journal, 556, 93

[13] Brandbyge J., Hannestad S., 2009, Journal of Cosmology and Astroparticle Physics, 5, 2

[14] Brandbyge J., Hannestad S., Haugbølle T., Thomsen B., 2008, Journal of Cosmology and Astroparticle Physics, 8, 20

[15] Brandbyge J., Hannestad S., 2010, Journal of Cosmology and Astroparticle Physics, 1, 21

[16] Brandbyge J., Hannestad S., Haugbølle T., Wong Y. Y. Y., 2010, Journal of Cosmology and Astroparticle Physics, 9, 14

[17] Bryan G. L., Norman M. L., 1998, Astrophysical Journal, 495, 80

[18] Clowe D., Bradač M., Gonzalez A. H., Markevitch M., Randall S. W., Jones C., Zaritsky D., 2006, Astrophysical Journal, 648, L109

[19] Colberg J. M., et al., 2008, Monthly Notices of the Royal Astronomical Society, 387, 933

[20] Cole S., et al., 2005, Monthly Notices of the Royal Astronomical Society, 362, 505

[21] Colín P., Valenzuela O., Avila-Reese V., 2008, Astrophysical Journal, 673, 203

[22] Cowan C. L., Jr., Reines F., Harrison F. B., Kruse H. W., McGuire A. D., 1956, Science, 124, 103

[23] Croft R. A. C., Weinberg D. H., Bolte M., Burles S., Hernquist L., Katz N., Kirkman D., Tytler D., 2002, Astrophysical Journal, 581, 20

[24] de Gouvêa A., Jenkins J., Kayser B., 2005, Physical Review D, 71, 113009

[25] Einstein A., 1916, Annalen der Physik, 354, 769

[26] Eisenstein D. J., et al., 2005, Astrophysical Journal, 633, 560

[27] Eisenstein D. J., Hu W., 1999, Astrophysical Journal, 511, 5

[28] Fillmore J. A., Goldreich P., 1984, Astrophysical Journal, 281, 1

[29] Fillmore J. A., Goldreich P., 1984, Astrophysical Journal, 281, 9

[30] Friedman A., 1922, Zeitschrift für Physik, 10, 377

[31] Friedmann A., 1924, Zeitschrift für Physik, 21, 326

[32] Furlanetto S. R., Piran T., 2006, Monthly Notices of the Royal Astronomical Society, 366, 467

[33] Gonzalez-Garcia M. C., Maltoni M., Salvado J., 2010, Journal of High Energy Physics, 4, 56

[34] Gonzalez-Garcia M. C., Maltoni M., Salvado J., 2010, Journal of High Energy Physics, 8, 117

[35] Governato F., et al., 2009, arXiv, arXiv:0911.2237

[36] Gunn J. E., Gott J. R., III, 1972, Astrophysical Journal, 176, 1

[37] Hamilton A. J. S., 2005, astro, arXiv:astro-ph/0503603

[38] Hamilton A. J. S., 2005, astro, arXiv:astro-ph/0503604

[39] Henon M., 1973, Astronomy and Astrophysics, 24, 229

[40] Henriksen R. N., Widrow L. M., 1997, Physical Review Letters, 78, 3426

[41] Hu W., Eisenstein D. J., 1998, Astrophysical Journal, 498, 497

[42] Hui L., Gnedin N. Y., 1997, Monthly Notices of the Royal Astronomical Society, 292, 27

[43] Jimenez R., Kitching T., Peña-Garay C., Verde L., 2010, Journal of Cosmology and Astroparticle Physics, 5, 35

[44] Kaiser N., Squires G., 1993, Astrophysical Journal, 404, 441

[45] KATRIN collaboration, 2001, hep.ex..., arXiv:hep-ex/0109033

[46] Kim T.-S., Bolton J. S., Viel M., Haehnelt M. G., Carswell R. F., 2007, Monthly Notices of the Royal Astronomical Society, 382, 1657

[47] Komatsu E., et al., 2009, Astrophysical Journal, Supplement, 180, 330

[48] Kraus C., et al., 2005, The European Physical Journal C, 40, 447

[49] Kravtsov A., 2010, Advances in Astronomy, 2010,

[50] Kuzio de Naray R., Martinez G. D., Bullock J. S., Kaplinghat M., 2010, Astrophysical Journal, 710, L161

[51] Lesgourgues J., Pastor S., 2006, Physics Reports, 429, 307

[52] Lithwick Y., Dalal N., 2011, Astrophysical Journal, 734, 100

[53] Lobashev V. M., 2003, Nuclear Physics A, 719, 153

[54] Loeb A., 2006, astro, arXiv:astro-ph/0603360

[55] Loeb A., Eisenstein D. J., 1995, Astrophysical Journal, 448, 17

[56] Ludlow A. D., Navarro J. F., Springel V., Vogelsberger M., Wang J., White S. D. M., Jenkins A., Frenk C. S., 2010, Monthly Notices of the Royal Astronomical Society, 406, 137

[57] Ma C.-P., Bertschinger E., 1994, Astrophysical Journal, 429, 22

[58] McDonald P., Miralda-Escudé J., Rauch M., Sargent W. L. W., Barlow T. A., Cen R., Ostriker J. P., 2000, Astrophysical Journal, 543, 1

[59] Markevitch M., Gonzalez A. H., Clowe D., Vikhlinin A., Forman W., Jones C., Murray S., Tucker W., 2004, Astrophysical Journal, 606, 819

[60] Martínez V. J., 2009, Lecture Notes in Physics, 665, 269

[61] Marulli F., Carbone C., Viel M., Moscardini L., Cimatti A., 2011, arXiv, arXiv:1103.0278

[62] Meiksin A. A., 2009, Reviews of Modern Physics, 81, 1405

[63] Mena O., Razzaque S., Villaescusa-Navarro F., 2011, Journal of Cosmology and Astroparticle Physics, 2, 30

[64] Miralda-Escudé J., Cen R., Ostriker J. P., Rauch M., 1996, Astrophysical Journal, 471, 582

[65] Mukhanov V., Physical Foundations of Cosmology, Cambridge University Press, November 2005, pp. 442.

[66] Navarro J. F., Frenk C. S., White S. D. M., 1996, Astrophysical Journal, 462, 563

[67] Navarro J. F., et al., 2010, Monthly Notices of the Royal Astronomical Society, 402, 21

[68] Particle Data Group, et al., 2004, Physics Letters B, 592, 1

[69] Peccei R. D., Quinn H. R., 1977, Physical Review Letters, 38, 1440

[70] Peebles P. J. E., The large-scale structure of the universe, Princeton University Press, 1980. 435 p.

[71] Penzias A. A., Wilson R. W., 1965, Astrophysical Journal, 142, 419

[72] Rauch M., 1998, Annual Review of Astronomy and Astrophysics, 36, 267

[73] Reid B. A., Verde L., Jimenez R., Mena O., 2010, Journal of Cosmology and Astroparticle Physics, 1, 3

[74] Riess A. G., et al., 1998, Astronomical Journal, 116, 1009

[75] Ringwald A., Wong Y. Y. Y., 2004, Journal of Cosmology and Astroparticle Physics, 12, 5

[76] Roos M., 2010, arXiv, arXiv:1001.0316

[77] Schneider P., Ehlers J., Falco E. E., Gravitational Lenses, XIV, Springer-Verlag Berlin Heidelberg New York, 1992, 560 pp. 112 figs.

[78] Seljak U., Makarov A., McDonald P., Trac H., 2006, Physical Review Letters, 97, 191303

[79] Seljak U., Slosar A., McDonald P., 2006, Journal of Cosmology and Astroparticle Physics, 10, 14

[80] Sheth R. K., van de Weygaert R., 2004, Monthly Notices of the Royal Astronomical Society, 350, 517

[81] Sikivie P., 1985, Physical Review D, 32, 2988

[82] Sikivie P., 1983, Physical Review Letters, 51, 1415

[83] Simon J. D., Geha M., 2007, Astrophysical Journal, 670, 313

[84] Singh S., Ma C.-P., 2003, Physical Review D, 67, 023506

[85] Slosar A., et al., 2011, arXiv, arXiv:1104.5244

[86] Springel V., 2005, Monthly Notices of the Royal Astronomical Society, 364, 1105

[87] Taoso M., Bertone G., Masiero A., 2008, Journal of Cosmology and Astroparticle Physics, 3, 22

[88] Tegmark M., et al., 2004, Astrophysical Journal, 606, 702

[89] Thomas S. A., Abdalla F. B., Lahav O., 2010, Physical Review Letters, 105, 031301

[90] Tollerud E. J., Bullock J. S., Strigari L. E., Willman B., 2008, Astrophysical Journal, 688, 277

[91] Tremaine S., Gunn J. E., 1979, Physical Review Letters, 42, 407

[92] Tremaine S., Richstone D. O., Byun Y.-I., Dressler A., Faber S. M., Grillmair C., Kormendy J., Lauer T. R., 1994, Astronomical Journal, 107, 634

[93] Viel M., Colberg J. M., Kim T.-S., 2008, Monthly Notices of the Royal Astronomical Society, 386, 1285

[94] Viel M., Haehnelt M. G., Springel V., 2010, Journal of Cosmology and Astroparticle Physics, 6, 15

[95] Villaescusa-Navarro F., Dalal N., 2011, Journal of Cosmology and Astroparticle Physics, 3, 24

[96] Villaescusa-Navarro F., Miralda-Escudé J., Peña-Garay C., Quilis V., 2011, Journal of Cosmology and Astroparticle Physics, 6, 27

[97] Villaescusa-Navarro F., Vogelsberger M., Viel M., Loeb A., 2011, arXiv, arXiv:1106.2543

[98] Vogelsberger M., White S. D. M., Mohayaee R., Springel V., 2009, Monthly Notices of the Royal Astronomical Society, 400, 2174

[99] Wang S., Haiman Z., Hu W., Khoury J., May M., 2005, Physical Review Letters, 95, 011302

[100] Wang J., White S. D. M., 2007, Monthly Notices of the Royal Astronomical Society, 380, 93

[101] Wang J., White S. D. M., 2009, Monthly Notices of the Royal Astronomical Society, 396, 709

[102] Wechsler R. H., Bullock J. S., Primack J. R., Kravtsov A. V., Dekel A., 2002, Astrophysical Journal, 568, 52

[103] Weinberg S., Principles and Applications of the General Theory of Relativity, Wiley-VCH, 1972, pp. 688.

[104] Weinberg S., Cosmology, Oxford University Press, 2008.

[105] Zhao D. H., Jing Y. P., Mo H. J., Börner G., 2009, Astrophysical Journal, 707, 354

[106] Zhao D. H., Jing Y. P., Mo H. J., Börner G., 2003, Astrophysical Journal, 597, L9

[107] Zhao D. H., Mo H. J., Jing Y. P., Börner G., 2003, Monthly Notices of the Royal Astronomical Society, 339, 12

[108] Zwicky F., 1933, Helvetica Physica Acta, 6, 110